A&A 523, A6 (2010)
DOI: 10.1051/0004-6361/201014422

Astronomy & Astrophysics

A gallery of bubbles

The nature of the bubbles observed by *Spitzer* and what ATLASGAL tells us about the surrounding neutral material[⋆]

L. Deharveng[1], F. Schuller[2], L. D. Anderson[1], A. Zavagno[1], F. Wyrowski[2], K. M. Menten[2], L. Bronfman[3], L. Testi[4], C. M. Walmsley[5], and M. Wienen[2]

[1] Laboratoire d'Astrophysique de Marseille (UMR 6110 CNRS & Université de Provence), 38 rue F. Joliot-Curie, 13388 Marseille Cedex 13, France
e-mail: `lise.deharveng@oamp.fr`
[2] Max-Planck Institut für Radioastronomie, Auf dem Hügel 69, 53121 Bonn, Germany
[3] Departamento de Astronomia, Universidad de Chile, Casilla 36-D, Santiago, Chile
[4] ESO, Karl Schwarzschild-Strasse 2, 85748 Garching bei München, Germany
[5] Osservatorio Astrofisico di Arcetri, Largo E. Fermi, 5, 50125 Firenze, Italy

Received 12 March 2010 / Accepted 25 June 2010

ABSTRACT

Context. This study deals with infrared bubbles, the H II regions they enclose, and triggered massive-star formation on their borders.
Aims. We attempt to determine the nature of the bubbles observed by *Spitzer* in the Galactic plane, mainly to establish if possible their association with massive stars. We take advantage of the very simple morphology of these objects to search for star formation triggered by H II regions, and to estimate the importance of this mode of star formation.
Methods. We consider a sample of 102 bubbles detected by *Spitzer*-GLIMPSE, and catalogued by Churchwell et al. (2006; hereafter CH06). We use mid-infrared and radio-continuum public data (respectively the *Spitzer*-GLIMPSE and -MIPSGAL surveys and the MAGPIS and VGPS surveys) to discuss their nature. We use the ATLASGAL survey at 870 μm to search for dense neutral material collected on their borders. The 870 μm data traces the distribution of cold dust, thus of the dense neutral material where stars may form.
Results. We find that 86% of the bubbles contain ionized gas detected by means of its radio-continuum emission at 20-cm. Thus, most of the bubbles observed at 8.0 μm enclose H II regions ionized by O-B2 stars. This finding differs from the earlier CH06 results (∼25% of the bubbles enclosing H II regions). Ninety-eight percent of the bubbles exhibit 24 μm emission in their central regions. The ionized regions at the center of the 8.0 μm bubbles seem to be devoid of PAHs but contain hot dust. PAH emission at 8.0 μm is observed in the direction of the photodissociation regions surrounding the ionized gas. Among the 65 regions for which the angular resolution of the observations is high enough to resolve the spatial distribution of cold dust at 870 μm, we find that 40% are surrounded by cold dust, and that another 28% contain interacting condensations. The former are good candidates for the collect and collapse process, as they display an accumulation of dense material at their borders. The latter are good candidates for the compression of pre-existing condensations by the ionized gas. Thirteen bubbles exhibit associated ultracompact H II regions in the direction of dust condensations adjacent to their ionization fronts. Another five show methanol masers in similar condensations.
Conclusions. Our results suggest that more than a quarter of the bubbles may have triggered the formation of massive objects. Therefore, star formation triggered by H II regions may be an important process, especially for massive-star formation.

Key words. stars: formation – stars: early-type – ISM: bubbles – H II regions

1. Introduction

The *Spitzer*-GLIMPSE images at 8.0 μm (Benjamin et al. 2003) have revealed a "bubbling Galactic disk" (Churchwell et al. 2006; hereafter CH06). About 600 ring structures have been detected and catalogued between longitudes −60° and +60° by CH06 and Churchwell et al. (2007). Most of these bubbles have angular diameters smaller than 10′; according to Churchwell et al. (2007), many more bubbles are present, with smaller or larger diameters. Thus, understanding the origin of these bubbles is important. After comparison with catalogues of known radio H II regions and catalogues of star clusters, CH06 conclude that "*about 25% of the bubbles coincide with known radio H II regions, and about 13% enclose known star clusters. It appears that B4–B9 stars probably produce about three-quarters of the bubbles in our sample*". This conclusion, which we disagree with, was based mainly on a comparison with the Paladini et al. (2003) catalog of diffuse and compact H II regions, which have a typical angular extent of a few arcmins. This catalogue is based on previously published lists of H II regions obtained from single-dish medium resolution observations, typically with beamwidths of a few arcmin. Thus, many ultracompact (UC) or compact H II regions, which could possibly be associated with *Spitzer* bubbles, are absent from the Paladini et al. (2003) catalogue. To improve this situation, we have used the Multi-Array Galactic Plane Imaging Survey (MAGPIS), a radio-continuum

---

[⋆] Appendices are only available in electronic form at http://www.aanda.org survey conducted with the NRAO Very Large Array (VLA) at 20-cm. The angular resolution of MAGPIS (5″), allows us to detect compact and ultracompact (UC) H II regions with small angular sizes. We have also utilized data from the *Spitzer*-MIPSGAL survey at 24 μm (Carey et al. 2009). These data show the extended emission of hot dust and also possibly the emission from associated young stellar objects (YSOs). This study is presented in Sect. 4, after a general introduction about the formation and evolution of an H II region in Sect. 2, and the description of the surveys in Sect. 3. We have studied one hundred and two bubbles, allowing us to derive statistical conclusions.

In Section 5, we take advantage of the very simple morphology of the bubbles to search for dense neutral shells and condensations surrounding the H II regions. These condensations are potential sites of star formation. This work is based on the APEX[1] Telescope Large Area Survey of the Galactic plane at 870 μm (ATLASGAL; Schuller et al. 2009). Because it is sensitive to the emission from cold dust, the ATLASGAL survey detects the dense cores inside which stars form. The distribution of cold dust (and thus the distribution of dense molecular material) also reflects the interaction between the bubbles and their surroundings.

In Sect. 6, once again, we take advantage of the simple morphology of these regions to discuss the influence of the environment on the shape of the bubbles, and the distribution of various types of dust grains. We present several possible cases of massive-star formation triggered by the expansion of H II regions. Detailed studies of the most interesting regions in terms of triggered star formation will be given in a forthcoming paper.

2. Morphology and evolution of an H II region

We consider a simple model of H II region evolution in which an H II region forms and evolves in a uniform medium of density n_0 atoms cm^{-3} (Fig. 1). The ionizing flux of the central exciting star is N_* photons s^{-1}. According to Dyson & Williams (1997), two main phases can be distinguished during the life of the H II region:

- First, there is a short formation phase during which the central star rapidly ionizes the neutral medium. Because of the speed at which the neutral medium is ionized, the neutral and ionized gases are at rest with respect to each other and at the same density ($n_e = n_0$). For $n_0 = 10^4$ cm^{-3} and $N_* = 10^{49}$ photons s^{-1} (the ionizing photon flux of an O6V star), this phase lasts about 50 years. At the end of this phase, for these values of n_e and N_*, the radius of the Strömgren sphere is $R_0 \sim 0.15$ pc.
- The formation phase is followed by a long expansion phase. Because of the higher pressure in the warm ionized gas ($T_e \sim 10^4$ K) than in the cold neutral surrounding medium (T in the range 10−100 K), the H II region expands. This expansion is supersonic; the ionization front (IF) is preceded by a shock front (SF) on the neutral side. With time, the size and mass of the H II region increase, whereas the electron density and the expansion velocity decrease. The expansion ceases when the ionized gas reaches pressure equilibrium with the surrounding neutral gas. Except in a high density medium, this equilibrium is not reached before the death of the central exciting star. For example, for expansion in a uniform medium of density $n_0 = 100$ cm^{-3}, and for $N_* = 10^{49}$ photons s^{-1}, equilibrium is reached after 80×10^6 yr when the radius of the H II region is $R \sim 34\ R_0$, and the electron density $n_e \sim 0.5$ cm^{-3}. The exciting star has left the main-sequence at this time, as the lifetime of an O6 star is of the order of 8×10^6 yr (Schaller et al. 1992).

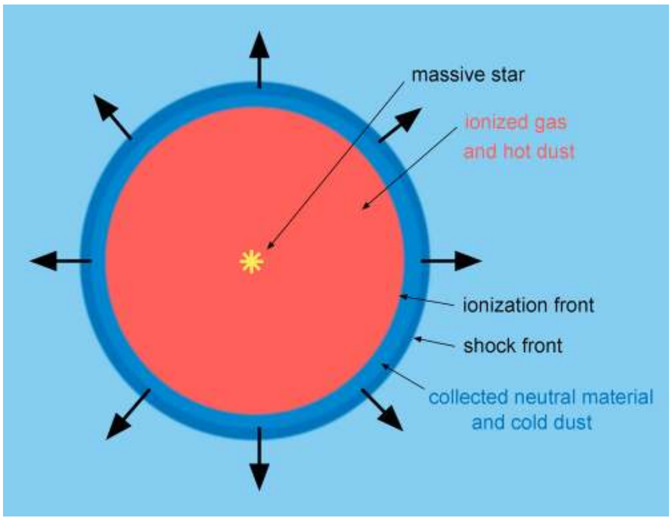

Fig. 1. Model of a spherical H II region expanding into a homogeneous medium. The ionized region is surrounded by a shell of dense neutral material collected during the expansion phase.

During the expansion of the H II region, neutral material accumulates between the IF and the SF. A layer of dense neutral material builds up around the ionized region. With time, this layer becomes very massive, perhaps several thousand solar masses (Hosokawa & Inutsuka 2006b). A new generation of stars may form in the collected layer (see Sect. 5). The dynamical expansion of ionization and dissociation fronts around a massive star has been simulated by Hosokawa & Inutsuka (2005, 2006a,b), taking into account the transfer of UV and FUV radiation, the thermal equilibrium of the gas, and the dissociation of the H_2 and CO molecules. These simulations show that the density in the shell is 10 to 100 times higher than the ambient gas density and that the highest densities are found in the outer parts of the shell. They show that the shell becomes gravitationally unstable, first in its outer parts, and that the gas is mainly molecular at the time of gravitational collapse.

This model is very simple and neglects several well-known facets of H II region evolution:

- Inhomogeneus neutral material. It is difficult to believe that an H II region of a several parsec diameter can evolve in a perfectly uniform medium. The surrounding medium is most likely turbulent (Falgarone & Phillips 1996), and thus highly inhomogeneous. H II regions forming and evolving in a turbulent medium were simulated by Mellema et al. (2006), who illustrated the highly irregular shape of the H II region's IF. Some other simulations of a shock propagating into a turbulent medium (Elmegreen et al. 1995) show that the clumps formed by turbulence are squeezed and collected into the compressed layer, and merge into a few massive cores. These cores protrude slightly into the ionized gas, forming bright rims. Massive stars form in dense cores that contain density gradients. Icke (1979), for example, considers the initial formation of H II regions (their first phase) in a medium presenting an exponential density distribution. The H II regions are egg-shaped (elongated in the directions of lower density); they may even be open in these directions if the ionizing photon flux is high or if the ambient density

---

[1] This publication is based on data acquired with the Atacama Pathfinder EXperiment (APEX). APEX is a collaboration between the Max-Planck-Institut für Radioastronomie, the European Southern Observatory, and the Onsala Space Observatory.

is low. The formation and expansion of H II regions in clouds with a power-law density stratification, r^{-w}, and in isothermal self-gravitating disks was described by Franco et al. (1990). For power-law profiles, there is a critical value of w above which the cloud is entirely ionized. During the expansion phase, $w_{\rm crit} = 3/2$. For clouds with $w < 3/2$, the H II region expands and neutral material is collected in a shell around the ionized region. For clouds with $w \geq 3/2$, a "champagne phase" occurs, as described in Tenorio-Tagle (1979): the dense ionized part of the cloud expands supersonically into the low-density surrounding ionized medium. After the champagne phase, there is no additional accumulation of neutral material around the H II region. Bisbas et al. (2009) simulated another situation of the expansion of an off-center H II region formed in a homogeneous cloud. Here again, the H II region opens on the outside when the IF reaches the edge of the cloud. All these departures from evolution in a homogeneous medium act to destroy the spherical symmetry of the H II region, and reduce the efficiency of collecting material during its expansion phase.

- Stellar winds emitted by the exciting stars. Capriotti & Kozminski (2001) and Freyer et al. (2003, 2006) developed analytical models and hydrodynamical simulations of H II regions, including stellar winds. At the beginning of its evolution, the young H II region should not be significantly affected by the wind of its exciting star(s). With time, the wind strengthens (especially at the end of the star's lifetime, in the Wolf-Rayet stage). A stellar-wind bubble filled of very hot ($T \sim 10^6$ K), low density, shocked gas forms inside the H II region. The X-ray emission of this gas has been observed for M17 and the Rosette Nebula (Townsley et al. 2003), and the Orion Nebula (Güdel et al. 2008). It is often claimed that the many bubbles observed in the Galactic plane are the result of the action of powerful winds (CH06), but this remains to be established. The presence of a central hole in the distribution of the ionized gas may be the indirect signature of the action of stellar winds, as discussed by Watson et al. (2008, 2009).
- A magnetic field. Krumholz et al. (2007) present a simulation of an H II region expanding into a magnetised gas. This simulation shows that magnetic fields suppress the sweeping up of gas perpendicular to magnetic field lines. This leads to a non-spherical H II region, elongated in the direction of the magnetic field, bounded by a dense shell of swept-up gas in the direction along the field, but not perpendicular to it. The authors conclude that this may reduce the efficiency of star formation triggered by H II regions.
- The radiation-pressure of the exciting stars. Krumholz & Matzner (2009) evaluated the role of radiation pressure in the dynamics of H II regions. They demonstrated that it is unimportant for H II regions driven by a handful of massive stars (which is the case for the H II regions discussed in this paper).

We describe the morphology of the 102 bubbles discussed here in Sect. 6.1.

3. Surveys used in this study

3.1. The Spitzer-GLIMPSE and -MIPSGAL surveys

The bubbles catalogued by CH06 have been detected at 8.0 μm in the *Spitzer*-GLIMPSE survey of the Galactic plane (Benjamin et al. 2003). This survey extends from l = 295° to 65°, $|b| \leq 1°$, with additional latitude coverage near the Galactic center. At 8.0 μm, the angular resolution of the *Spitzer* IRAC instrument is $1\farcs9$ (Fazio et al. 2004). We also use images at 24 μm from the *Spitzer*-MIPSGAL survey (Carey et al. 2009), which has the same Galactic coverage. The resolution of the *Spitzer* MIPS instrument is $6''$ at 24 μm (Rieke et al. 2004).

The *Spitzer*-IRAC filter centered on 8.0 μm contains the 7.7 μm and 8.6 μm emission bands generally attributed to polycyclic aromatic hydrocarbon (PAH) molecules or clusters of molecules. Infrared emission from PAHs is observed in the direction of photo-dissociation regions (PDRs), where they are excited by the absorption of far-UV photons leaking from H II regions. Thus, PAH emission is a good tracer of ionization fronts. The PAH emission bands are superimposed on continuum emission generally attributed to the PAHs and/or to very small grains (VSGs) that are out of thermal equilibrium after absorption of high energy photons (Léger & Puget 1984; Sellgren 1984; Desert et al. 1990; Draine & Li 2007; Tielens 2008, and references therein). The distribution of PAHs is discussed in Sect. 6.2.

The *Spitzer*-MIPS filter centered on 24 μm is dominated by continuum emission, which may be due to very small grains (VSGs) being out of thermal equilibrium, or to big grains (BGs) being in thermal equilibrium. (The maximum of the Planck function B_ν for dust grains in equilibrium at 120 K is at λ = 24 μm.) This point is discussed in Sect. 6.3.

3.2. The MAGPIS survey

The Multi-Array Galactic Plane Imaging Survey (MAGPIS; Helfand et al. 2006) is a 20-cm VLA continuum survey of the Galactic plane. This survey spans l = 5° to $48\fdg$ and $|b| < 0.8°$. It has a resolution of $\sim 5''$, a detection threshold in the range 1–2 mJy, and a high dynamic range ~1000:1. The VLA images were combined with images from the Effelsberg 100-m telescope to account for the flux from large-scale structures. The high resolution of the MAGPIS survey allows the detection of the free-free emission from compact and ultracompact H II regions that are small in angular size. It is especially useful when looking for (second-generation) UC H II regions at the borders of large (first-generation) H II regions (Sect. 6.5).

We used the MAGPIS website[2], and especially the image "cutout" facility to extract, for each bubble, MAGPIS 20-cm, *Spitzer*-GLIMPSE 8.0 μm, and *Spitzer*-MIPSGAL 24 μm images. These images have user-specified center and size. They are regridded to have the same number of pixels (with a pixel size of $2''$), which makes the comparison of the same object at different wavelengths easier. The sizes of the extracted fields are multiples of $5'$ (up to $30'$), depending on the size of the bubbles. The sizes of these fields, and thus of the colour images presented in Sect. 4, are given in Table A.1.

3.3. The VGPS survey

For MAGPIS fields that are too noisy or not sensitive enough, we used the continuum data from the VLA Galactic Plane Survey at 21-cm (VGPS, Stil et al. 2006). This survey extends from l = 18° to 67°, with $|b|$ varying from 1.3° to 2.6° over the longitude range. The H I line and continuum emission observations at 21-cm have a resolution (*FWHM*) of $1'$. In our analysis, we have oversampled the VGPS maps from their native $18''$ pixels to $2''$ pixels to allow comparison with the 8.0 μm and 24 μm images obtained with the MAGPIS cut-out facility.

---

[2] `http://third.ucllnl.org/gps/`

3.4. The ATLASGAL survey at 870 μm

ATLASGAL is the APEX Telescope Large Area Survey of the Galaxy at 870 μm (Schuller et al. 2009). This survey covers the inner Galactic plane, $l = 300^\circ$ to 60°, $|b| \leq 1.5^\circ$, with an rms noise in the range 0.05–0.07 Jy/beam. The calibration uncertainty in the final maps is of the order of 15%.

LABOCA, the Large Apex BOlometer CAmera used for these observations, is a 295-pixel bolometer array developed by the Max-Planck-Institut für Radioastronomie (Siringo et al. 2007). The beam size at 870 μm is 19″.2. The observations are reduced using the Bolometer array data Analysis package (BoA; Schuller et al., in preparation). During the reduction, and as a result of the correction for correlated noise, uniformly extended emission (on scales larger than 2.5′) that mimics variations in the sky emission (skynoise) is filtered out. This can be a problem for our analysis, as we search for extended structures.

The continuum emission at 870 μm is dominated by the thermal emission from cold dust. Low temperature dust is contained in dense material: dense molecular cores or filaments. These structures are the places where stars form.

4. The nature of the bubbles observed by *Spitzer*

We study one hundred and two bubbles from 10° to 48°, with $|b| \leq -0^\circ\!.8$. This longitude range represents the overlap between the CH06 catalogue and the MAGPIS survey. A few bubbles from the list of CH06 are missing in our sample. Bubbles N5 and N19 are too high in latitude to be mapped by MAGPIS. Bubbles N17, N30, and N38 are entirely surrounded by the larger N16, N29, and N39 bubbles. Bubbles N63 and N88, are supernova remnants (SNRs) and we do not include them in the present study (see CH06 and references therein). We added 11 new bubbles found in the observed fields close to the CH06 bubbles (called Nxxbis, if in the field of Nxx; otherwise, named by their Galactic longitude). Three of the bubbles of our sample are included in the study of Watson et al. (2008); they are N10, N21, and N49.

For each of these bubbles, we compiled two-color composite images with PHOTOSHOP to compare the emission of the ionized gas to that of the dust at 8.0 μm and 24 μm. We show twelve of these images in Fig. 2 (N13, N33, and N42) and Fig. 3 (N4, N14, and N36). In these figures[3], red shows the hot dust emission at 24 μm (top rows) or the ionized gas free-free emission at 20-cm (bottom rows). Turquoise shows the 8.0 μm emission tracing the bubbles.

Images for all the bubbles can be found online[4]. The name of these images begins with the name of the bubble, followed by "_8+24" or "_8+MAGPIS" or "_8+VGPS", indicating which frames have been combined (8 and 24 are for 8.0 μm and 24 μm). For example, N1_8+24.eps and N1_8+MAGPIS.eps are the names of the two color images relating to the N1 bubble. When several sources are present in the same field they have been identified; otherwise the bubble is always in the center of the field.

Based on the MAGPIS or VGPS data, we determined whether the bubbles are surrounding H II regions. Our conclusions are presented in Table A.1 (Appendix A), available online. Column 1 is their identification name. Their Galactic coordinates from CH06 are given in Cols. 2 and 3. Column 4 gives the angular size of the fields analyzed (these are also the size of the colour images). Columns 5 and 6 comment on the presence or absence of the radio-continuum and the 24 μm extended emissions. Column 7 provides our conclusions about the nature of the bubbles (whether they are surrounding H II regions).

Of the 102 bubbles studied here, 88 (86%) enclose H II regions, as they contain ionized gas detected via their radio-continuum emission. This strongly differs from the conclusions of CH06 who stated that only one-quarter of the bubbles enclose H II regions (the other three-quarter being associated with non-ionizing B4–B9 stars).

Furthermore, the percentage of bubbles enclosing H II regions is probably still underestimated here, and may increase to 93%. The VGPS survey shows radio emission in the direction of a number of small bubbles not detected by MAGPIS: N48, N71, N84, N85, and N87. However, because radio emission is also observed outside these bubbles, and the resolution of the VGPS (1′) is comparable to the size of these bubbles, their nature as H II regions is questionable; we are unsure wether these bubbles enclose H II regions (thus the "?" in Table A.1, Col. 7, for their nature). In addition, N64bis is observed in the direction of a very bright 20-cm radio source (the SNR W44 or G034.6-00.5), preventing the detection of any faint emission associated with the bubble. The nature of N6, a complex bubble, is also unclear. This bubble is composed of two different structures: an open and faint bubble in the northeast, and a filamentary ionization front in the southwest. Both structures appear as filaments at 24 μm, but they are possibly not linked.

Extended 24 μm emission is observed in the direction of the PDRs and inside the bubbles. Ninety-eight percent of the bubbles exhibit extended 24 μm emission enclosed within the bubble. The only exceptions are N7 and N15. The bubble N7 lies on the border of a bright molecular condensation enclosing the most active parts of the active and complex star-forming region W33 (Beck et al. 1998). The bubble N15 lies on the border of M17, an extremely luminous massive star-formation region. Both N7 and N15 do not seem to be individual bubbles but appear to be filaments at the periphery of active H II regions; they are possibly caused by the expansion of very hot gas.

The origin and distribution of the 8.0 μm and 24 μm emissions are discussed in Sects. 6.2 and 6.3.

5. The neutral environment of the bubbles as seen by ATLASGAL

We now study the distribution of the dense neutral material traced using the ATLASGAL survey at 870 μm that is associated with the bubbles and their enclosed H II regions. We take advantage of their simple morphology to detect the material collected during their expansion phase.

During the expansion of an H II region, neutral material accumulates between the ionization and shock fronts, forming a shell of dense material (10 to 100 times the density of the neutral surrounding material) surrounding the ionized gas. With time the mass of this shell increases, reaching thousands of solar masses (see Sect. 2). The shell is dense and is mainly molecular. Thus, it should contain cold dust, which radiates in the (sub-)millimeter range. It is the thermal emission from this cold dust that is observed with the APEX-LABOCA camera at 870 μm.

This shell is an important component of the photodissociation region (PDR). It may become gravitationally unstable,

---

[3] These images are RGB color images; the Red channel contains the 24 μm or radio-continuum image; the Green and Blue channels contain the same 8 μm image, thus the turquoise color for the 8 μm emitting regions. The RGB color model is an additive color model; thus a region with both 24 μm and 8 μm emission (or both radio and 8 μm emission) will appear in white, independently of the intensity of these emissions.

[4] `http://lamwws.oamp.fr/bubbles`

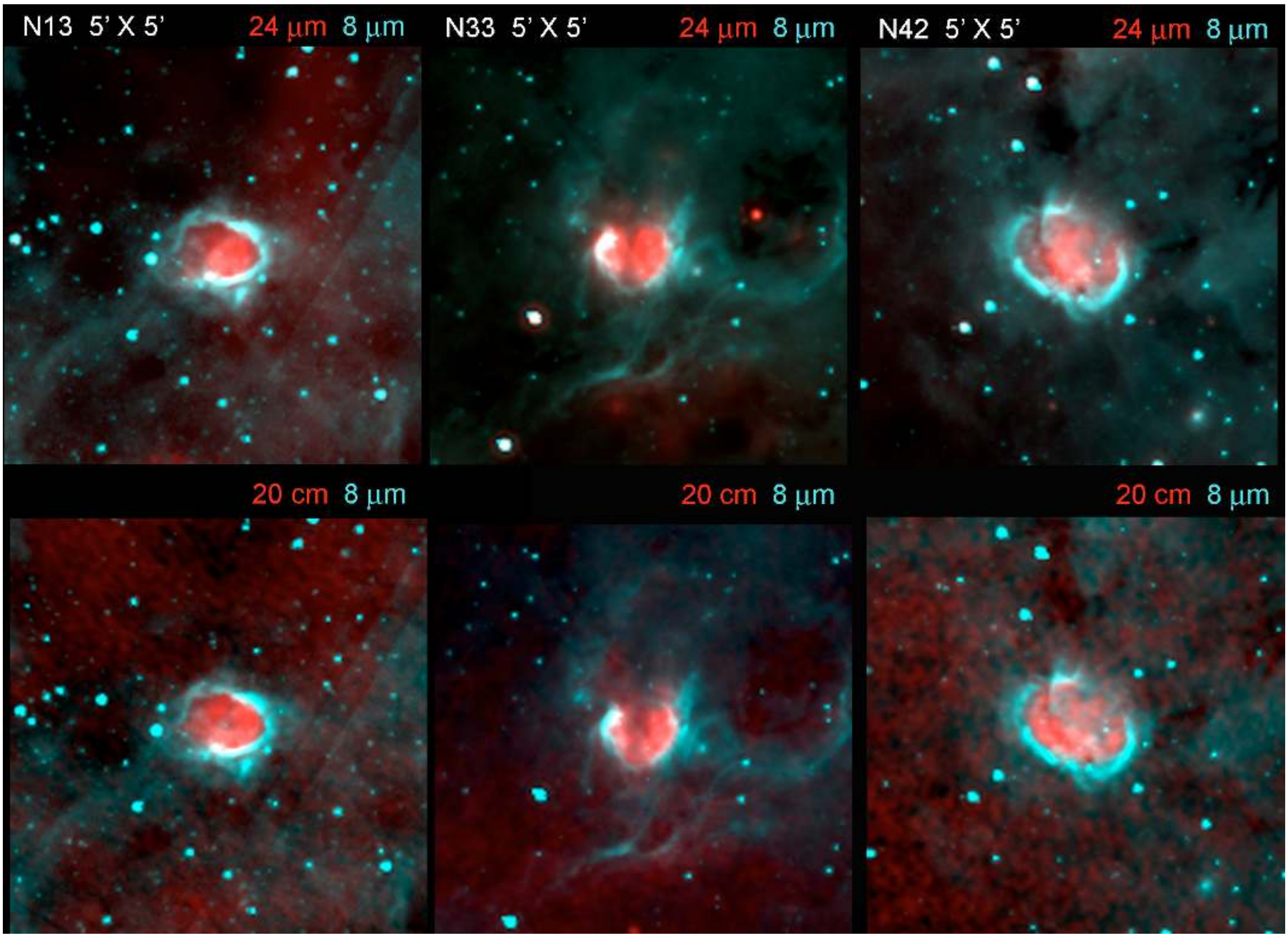

Fig. 2. Examples of three bubbles that are small in angular size. All the fields are 5′ × 5′. Turquoise is the *Spitzer*-GLIMPSE images at 8.0 μm, which defines the bubbles. Red is the *Spitzer*-MIPSGAL emission at 24 μm from hot dust (*top row*) or MAGPIS 20-cm radio continuum emission from the ionized gas (*bottom row*). Directions in which both the 8 μm and 24 μm emission (or both the 8 μm and radio emission) are present appear in white, independent of the intensity of the emission. Equivalent images for the entire sample are available online.

leading to star formation. In theory, stars of all masses can form in this shell around H II regions (cf. Fig. 4). Small-scale gravitational instabilities (for example Jeans instabilities) can lead to the formation of low-mass stars. Large-scale gravitational instabilities along the collected shell can lead to the formation of massive fragments, potential sites of massive-star formation; this is the "collect & collapse" process (Elmegreen & Lada 1977). The ionizing radiation can also act on a turbulent medium, forming peculiar structures such as fingers or pillars (Gritschneder et al. 2009), and pre-existing condensations can be compressed by the pressure of the ionized gas. (This mechanism is often called "radiation-driven implosion" of a condensation, but "radiation-driven compression" would be better as no observations indicate that star formation occurs during the implosion.) Good illustrations of star formation triggered by the expansion of H II regions are given by the RCW 79 (Zavagno et al. 2006) and RCW 120 (Deharveng et al. 2009) bubbles.

In the following, we use the ATLASGAL survey to search for the following signatures:

- A shell of cold dust emission material, surrounding the ionized H II region and adjacent to the 8.0 μm bubble.
- Massive fragments, observed elongated along the IF. These fragments are expected if the shell is already fragmented by means of the collect & collapse process; they should have masses of several tens or hundreds of solar masses. These fragments should not distort the IF because they are formed from collected material that moves at the same velocity as the ionization and shock fronts.
- Massive condensations protruding inside the ionized region. This is the signature of pre-existing massive condensations; they distort the shape of the ionization front because their velocity differs from that of the IF. They are dense, thus bordered by bright rims at 8.0 μm and by bright radio emission on the ionized side.
- Thin structures, such as fingers or pillars, protuding inside the ionized gas. These are signatures of a turbulent medium. These structures are expected to be of low mass, and should therefore be more difficult to detect for distant bubbles. These dense pillars should also be bordered by bright rims at 8.0 μm.

Young stellar objects (YSOs) should be present in the PDRs surrounding the H II regions. They can be identified based on their infrared (IR) colours (see the discussion in Robitaille et al. 2008). Since the stars share the velocity of the material inside which they form, the second-generation stars, formed in the collected layer by gravitational instabilities, should be observed later on in the direction of the collected material (or slightly in front, on the neutral side, if they have formed early in the evolution of the H II region, when its expansion velocity was large).

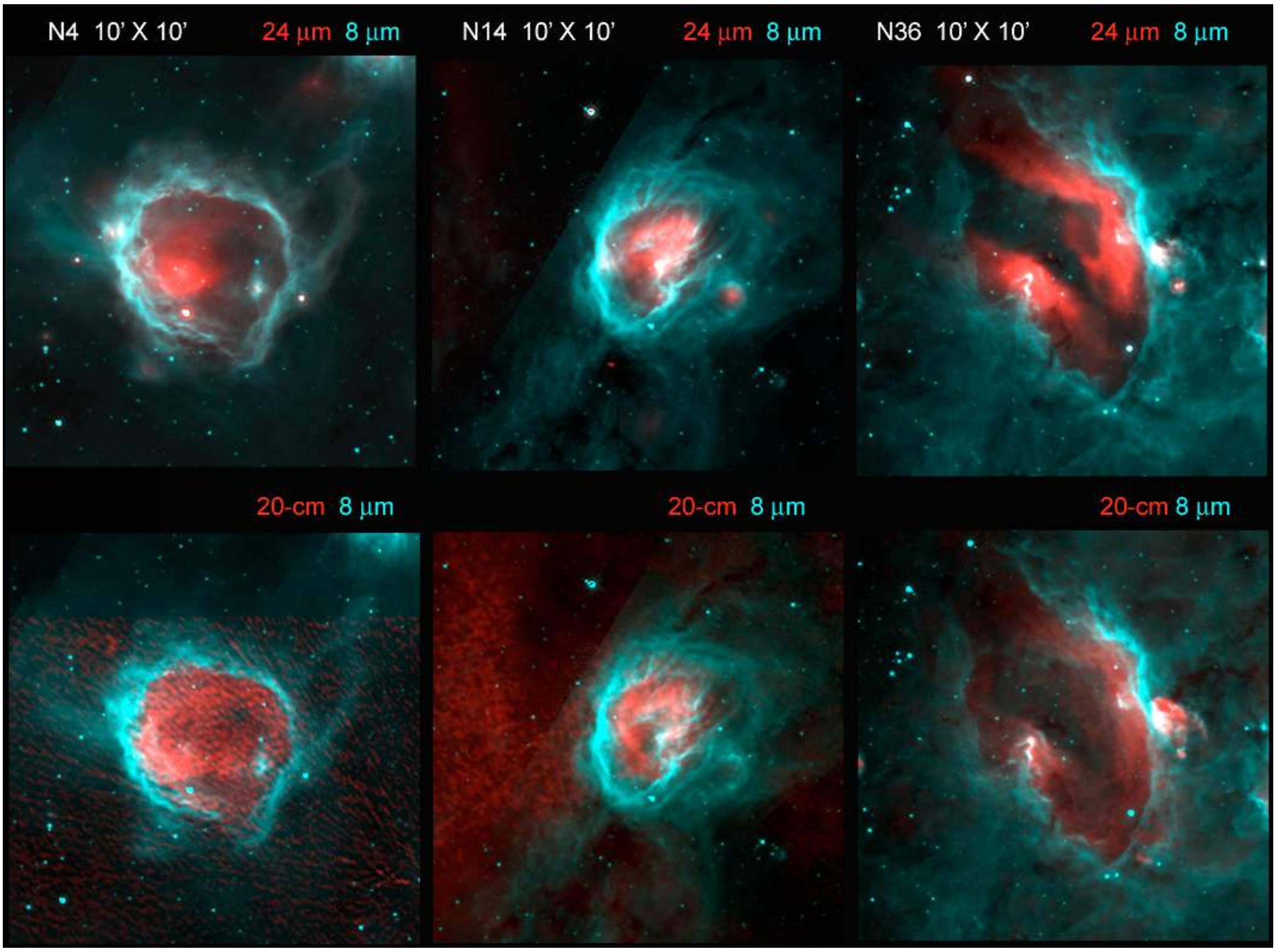

Fig. 3. Examples of three bubbles that are large in angular size. All the fields are 10′ × 10′. The colours are the same as in Fig. 2.

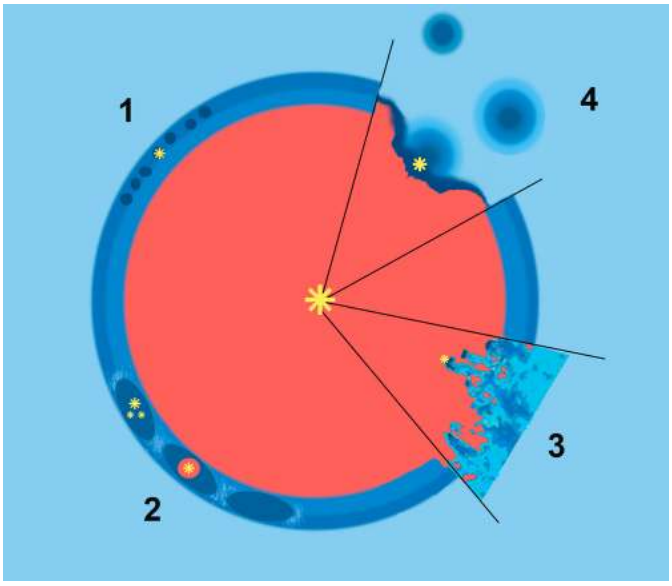

Fig. 4. Schematic view of a spherical expanding H II region and of its neutral environment. Different processes of triggered star formation are depicted: 1 – small-scale gravitational instabilities; 2 – large-scale gravitational instabilities leading to the formation of high-mass fragments; 3 – ionizing radiation acting on a turbulent medium; 4 – radiation-driven compression of pre-existing dense clumps.

The stars formed in compressed pre-existing globules should be seen in the direction of the H II region. In this paper, we try to identify only the most massive second-generation stars, which are those able to ionize second-generation H II regions.

5.1. The ATLASGAL images

We first used the interactive software sky atlas Aladin[5] to superimpose the ATLASGAL images (and isocontours) on the *Spitzer*-GLIMPSE 8.0 μm and 24 μm images. In a second step, we used the Kang IDL software[6] to superimpose ATLASGAL isocontours on GLIMPSE 8.0 μm, MIPSGAL 24 μm, and MAGPIS 20-cm data. For the GLIMPSE and MIPSGAL data, we used a logarithmic scaling to create the background images in the figures. For the MAGPIS data, however, a logarithmic scaling accentuated the noise in the images and we instead used a linear scaling. We calculated the standard deviation over each fields (σ value) using the IDL routine "mmm"[7] found in the IDL Astronomy User's Library. The lowest contour level in our figures is the 1-σ level and the contour levels increase in multiples of the 1-σ level.

---

[5] `http://aladin.u-strasbg.fr/`

[6] `http://www.bu.edu/iar/kang/`

[7] `http://idlastro.gsfc.nasa.gov/ftp/pro/idlphot/mmm.pro`

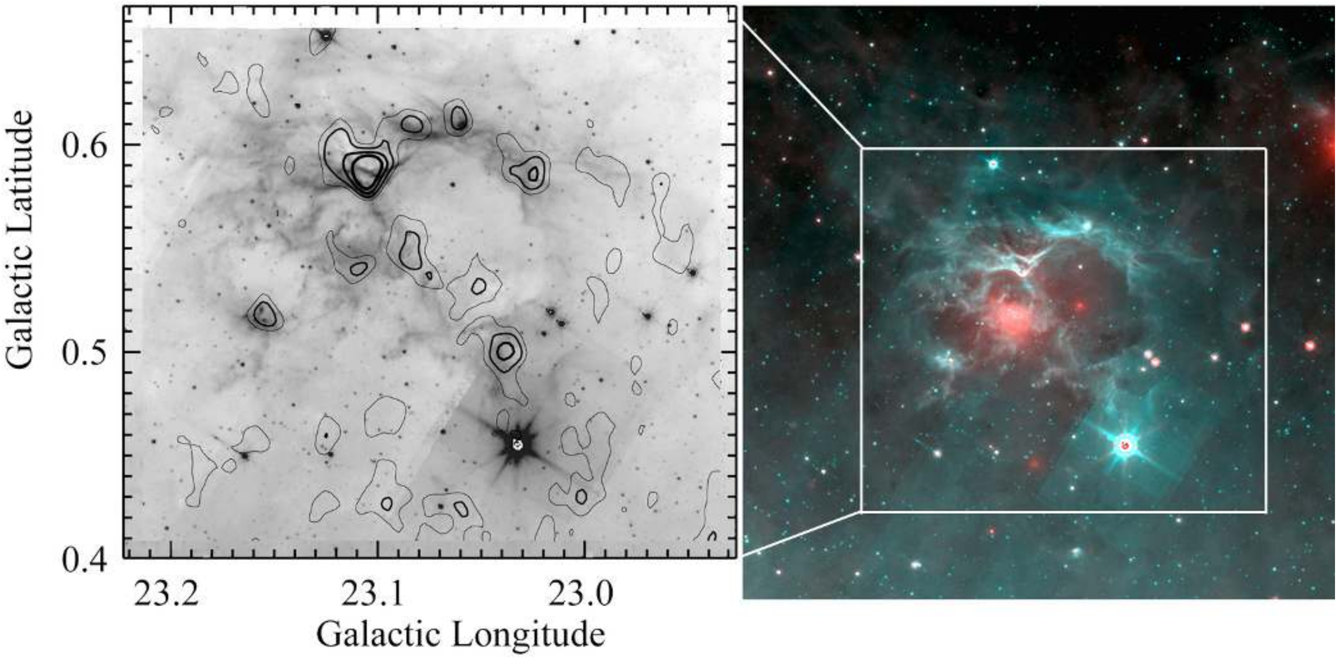

Fig. 5. N29: *left*: contours of the 870 μm emission superimposed on the 8.0 μm bubble (σ = 0.05 Jy/beam; contour levels 1, 2, 3, 5σ); *right*: *Spitzer*-GLIMPSE 8.0 μm emission in turquoise and *Spitzer*-MIPSGAL 24 μm emission in red. Several faint 870 μm condensations are present in the direction of the PDR. The brightest one (at 23.104 + 00.584) is bordered by a bright rim at 8.0 μm. Thus, it is associated with the bubble and its central H II region. This condensation probably pre-existed as it distorts the IF; it is presently compressed by the ionized gas. Some other faint condensations, near $b \sim 0.6°$, may have formed from collected material.

All of these images are available online[8]. The name of each image begins with the name of the bubble, followed by "_870+8", or "_870+24", or "_870+MAGPIS", or "_870+VGPS" to indicate the frame on which the 870 μm contours have been superimposed. For example, N1_870+8.eps, N1_870+24.eps, and N1_870+MAGPIS.eps are the images relating to the N1 bubble. The 870 μm 1-σ level is given for each field.

5.2. The distribution of dense neutral material

We must be very cautious about associating the cold dust condensations with the bubbles. A cold dust condensation observed in the direction of a bubble may not be associated with it, but may be, by chance, situated along the same line of sight. This problem can be mediated with velocity information. The velocity of the ionized gas is measured using hydrogen recombination lines. The velocities of the central H II regions, when known, are given in Table A.2 (Appendix A). The velocities of some bright dust condensations have been measured using the NH_3 (1, 1) inversion line, at Effelsberg (Wienen et al., in preparation). About 80% of these bright dust condensations adjacent to bubbles have a NH_3 velocity that differs by less than 5 km s^{-1} from that of the enclosed H II region. In addition to the velocity information, we regard the association of a dust condensation with a bubble as highly probable if we have signs of interaction between the ionized gas and the condensation (for example, the presence of a bright rim, observed at 8.0 μm, bordering the condensation and part of the ionization front). For example, the brightest condensation in N29 (Fig. 5) is clearly associated with the bubble because it is bordered by a bright rim at 8.0 μm. Finally, if a (partial) shell of dust or if numerous condensations surround the bubble we consider the association probable.

We present in Tables 1–3 our conclusions derived from the comparison between the cold dust emission, as seen by ATLASGAL, and the morphology and location of the bubbles enclosing H II regions. We consider several cases:

- The presence of a partial shell of collected material, or of numerous condensations surrounding the ionized region. The corresponding regions are listed in Table 1. Twenty-six regions (Table 1) show a shell of cold dust surrounding the bubble, or numerous condensations observed in the direction of the PDR surrounding the ionized region. These regions are good candidates for the collect process (accumulation of dense material around the ionized region during its expansion). N4 (Fig. 6), N14 (Fig. 8), and N49 (Sect. 6.5 and Fig. 18) are good examples of such regions.

- The presence of a few dust condensations in the direction of the PDR surrounding the H II region, some interacting with the ionized gas (as evidenced by bright rims seen at 8 μm). The corresponding 18 regions are listed in Table 2. The condensations presently interacting with the ionized gas may be pre-existing condensations reached by the ionization front and compressed by the ionized gas. In this case, they should protude inside the ionized region. The bright condensation in N29 (Fig. 5) was probably already present in the neutral gas before being reached by the ionization front. Some of the 18 bubbles present in Table 2 may also show condensations formed from collected material; and both types of condensation may be present around the same region. For example, the faint condensations present around N29, near $b \sim 0.6°$, probably formed from collected material. For most of these regions and condensations, it is difficult to determine which of the two processes is at work: collect and collapse or radiation-driven compression of a pre-existing condensation. Both processes can induce star formation.

---

[8] `http://lamwws.oamp.fr/bubbles`

Table 1. Bubbles as seen by ATLASGAL. Presence of collected material (partial shell or numerous condensations surrounding the ionized region).

Identification	Comments
N2	collected material along the open bubble (faint emission) + several bright condensations at one end, containing several UC and compact H II regions and two 6.7 GHz methanol masers
N4	shell of collected material
N12	several adjacent condensations, some in the direction of "fingers" or of IRDCs
N14	shell of collected material
G15.68	square bubble; shell of collected material; most of the condensations are IRDCs
N18	several faint condensations following the PDR, two UC H II regions (uncertain association)
N21	collected material (faint emission); one bright adjacent interacting condensation
N22	collected material (faint emission); two bright adjacent interacting condensations
N24	collected material (faint emission); several bright condensations, one adjacent to the N24bis1 H II region, another one surrounding the N24bis2 H II region
N24bis2	shell of collected material; a 6.7 GHz methanol maser
N29	several faint condensations along the PDR; one bright interacting condensation
N35	several faint condensations along the PDR; one interacting condensation; two nearby compact H II regions
N36	collected material + a very bright condensation containing an UC and a compact H II regions; OH, H_2O and methanol masers associated with the UC H II region
N45	several bright condensations along the PDR; one interacting condensation
N49	half a ring of collected material with massive fragments; one UC H II region on the border of the brightest fragment; two 6.7 GHz methanol masers
N50	a partial shell of collected material
N52	bright dust emission along the 8 μm filaments surrounding the bipolar nebula; very bright condensations at its "waist", containing an UC and a compact H II regions; four 6.7 GHz methanol masers
G31.16	faint emission following the PDR; one condensation in the direction of N53
N59	numerous dust condensations along the PDR; three UC H II regions in the direction of the brightest condensation; is the N58 bubble associated? is the bipolar nebula at 33.201−00.011 associated?
N65	collected material (faint emission) on the border of the two bubbles; one bright condensation with a hyper or UC H II region and a 6.7 GHz methanol maser
N68	similar to N36; several faint condensations adjacent to the PDR + a bright condensation containing an UC and a compact H II region
N69	collected material (faint emission) along the bright part of the PDR
N77	several condensations adjacent to the PDR; the brightest one in interaction with the ionized gas
N80	several condensations around the bubble
N90	several condensations around the bubble
N94	several faint condensations along the PDR; some are bordered by bright rims

Table 2. Bubbles as seen by ATLASGAL. Presence of at least two dust condensations adjacent to the PDR, with one in interaction with the ionized region.

Identification	Comments
N1	two adjacent interacting condensations between N1 and the nearby W31 H II region
N3	two adjacent interacting condensations (faint emission)
N10	two adjacent interacting condensations
N27	open bubble; one condensation elongated along the bright part of the PDR
N39	bipolar nebula; three interacting condensations at its "waist"; another bright condensation on the border, in the direction of a compact H II region (probably not associated, as shown by its velocity)
N47	several faint interacting condensations
N54	faint condensations adjacent to the PDR; the brightest one interacting with the ionized region
N60	two adjacent interacting condensations
N61	faint condensations adjacent to the PDR (collected material?); a bright adjacent condensation containing one UC and two compact H II regions (no triggering)
N62	faint emission in the direction of the PDR + a bright adjacent filament (IRDC)
N73	two adjacent interacting condensations
N74	several faint adjacent condensations; one interacting condensation
N76	several faint interacting condensations
N82	condensations elongated along the bright part of the PDR
N91	several condensations, one elongated along the bright PDR, another very bright (also an IRDC) containing an UC H II region and a 6.7 GHz methanol maser
N93	two condensations adjacent to the PDR (one in interaction)
N95	several condensations along the bright PDR
N98	a bright interacting dust filament extended along the PDR

Table 3. Bubbles as seen by ATLASGAL. Presence of at least one dust condensation in the direction of the bubble or adjacent to it (the association condensation – bubble may be uncertain).

Identification	Comments
N8 & N8bis	one elongated bright condensation, a 24 μm source in the center, N8 and N8bis on each side
N9	one bright adjacent condensation
N13	at the tip of a dust filament
N16	one interacting adjacent condensation; also an IRDC
N20	one bright adjacent condensation
N23	between two condensations, along a bright fragmented filament
N24bis1	one bright adjacent condensation, with an UC H II region in its center
N25 & N25bis	one adjacent bright condensation
N26	two faint adjacent condensations
G19.82	a bright adjacent condensation
N28	an adjacent condensation (also a filamentary IRDC)
N31	two faint adjacent dust condensations
N32	one bright adjacent condensation containing an UC H II region
N33	an adjacent condensation
N34	one filament crossing the bubble
N37	one adjacent interacting condensation
N40	one adjacent filament (also an IRDC), with several fragments
N41	one adjacent dust condensation
N42	one dust condensation in its direction
N43	one bright adjacent condensation
N44	two condensations, one in its direction and one adjacent
N46	two faint adjacent condensations
N48	one bright adjacent condensation (also a filamentary IRDC)
N51	faint condensations
G30.25	faint adjacent condensation
N53	two faint adjacent condensations; N53 lies on the border of the large G31.165−0.127 bubble
N55	a bright condensation along an adjacent filament (IRDC); three H II regions within the condensation (no triggering)
N56	one condensation in its direction
N57	one adjacent condensation
N58	one bright condensation in its direction
N64	several faint nearby condensations (also IRDCs)
N64bis	one adjacent condensation
N66	one condensation in its direction
N67bis	one bright condensation in its direction, containing two UC H II regions
N70	one adjacent bright condensation, containing an UC H II region in its center
N71	several faint condensations
N72	a bright adjacent condensation (also a filamentary IRDC)
N75	two adjacent condensations
N78	one bright condensation in its direction
N79	one adjacent condensation
N83	one condensation in its direction
N84	two adjacent condensations
N85	one adjacent condensation containing an UC H II region
N86	one adjacent condensation
N87	one adjacent condensation
N89	a faint adjacent condensation
N92	one filamentary condensation (also an IRDC) crossing the nebula
N96	a condensation in its direction; N96 lies on the border of the large N97 bubble

- Presence of a cold dust condensation, often bright, in the direction of the H II region or adjacent to it. The association is most often uncertain: velocities are missing and/or we lack the angular resolution to see the signatures of collected material or of interactions with the ionized gas. The corresponding regions are listed in Table 3.

Forty-seven bubbles are listed in Table 3; most of them are of small apparent size (and thus are either young or distant). In the absence of velocity measurements, the association between the bubbles and the dust condensations is uncertain; this is the case for N8 and N25 (Fig. 7). For angularly small bubbles, we also lack the angular resolution required to assess whether the bubbles and the condensations are interacting (this applies to 70% of these 48 regions). These dust condensations may be massive, and they often contain several massive young objects (UC H II regions, 6.7 GHz methanol masers). The bright condensations adjacent to N25 (Fig. 7), N32 (Sect. 6.1, Fig. 9), or N67bis (Sect. 6.6, Fig. 25) are good illustrations of such a configuration.

- A few bubbles have very faint, or lack entirely, associated 870 μm cold dust emission. They are N11, N65bis, and N67. Furthermore, two large bubbles with very faint dust emission present a clearly associated compact H II region at their periphery. They are N81 (with the compact H II region enclosed by N82, Fig. 22), and N97 (with N96).

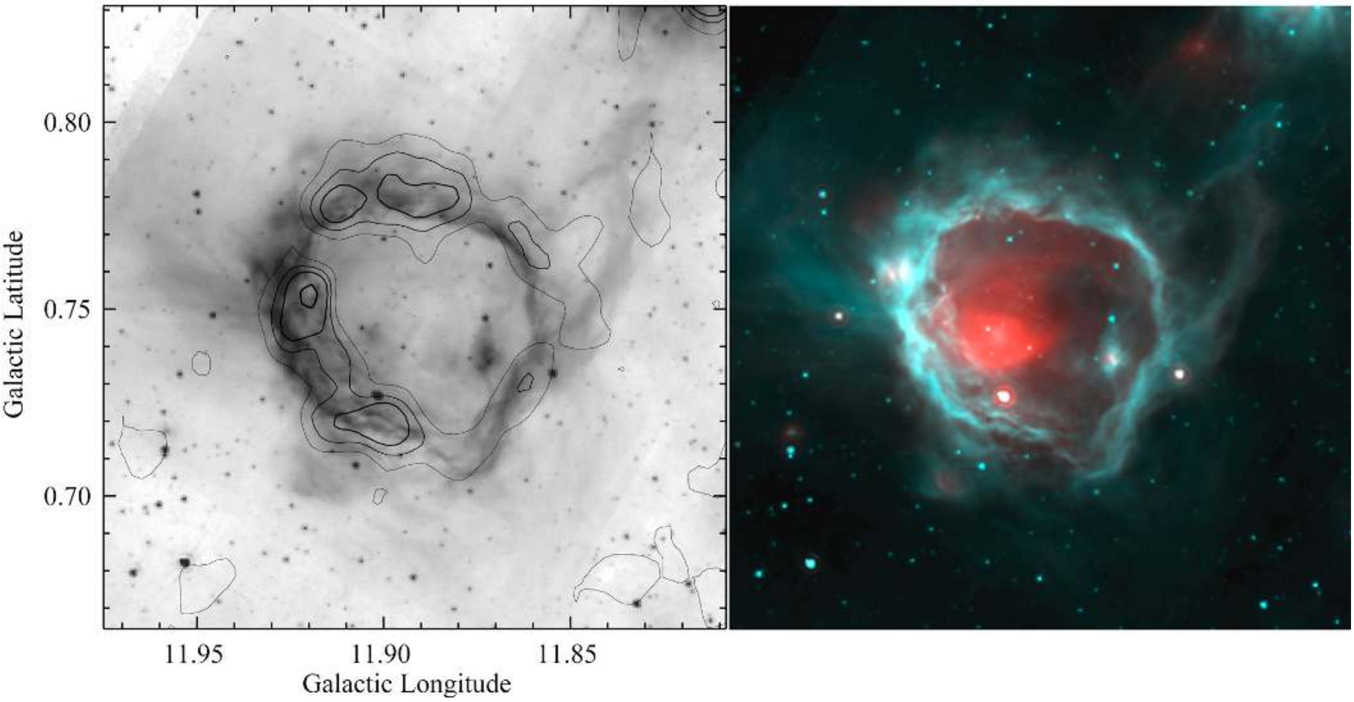

Fig. 6. N4: this bubble is surrounded by a shell of collected material. Its mass is ~1150 $M_{\odot}$ (for D = 3.14 kpc). *Left*: contours of ATLASGAL 870 μm emission superimposed on the *Spitzer*-GLIMPSE 8.0 μm bubble (σ = 0.04 Jy/beam; contour levels 1, 3, 5, 10, 15σ); *right*: *Spitzer*-GLIMPSE 8.0 μm emission in turquoise and *Spitzer*-MIPSGAL 24 μm emission in red.

To conclude, for the 65 H II regions enclosed by bubbles and for which the angular resolution of the observations is high enough to study the spatial distribution of cold dust, 26 (40%) are clearly surrounded by collected material, and 18 more (28%) show interacting dust condensations and also possibly condensations formed from collected material. For 16 regions (24%), the association between the bubble and the condensations is uncertain, and 5 regions (8%) have no detectable associated dust emission.

At least 16 bubbles contain a compact or ultracompact H II region (or several of them; detected via their radio and 24 μm central emission) in the direction of their PDRs. These regions are good candidates for triggered massive-star formation. They are identified in Tables 1 and 2, and are discussed in Sect. 6.5.

6. Discussion

We now address the morphology of the bubbles (whether it is influenced by their environment), their dust content (PAHs and hot dust), and their CO environment. We then discuss massive-star formation at their borders, possibly triggered by the enclosed H II regions.

We require the distance of the bubbles to estimate parameters such as the size or the mass of the associated dust condensations. Their distances, when available, are given in Appendix A, Table A.2. CH06 "emphasize that the near distances are most likely the correct ones" (the argument is that nearby bubbles are more easily detected because distant ones are masked by the foreground emission of the Galactic plane). However this is not true: the kinematic distance ambiguity has been resolved for 57 bubbles in our sample; 39 of them (68%) lie at the far distance, whereas only 15 (26%) of them are located at the close-by position (3 are at the tangent point).

In the following, we use the 870 μm cold dust emission to estimate the amount of neutral material associated with the bubbles. We give in Appendix B the relations used to derive the column density $N(H_2)$ and the mass of a condensation from the observed surface brightness $F_{870\ \mu\mathrm{m}}$.

6.1. The morphology of the bubbles

We categorized a few different types of bubbles:

- Nearly complete bubbles such as N1, N4 (Fig. 3), N8, N12, N13 (Fig. 2), N23, N26, N28, N42 (Fig. 2), N43, N44, N49, G30.250, N53, N57, N58, N66, N70, N74, N75, N78, N80, N83, N86, N90, and N93. As mentioned in Sect. 2, the interstellar medium is not homogeneous on large scales. In an inhomogeneous medium, there are density gradients and therefore maintaining circular symmetry over large scales would seem unlikely. Circular bubbles should therefore be of small size, and thus should be either young or evolving in a very dense medium that restricts their expansion. Many of the complete bubbles are indeed small, such as N13 (diameter ~ 0.85 pc), N58 (0.95 pc), and N83 (1.7 pc) – all three of which are seen in the direction of bright cold dust condensations and thus are probably associated with dense material. However, N1 (diameter ~ 7.8 pc), N4 (3.5 pc), N43 (2.6 pc), N49 (4.0 pc), N53 (4.5 pc), N70 (6.6 pc), and N93 (3.8 pc, if at the distance of N94) are medium-sized H II regions. Why are they so circular? The most obvious answer is that these regions evolve in a rather homogeneous medium (on the scale of a few parsecs), where the turbulence – at the origin of most inhomogeneities – is low.
- Some bubbles are elongated, probably in the direction of lower density, and are possibly in the process of opening (see, for example, N10, N14 (Fig. 3), N29, N50, and N77). These bubbles are, in general, well-defined on the side of high density (where we see adjacent dust condensations). For example,

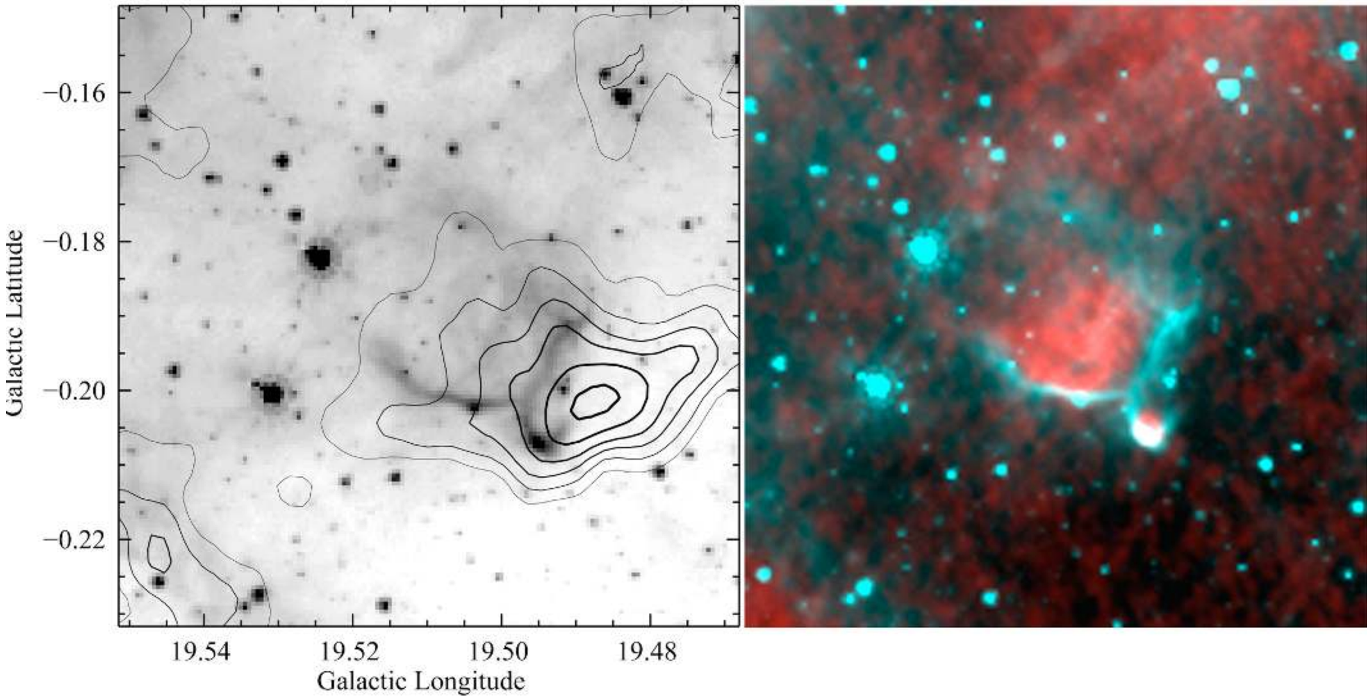

Fig. 7. N25. *Left*: contours of the 870 μm emission superimposed to the 8.0 μm bubble (σ = 0.06 Jy/beam; contour levels 1, 3, 5, 7, 10, 14σ); *right*: *Spitzer*-GLIMPSE 8.0 μm emission in turquoise and MAGPIS 20-cm emission in red. N25 is adjacent to a bright condensation. The bubble is bright on the side of the dense material, and opens on the low-density side. But we lack angular resolution to get details about the distribution of neutral material wih respect to the bubble.

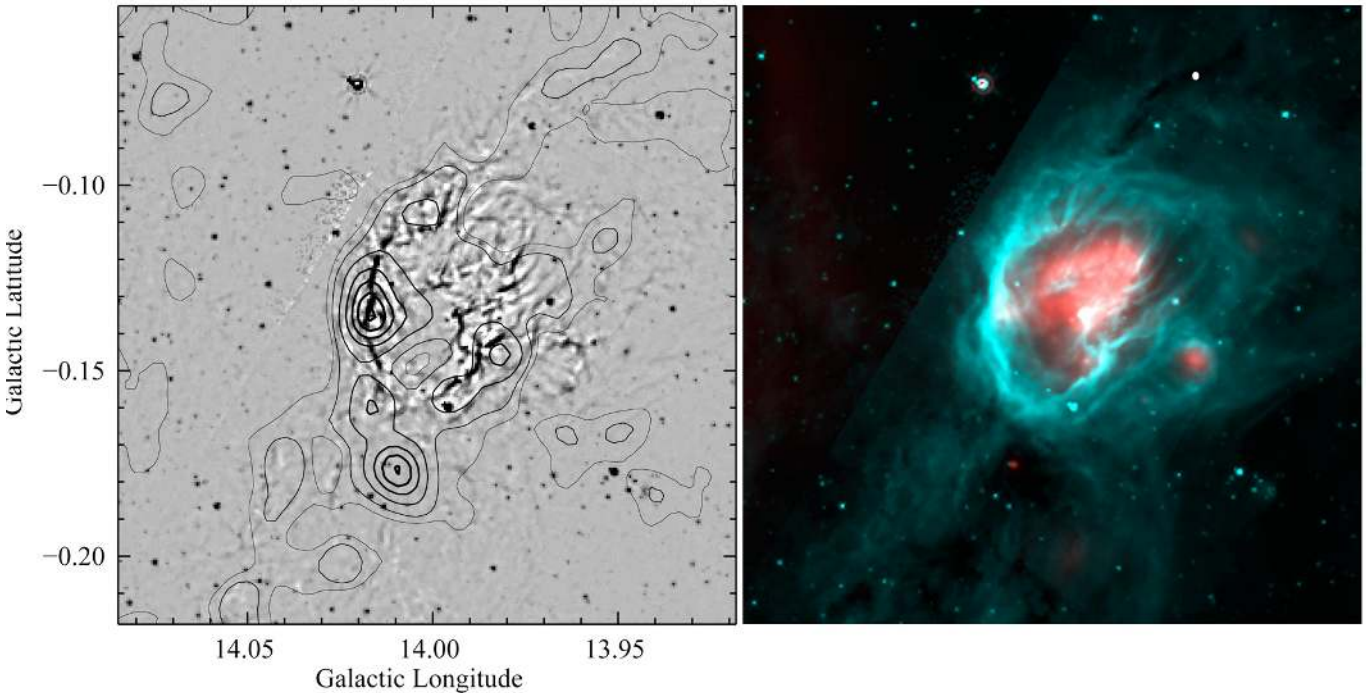

Fig. 8. N14, a bubble possibly in the process of opening. The bubble is bright where it is adjacent to dense material, and opens in the direction of low density. *Left*: contours of the 870 μm emission superimposed on an unsharp-masked image at 8.0 μm. We see the filaments shaped at the surface of the bubble by the ionized gas flowing out (870 μm emission: σ = 0.04 Jy/beam; the contour levels are 1, 2, 5, 10, 15, 20, and 25σ); *right*: *Spitzer*-GLIMPSE 8.0 μm emission in turquoise and *Spitzer*-MIPSGAL 24 μm emission in red.

N14 (Fig. 8) is surrounded by a partial shell of dense material, and opens in the direction free of dense material. The bubbles N24bis1, N25 (Fig. 7), G19.821, and N32 (Fig. 9) are adjacent to one bright dust condensation. They are well-defined on the side of the condensation, and open on the opposite side, presumably towards the low-density region.

- Some bubbles are open in one direction, such as N2 (Sect. 6.5, Fig. 15), N16, N21, N24 (wide opening, Fig. 16),

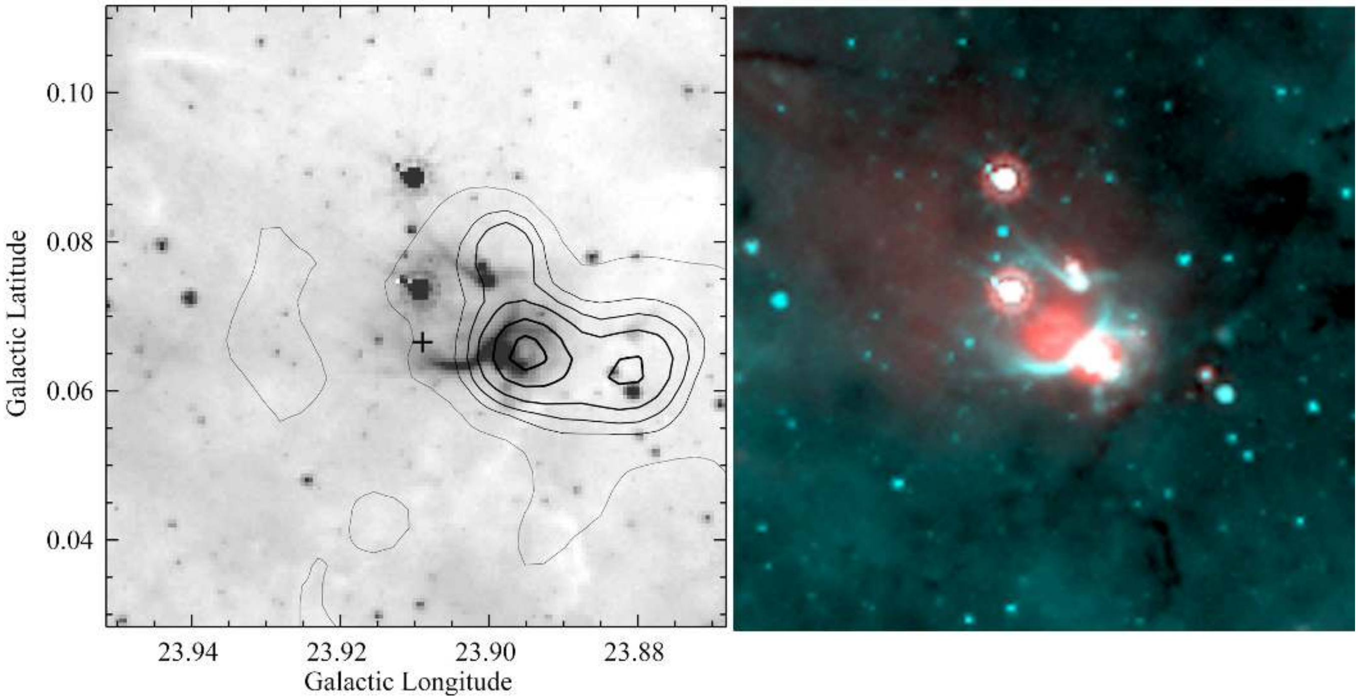

Fig. 9. N32. *Left*: contours of the 870 μm emission superimposed on the 8.0 μm image. The cross gives the position of a methanol maser. *Right*: *Spitzer*-GLIMPSE 8.0 μm emission in turquoise and *Spitzer*-MIPSGAL 24 μm emission in red. The comparison of the velocity of the condensation with that of the H II region suggests an association; the condensation at 23.8955+00.0638 has a velocity of 39.25 km s^{-1} whereas the H II region has a velocity of 32.8 km s^{-1} (Table A.2).

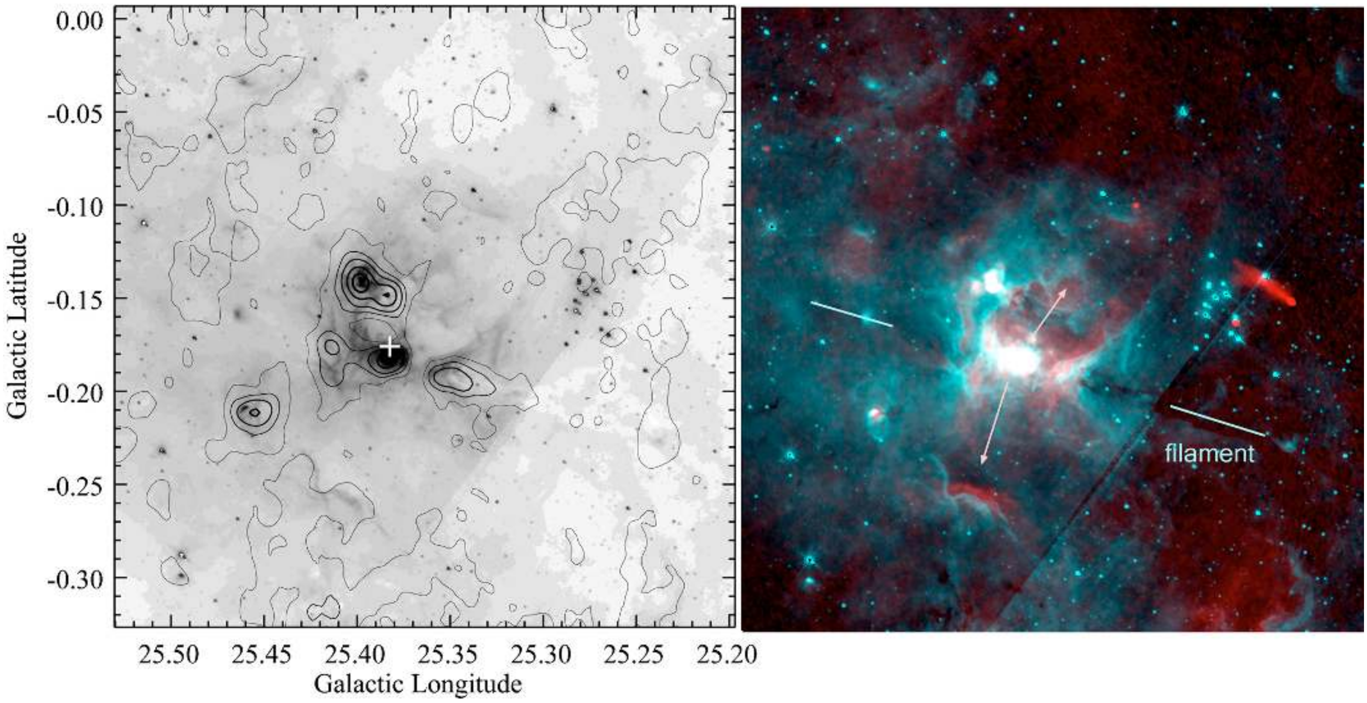

Fig. 10. N39, a bipolar nebula: *left*: contours of the 870 μm emission superimposed on the *Spitzer*-GLIMPSE 8 μm image. The white cross gives the position of a methanol maser. *Right*: *Spitzer*-GLIMPSE 8.0 μm emission in turquoise and MAGPIS 20-cm emission in red. The blue line shows the remains of the filament (or the sheet seen edge on) inside which the exciting star(s) of N39 possibly formed. The red arrows show the probable preferential directions of expansion of the ionized gas.

N27, N36 (Fig. 3), N37, N91, N92, N94, and N97 (wide opening). They are often of large size, such as N2 (38 pc × 19 pc, at a distance of 6.0 kpc), N16 (33 pc × 19 pc, at D = 13.7 kpc), N24 (≥30 pc, at D = 4.6 kpc), N36 (16 pc × 8 pc, at D = 6.4 kpc), N37 (16 pc × 9 pc, at D = 12.6 kpc), N91 (31 pc × 19 pc, at D = 8.1 kpc), and N97 (20 pc × 11 pc, at D = 9.3 kpc). A large size may be indicative of either evolution in a low density medium or an old age. An H II region of radius 10 pc, excited by an O6V star, may for example be 3.5 Myr old if evolving in a medium of 10^3 cm^{-3}, or 1 Myr old if evolving in a medium of 10^2 cm^{-3}.

- Two bubbles (N39 and N52) are part of bipolar nebulae. N39 (Fig. 10) has three 870 μm condensations aligned along a filament. This filament is seen farther away from the bubble as an infrared dark cloud (IRDC; line in Fig. 10). A possible scenario is the following: the massive star or cluster exciting the nebula formed inside this filament. Later, the expanding H II region broke through the edge of the cloud, simultaneously in two directions, producing a bipolar nebula (arrows). This scenario was simulated by Bodenheimer et al. (1979, their Fig. 4). A bipolar nebula is also obtained when an H II region forms and expands near a dense filament, as simulated by Fukuda & Hanawa (2000). Their simulation shows that a gravitational instability is induced to form dense cores along the filament, on each side of the ionized region (their Fig. 1). This is another process by which an expanding H II region can trigger star formation. In the case of N39, Fig. 10 shows the presence of two condensations at the waist of the bipolar nebula, along the filament, in the directions 25.410−00.176 and 25.351−00.191. A similar situation can explain the N52 morphology (Sect. 6.5, Figs. 19). In both nebulae, a 6.7 GHz methanol maser is present in a condensation situated at the waist of the nebula, indicating that star formation is at work there. Two percent of the bubbles appear to be bipolar. If, as suggested by Beaumont & Williams (2010; see Sect. 6.4), most molecular clouds were flat, more bipolar nebulae should be observed. We note however that an H II region appears to be bipolar only when the line of sight is not too inclined with respect to the plane of the parental molecular cloud.

The inside boundary of many bubbles (in addition to the ionization front of the enclosed H II regions) exhibits structures, such as 8 μm bright rims bordering condensations protruding inside the ionized regions, or pillars (also called fingers or elephant trunks). The N12 bubble, which is almost circular, displays such a bumpy IF (Fig. 11), as do the IFs of N35, N36 (Fig. 17), N68, N76, and N91 (Fig. 23). These structures are the signatures of small-scale density inhomogeneities in the medium surrounding the bubbles. These inhomogeneities are probably due to turbulence. The HD simulations of H II regions expanding in a turbulent medium by Mellema et al. (2006), Gritschneder et al. (2009), and Arthur (2009) reproduce rather well the appearance of these IFs.

One of the bubbles is not circular, but square (G15.68−00.28). It is surrounded by a shell of collected material that follows the four sides of the square and appears as IRDCs. The MHD simulations of Arthur (2010) of an H II region, excited by a B star, evolving in a magnetised medium show that the magnetic pressure is able to straighten the ionization front. Could a similar scenario explain the very peculiar shape of G15.68−00.28?

All these examples show that the birth and evolution of the bubbles, and their present morphology, are strongly influenced by their environment. Their environment plays a role at the time of their birth, whether at the center or at the edge of a dense core, or in a filament or a sheet; it also plays a role during their expansion phase, in media with density gradients and/or turbulence.

6.2. The distribution of PAHs as observed at 8.0 μm

Several spectroscopic observations show that the PAH emission bands are faint or absent in the direction of H II regions, suggesting that PAHs are destroyed inside the ionized region. Cesarsky et al. (1996) present ISOCAM spectra of the M17 H II region and find that the spectrum obtained in the direction of the adjacent molecular cloud displays the PAH emission bands, whereas the spectrum obtained in the direction of the ionized region is clearly dominated by the continuum emission (the 7.7 μm and 8.6 μm PAH features are almost absent). This observation has been confirmed by *Spitzer*-IRS spectra of M17 (Povich et al. 2007). Lebouteiller et al. (2007) present *Spitzer*-IRS spectra of the giant H II region NGC 3603. They compare the intensity of the PAH emission bands with that of the underlying continuum which is attributed to VSGs. They find that the PAH/VSG ratio is anticorrelated with the hardness of the radiation field, which implies that a destruction mechanism operates on the PAH molecules within the ionized gas. The PAH emission band at 3.3 μm has been mapped in the Orion bar (a nearby edge-on PDR) with a resolution of 1″ (Giard et al. 1994). The map shows a sudden drop of the 3.3 μm emission feature at the ionization front, toward the H II region. The spatial extent of the transition zone is not resolved and is thus thinner than 2.5×10^{-3} pc.

The destruction of PAHs in hard radiation fields, such as those present in H II regions, has been discussed by several authors (see Tielens 2008, and references therein). Processes involving the photodissociation of PAHs, for example by the loss of an acetylenic group, show that small PAHs of fewer than about 50 carbon atoms are destroyed by the radiation field in H II regions, but that larger PAHs may survive (Allain et al. 1996a,b). This process also involves photons with energies less than 13.6 eV, and thus the PAH destruction does not occur exactly at the limit of the ionized region. PAHs may be doubly ionized in H II regions, and charge separation reactions (also called Coulomb explosions or dissociations) do occur; this is another PAH destruction process (Leach 1989). However, here again, photons with energy near 13.6 eV or higher are not directly involved. Chemisputtering by H^+ seems a promising PAH destruction process in H II regions, as proposed by Giard et al. (1994) or Normand et al. (1995), because it relies on the large abundance of free protons found in H II regions. (It was proposed by Barlow & Silk 1977, for the destruction of graphite grains; and Omont 1986, proposed that it was also valid for PAHs.) However, the study by Micelotta et al. (2010) of the interaction of PAHs with electrons or ions (H^+ and He^+) in a hot or warm gas shows that PAH destruction is dominated by He^+ collisions at a temperature lower than 30 000 K, thus is dominant in H II regions.

Many bubbles in our sample show that the carriers of the IR bands responsible for the emission in the *Spitzer*-IRAC band at 8.0 μm are destroyed inside the ionized region. For these bubbles, the 8.0 μm emission stops where the 20-cm radio continuum emission begins. This phenomenon is observed in H II regions excited by both massive, and also less massive stars. For example, it is observed in: i) RCW 79, which is excited by a cluster of early O-stars (Martins et al. 2009), and in N49, which is excited by an O5V star (Watson et al. 2008); ii) RCW 120, which is excited by an O8V star (Zavagno et al. 2006) and in N4, which is excited by an O8V star (an estimation based on a radio flux of 2.02 Jy at 11-cm, Reich et al. 1984, and a distance of 3.14 kpc); iii) RCW 82, which is excited by two late O-stars (Martins et al. 2009). It is also observed in bubbles enclosing regions of very faint/or absent radio emission (as N8). Thus, the destruction of PAHs does not require photons more energetic than necessary to ionize hydrogen. This differs from the conclusions of Lebouteiller et al. (2007), who state that energies higher than 27.6 eV (the ionization potential of Ar^+) are required to destroy PAHs containing more than 50 carbon atoms. Their argument, based on observations of NGC 3603, is that PAH emission

Fig. 11. N12: *left*: colour image with the *Spitzer*-GLIMPSE image at 8 μm in turquoise and the *Spitzer*-MIPSGAL image at 24 μm in red. This bubble appears, at first glance, to be rather circular; but the ionization front that limits the central cavity shows many structures. This is indicative of density inhomogeneities in the medium surrounding the bubble. *Right*: synthetic optical image of a simulated H II region evolving in a turbulent molecular cloud (Henney et al. 2010). The [NII] 6584 Å emission appears in red, the Hα 6563 Å emission in green, and the [OIII] 5007 Å emission in blue.

is observed in regions where Ar^+ is present. The morphology of NGC 3603 is more complicated than that of the bubbles studied here, and regions with very different physical conditions can contribute to the emission along one line of sight, this effect blurring the general picture.

In conclusion, PAH emission is observed in the direction of the PDRs, outside the ionized region, independent of the hardness of the radiation field of the exciting stars (at least from early to late O stars). This indicates that the PAHs are destroyed in the H II regions. The destruction mechanism(s) remains uncertain.

6.3. The extended dust emission at 24 μm

Extended 24 μm emission associated with the bubbles is observed in two locations. First, it is seen in the direction of the center of the bubbles. This emission is often bright. Spectroscopy of H II regions (Roelfsema et al. 1998; Peeters et al. 2002) shows that no strong nebular emission lines are present in the 24 μm band; the emission is mostly from the continuum. This emission can only be attributed to dust. Therefore, hot dust grains must be present in the ionized region, not far from the exciting stars. Emission at 24 μm is also observed in the direction of the dense PDR filaments that are also observed at 8.0 μm and delineate the bubble. This emission is rather faint. We lack the resolution required to determine whether the 24 μm and 8.0 μm emission observed in the direction of the PDRs are cospatial.

There are several possible origins of the 24 μm emission. Désert et al. (1990) showed that the cirrus continuum emission near 25 μm was due, in almost equal proportions, to PAHs and VSGs. (VSGs have a size in the range 1 nm to 10 nm, and are probably carbon dominated.) These small particules (PAHs and VSGs) are out of thermal equilibrium: they reach very high temperatures (up to several hundreds of K) after absorbing high-energy photons and radiate in the near- and mid-IR. In the direction of the PDRs surrounding H II regions, the radiation field hardens. It has been shown, for example by Compiègne et al. (2008) for the PDR tracing the Horsehead nebula, that the abundance ratio of PAHs to VSGs varies. Emission from VSGs dominates the continuum emission near 24 μm. But what happens inside H II regions where the stellar radiation field is very intense and hard? What kind of grains can survive in this very harsh environment?

The 24 μm continuum emission in H II regions may alternatively be caused by big dust grains (BGs) in thermal equilibrium (BGs have a size of a few tens to a few hundreds of nm, and are mainly formed of coated silicates). Cesarsky et al. (2000) discussed mid-IR imagery and spectroscopy obtained with the ISO satellite of a region in the Orion Nebula. The images show extended emission from amorphous silicate grains from the entire H II region (ionized mainly by $\theta^{\ 1}$ Ori, an O6 star), and from around θ^2 OriA (an O9.5V star). The spectra peak near 25 μm; Cesarsky et al. have demonstrated that, at these wavelengths, the emission comes mostly from amorphous silicate grains of temperatures 85 K to 145 K, with a small contribution from amorphous carbon grains of temperatures 110 K to 200 K.

Thus, the mechanism behind the 24 μm emission in H II regions is not clear. There are, however, several interesting properties of the 24 μm emission:

- The integrated 24 μm flux from within the ionized regions represents half or more of the total 24 μm emission of the bubbles. We measured the fraction of 24 μm emission coming from the central ionized region for selected well-defined bubbles. The ratios (flux from the ionized region)/(flux from the ionized region + flux from the PDR) are 0.50 for N4, 0.51 for N13, 0.65 for N21, 0.49 for N25, 0.51 for N42, 0.66 for N49, and 0.60 for N70.

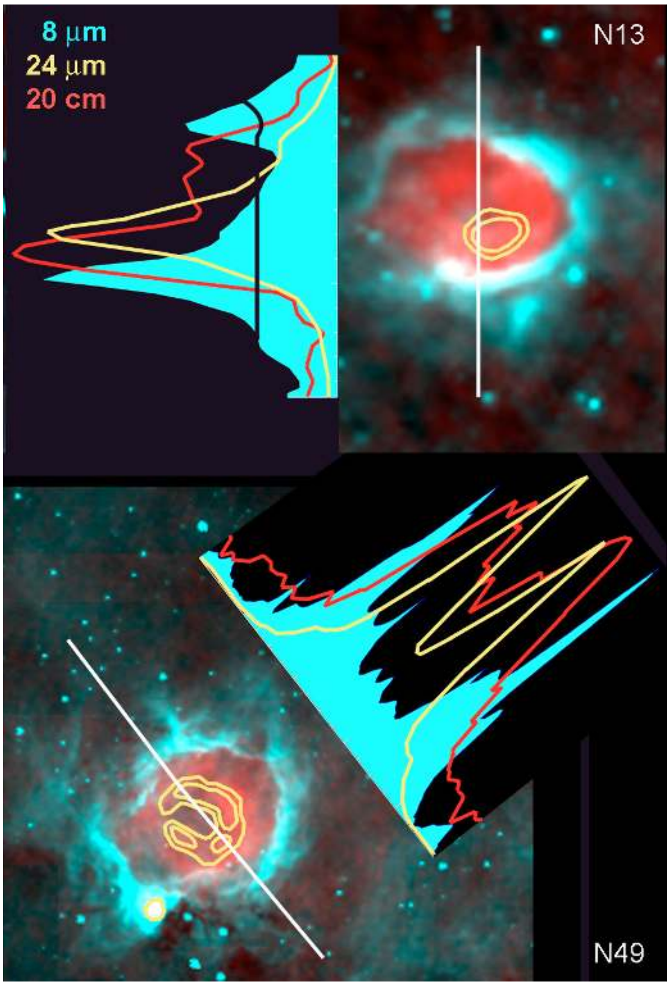

Fig. 12. Variation in the 8.0 μm, 24 μm, and 20-cm brightness along the diameter of N13 and N49. The colour images are a composite of 8.0 μm (turquoise) and 20-cm emission (red). Yellow contours show the regions of maximum 24 μm emission. The 24 μm emission is more central than the 20-cm emission.

- In several bubbles, the observed 24 μm emission is more central than the radio continuum emission; the ratio (surface brightness at 24 μm)/(radio continuum brightness at 20-cm) peaks at the very center of the bubbles. This is illustrated in Fig. 12, which compares the 24 μm and 20-cm brightness in the N13 and N49 bubbles. The ratio of the flux densities $S_{24\,\mu}/S_{20-cm}$ averaged over the whole regions is respectively 30 and 97 for N10 and N49. This ratio varies by a factor of more than 5 from the outside to the center of the H II regions. The same situation is observed in N21, N25, N42, and N70. The simplest explanation is that this effect is due to the dust temperature, which is higher near the radiation source. Inside the ionized region, dust grains can be heated by Lyman α photons, and/or directly by the Lyman continuum radiation of the central exciting stars. That the 24 μm emission is centrally peaked favours the explanation that the grains are mostly heated by absorption of Lyman continuum photons, which are more numerous near the exciting star (Lyman α photons, more uniformly distributed inside the ionized region, would probably not produce this effect). However, using the 24 μm emission alone, we cannot determine wether it is caused by VSGs out of equilibrium or by BGs in equilibrium. Additional observations at longer wavelengths are required to answer this question.

- Figure 13 allows us to compare, in the well-defined N4 bubble, the distribution of dust grains responsible for the *Spitzer*-MIPSGAL 24 μm and 70 μm emission (both bands trace thermal emission from dust grains). It shows that the grains responsible for this emission are not co-spatial. The 70 μm emission is not central, but resembles the 8.0 μm emission; it comes from the PDR rather than from the central ionized region. This confirms that the dust grains located inside the ionized region are very hot, as their emission is stronger at 24 μm than at 70 μm.

Regardless of its origin (VSGs or BGs), the emission at 24 μm from the center of bubbles is important for another reason: it allows us to locate the central exciting stars (assuming that the 24 μm emission comes from hot dust close to the exciting star). The presence of a small central hole, sometimes observed in this emission, may be the signature of stellar winds emitted by the exciting star(s). These points are illustrated and discussed in Martins et al. (2009). Alternatively, the holes may be produced by the radiation pressure of the central stars. In either case, the hole indicates the location of the exciting stars. One example of a bubble showing a central hole in both the radio-continuum emission and the 24 μm emission is N49. It has been shown by Watson et al. (2008) that the exciting star of N49 could be an O5V star lying in the direction of the hole.

Three bubbles of small angular size, N8bis, N9, and N48, display central 24 μm emission but no central radio-continuum emission. What is their nature? There are two possibilities. First, they may be H II regions with faint radio continuum emission that is undetected by MAGPIS or the VGPS. This implies that they are either distant, of low electron density, or excited by B1 or B2 stars. Alternatively, if they are not H II regions, they must contain a rather massive star because they contain hot dust. The massive star must be later than B2, or it would have created an H II region.

6.4. The CO environment of the bubbles

Beaumont & Williams (2010; hereafter B&W) mapped 38 bubbles from our sample in the $J = 3{-}2$ line of ^{12}CO, and 6 in the $J = 4{-}3$ line of HCO$^+$, with an angular resolution of 16″; these bubbles are identified in Table A.1. Their study provides information about the molecular environment, the three-dimensional morphology and the column density and density of the material surrounding the bubbles. According to B&W, the ^{12}CO (3−2) emission most likely originates in regions that are moderately dense ($n(\mathrm{H_2}) \sim 10^3{-}10^4$ cm^{-3}) with temperatures in the range 20−50 K. The HCO$^+$ (4−3) emission traces higher density regions ($n(\mathrm{H_2}) \geq 10^5$ cm^{-3}) where star formation takes place.

One feature showed by this study is the paucity of CO emission towards the center of the bubbles. If the bubbles were two-dimensional projections of spherical molecular expanding shells, we would expect to see the front and back faces of the shells as relatively faint blueshifted and redshifted emission regions, but this emission is not observed. B&W (2010) conclude that most bubbles are not spherically symmetric, but rather rings formed in flattened molecular clouds, with a thickness of a few parsecs. We have shown in Sect. 6.1 that some of the bubbles are open towards the side of low density. Thus, we agree that the front or back sides (or both) of some bubbles may be missing, but is this a general feature? If most molecular clouds had a thickness of a few parsecs, as predicted by B&W, numerous bipolar nebulae should be observed, which is not the case. However, the bubbles in the GLIMPSE sample (CHU06) are quite eccentric, with an eccentricity peaking at 0.65. This is

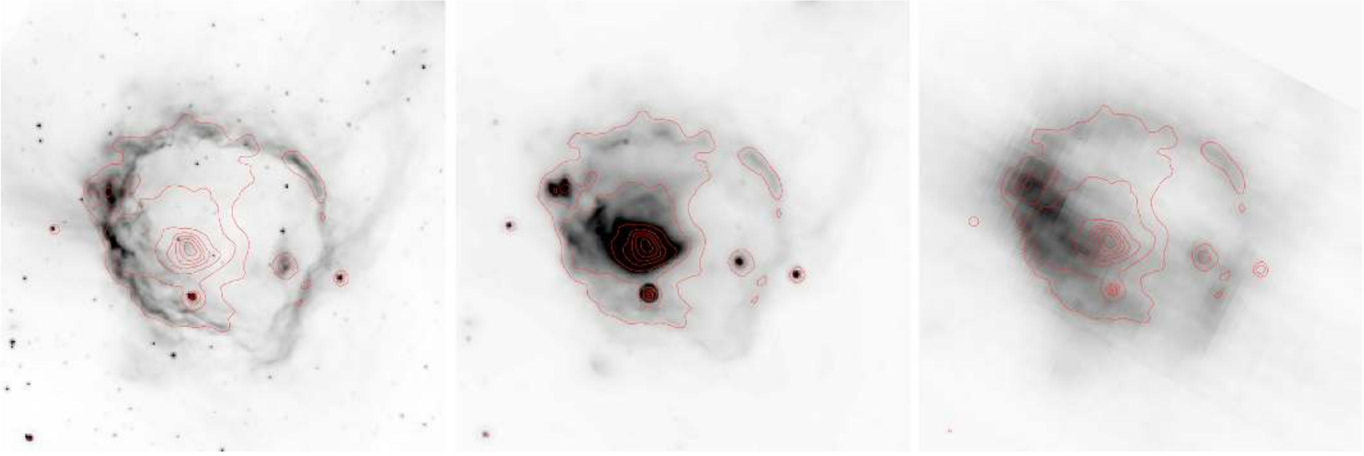

Fig. 13. N4: comparison of the distribution of various types of dust grains; *left*: emission of the PAHs at 8.0 μm from the PDR. *Middle*: emission at 24 μm of the hot grains from the ionized region (the red contours correspond to this emission). *Right*: emission at 70 μm from colder grains, distinct from these emitting at 24 μm, and probably situated in the PDR.

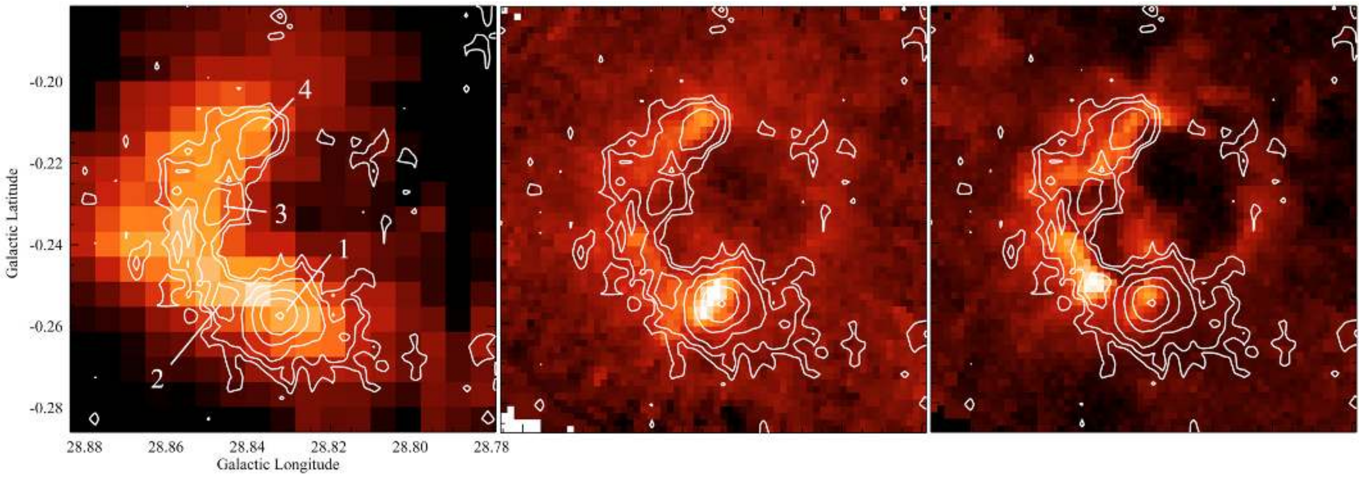

Fig. 14. The CO environment of N49: the 870 μm contour levels (0.1, 0.2, 0.5, 1.0, 1.5, and 2.0 Jy/beam) are superimposed on the Galactic Ring Survey ^{13}CO (1−0) emission (Jackson et al. 2006) integrated over all velocities (*left*), on the B&W ^{12}CO (3−2) emission integrated over the velocity (*middle*), and on the B&W ^{12}CO (3−2) peak intensity map (*right*). The dense dust condensation #1 is almost absent from the CO peak intensity map, whereas condensation #2, associated with the UC H II region, is bright (presumably a temperature effect). The CO (1−0) and (3−2) emissions integrated over velocity are more similar to the 870 μm emission. However, the dust condensation #1 is much brighter at 870 μm than it is in CO.

indicative of anisotropy, and in turn of either density gradients, a magnetic field, or a flat (two-dimensional) bubble morphology.

Another result of the B&W (2010) study are the low values estimated for the column densities of the molecular material surrounding the bubbles. The measured H_2 column densities are in the range $5{-}10 \times 10^{20}$ cm^{-2}, averaged over the dense regions with HCO$^+$ emission. These low column densities led the authors to claim that the conditions for star formation are not met in the immediate vicinity of the bubbles.

The CO (3−2) maps presented by B&W in their Fig. 1 show the CO peak intensity and appear to be very different from the 870 μm maps. The peak intensity maps show the regions where the CO kinetic temperature is high, at the borders of the H II regions, hence clearly define the bubble boundaries. Maps of CO emission integrated over all velocities are more comparable to the 870 μm maps, which show all material along the line of sight. B&W provided us with the data cubes of four regions, and indeed, the maps of CO emission integrated over the velocity are similar to the 870 μm maps. This is illustrated for the N49 region in Fig. 14. However, the dust condensations, which are dense and cold, are expected to be less apparent on the CO maps than on the 870 μm maps for several reasons: i) the CO (3−2) emission is insensitive to high densities; ii) the condensations are probably optically thick in ^{12}CO; and iii) the CO molecule is probably depleted in the gaseous phase because it condenses onto the dust grains in cold dense cores (Caselli et al. 1999; Bacmann et al. 2002).

The column densities that we estimate for the dust condensations associated with the bubbles using the 870 μm emission, are much higher than these estimated by B&W from their observations. If the column densities were of the order of those estimated by B&W, almost no emission would be detected by ATLASGAL. At the 870 μm rms noise of ~0.07 Jy/beam, the derived column density of $N(H_2) \sim 1.8 \times 10^{21}$ cm^{-2} is indeed higher than the values estimated by B&W for the HCO$^+$ emitting regions (see their Fig. 7). The column densities that we measure for dust condensations associated with massive young objects, for example the condensations containing class II methanol masers, are in the range 5×10^{22} to 1.3×10^{24} cm^{-2} (see Sect. 6.6). These values are compatible with the theoretical

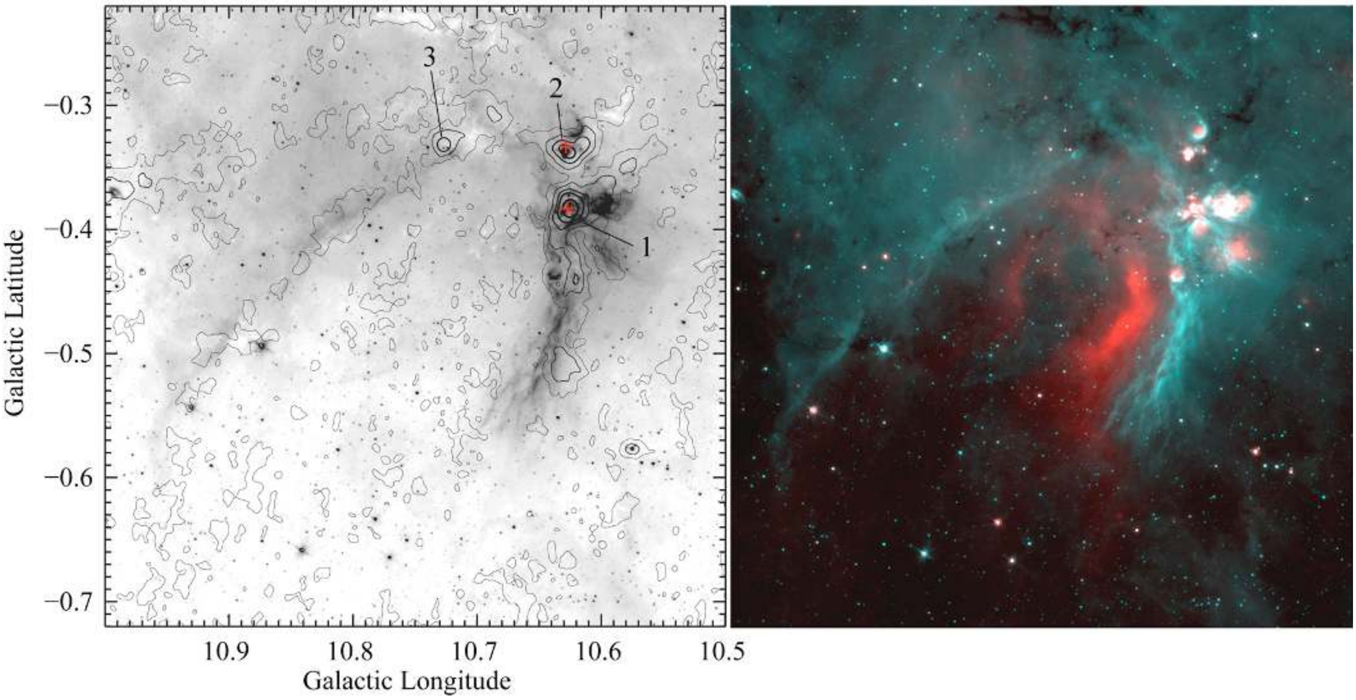

Fig. 15. N2: *left*: contours of the 870 μm emission superimposed on the *Spizer*-GLIMPSE 8.0 μm image. We see the faint emission from the cold dust associated with the collected neutral material, on the borders of N2; we also see bright condensations containing various young stellar objects and UC H II regions; (870 μm emission: σ = 0.06 Jy/beam; contour levels 1, 5, 20, 40, 150σ). The red crosses give the position of two methanol masers. *Right*: *Spitzer*-GLIMPSE 8.0 μm emission in turquoise and -MIPSGAL 24 μm emission in red.

predictions of Whitworth et al. (1994), who show that, for a wide range of input parameters, the gravitational fragmentation of a shocked layer occurs when the column density of this layer reaches a value $\sim 6 \times 10^{21}$ cm^{-2}. Furthermore, the mean densities that we estimate for the dust condensations are lower than these obtained by B&W, even for the shell surrounding the bubbles (their Fig. 7). These high densities obtained by B&W probably result from a strong underestimate of the CO column densities, possibly due to depletion or from the assumption of small optical depth used in the LVG formalism.

For example, for N65 and the associated dust condensation containing an UC H II region and a methanol maser (Fig. 21), we measure a peak intensity of 5.15 Jy/beam. This corresponds to a column density of $N(\mathrm{H_2}) = 1.33 \times 10^{23}$ cm^{-2}. The size at half intensity of this condensation is 0.3 pc (for D = 3.6 kpc, Table A.2) and its integrated flux density is 14.5 Jy, which imply a mass of 1065 $M_\odot$ and a mean density of 7×10^5 cm^{-3}. These numbers are very different from the values estimated by B&W for this region (respectively $\sim 10^{21}$ cm^{-2} and $\geq 10^7$ cm^{-3} for the column density and density in the HCO$^+$ region).

6.5. Massive-star formation triggered by the expanding bubbles

Sixteen bubbles display compact or UC H II regions (detected in radio-continuum and 24 μm emission) at their periphery, often in the direction of bright adjacent dust condensations. The column densities, visual extinctions, and masses given in this section are based on the formulae and assumptions given in Appendix B, and on the distances given in Table A.2. Detailed studies of the most interesting regions, in terms of triggered star formation, will be given in a forthcoming paper.

6.5.1. N2

This is a large bubble, elongated along the eastwest direction, that opens on its eastern side (see Fig. 15). It surrounds an extended H II region, which probably evolved in a medium presenting a density gradient as all the emission on the western side (at 8.0 μm, 24 μm, and 20-cm) are brighter than on the eastern side. The distance to this region is uncertain; it has been discussed by Corbel & Eikenberry (2004), who, on the basis of CO emission lines and NH$_3$ absorption features from associated molecular clouds, suggest a near distance of 4.5 ± 0.6 kpc. It has also been discussed by Pandian et al. (2008), who also favor a near distance of 3.4 kpc. The N2 bubble has a diameter of 30 pc (E-W) × 15 pc (N-S) (if D = 4.5 kpc). The 870 μm cold dust emission shows a shell of collected material surrounding the ionized region in the west (Fig. 15). Several bright condensations are present there. The velocity of the neutral material has been measured at several positions (see Table A.2) and velocities have been found in the range −1.5 km s^{-1} to −4.6 km s^{-1}. This is similar to the velocity of the central H II region, −2.4 km s^{-1}. Because of this velocity agreement, we conclude that the neutral material in the shell and the bright condensations are associated with the central H II region.

Several UC and compact H II regions are present in the direction of the two main condensations, or are adjacent to them. The peak emission for condensation #1 at 10.6234−00.3819 is 25.2 Jy/beam at 870 μm. This corresponds to a column density $N(\mathrm{H_2}) = 6.5 \times 10^{23}$ cm^{-2} (∼350 mag of visual extinction). The UC H II region G010.624−00.384 lies in the same direction. As discussed by Keto & Wood (2006), a cluster of massive stars that contains massive YSOs still in the accretion phase ionizes this very young H II region. A 6.7 GHz methanol maser is detected nearby (Menten 1991; Caswell 1995; see Sect. 6.6 and Table A.2). MAGPIS detects two additional compact H II regions

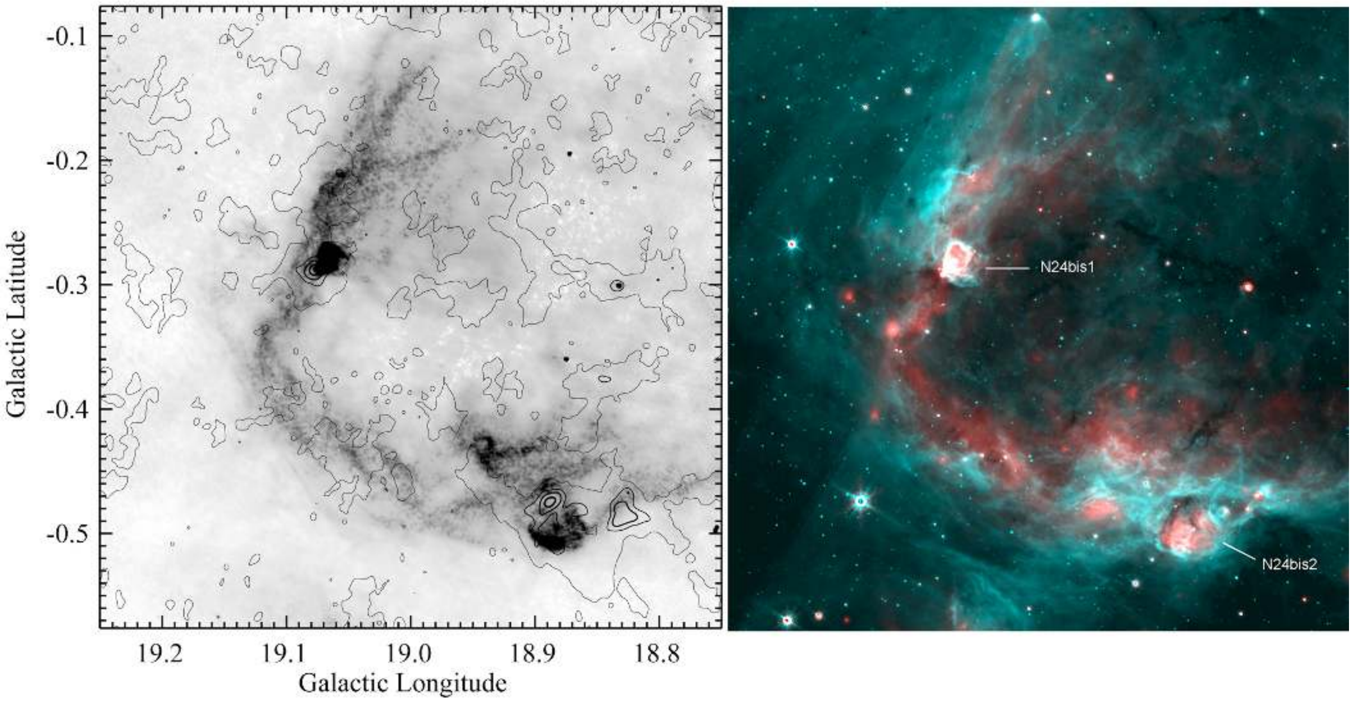

Fig. 16. N24: *left*: 870 μm contours superimposed on the MAGPIS radio-continuum image at 20-cm (*sigma* = 0.06 Jy/beam; contour levels 1, 10, 30, 60, 100σ). *Right*: colour composite image, with red for the *Spitzer*-MIPSGAL emission at 24 μm and turquoise for the *Spitzer*-GLIMPSE emission at 8.0 μm. The two second-generation compact H II regions, N24bis1 and N24bis2, are identified.

adjacent to this condensation, located at G010.598−00.384 and G010.621−00.386. Condensation #2 peaks at 10.6264−00.3357 with a peak emission at 870 μm of 2.4 Jy/beam. This corresponds to a column density of $N(H_2) = 6.2 \times 10^{22}$ cm^{-2} (~33 mag of visual extinction). MAGPIS detects an UC H II region in this direction, at G010.629−00.338, and a 6.7 GHz methanol maser is detected nearby (Caswell 1995; Sect. 6.6 and Table A.2). MAGPIS finds a compact H II region adjacent to this condensation, at G010.618−00.320. Another extended 24 μm source is surrounded by a 8.0 μm shell at G010.639−00.434. It lies in the direction of the collected shell. This is possibly another H II region.

6.5.2. N18

This is a faint, not very clearly defined open bubble with spiraling filaments at 8.0 μm. For a distance of 12.4 kpc, its diameter is ~50 pc (but the distance is uncertain, see Table A.2). Several very faint 870 μm cold dust condensations are located along the 8.0 μm filaments. Two compact radio sources are present at the western border of the bubble. They are not extragalactic sources because they have associated 24 μm emission. The brightest UC H II region lies at 16.6002−00.2759; at 5 GHz, its integrated flux is 12.2 mJy and its diameter is 3.″1 (Becker et al. 1994). Another fainter UC H II region lies nearby, at 16.589−00.283. No cold dust emission is detected in their direction. Their association with the N18 bubble is uncertain.

6.5.3. N24

This is a large (≥30 pc for a distance of 4.6 kpc; Table A.2), wide-open bubble. The 8.0 μm emission tracing the bubble is somewhat confusing, but the radio-continuum emission exhibits a well-defined H II region (Fig. 16). The radio and 24 μm emission follow, but are located interior to, the emission from filaments at 8.0 μm. Faint cold dust emission is observed in the direction of the 8.0 μm filaments, most likely tracing the collected neutral material. At least two compact H II regions, N24bis1 and N24bis2, lie on the borders of N24. Bright 870 μm emission is observed in their direction or vicinity. All these objects (the large bubble, the two compact H II regions, and the 870 μm condensations) are associated because their velocities are within 3 km s^{-1} of each other (see Table A.2). The 870 μm emission associated with N24bis2 forms a shell surrounding the compact central H II region. A class II methanol maser lies in the direction of this shell (Sect. 6.6 and Table A.2).

6.5.4. N35

This is a large bubble, not well-defined at 8 μm, that is possibly open to the southeast. At a distance of 8.6 kpc, its size is 23 pc × 11 pc. Several cold dust condensations are present, adjacent to the PDR. Two condensations are bordered by bright rims, and thus are clearly associated with the bubble. Furthermore, one of the brightest, at 24.4587+00.1968, has a velocity of 119.08 km s^{-1} similar to that of the central H II region (Table A.2), confirming the association. A bright radio source with a jet is present at 24.4539+00.2296 (Becker et al. 1994); it is most probably an extragalactic source as it has no counterpart at 8.0 μm or 24 μm. A compact H II region is present at 24.429+00.223, in the direction of an adjacent dust condensation. Furthermore, a very small 8.0 μm bubble (diameter 0.5 pc, if at the same distance) enclosing 24 μm emission lies in the direction of another condensation; we suggest that it may be another second-generation UC H II region. A 6.7 GHz methanol maser is observed in the direction of the PDR, associated with faint dust emission (Sect. 6.6 and Table A.2).

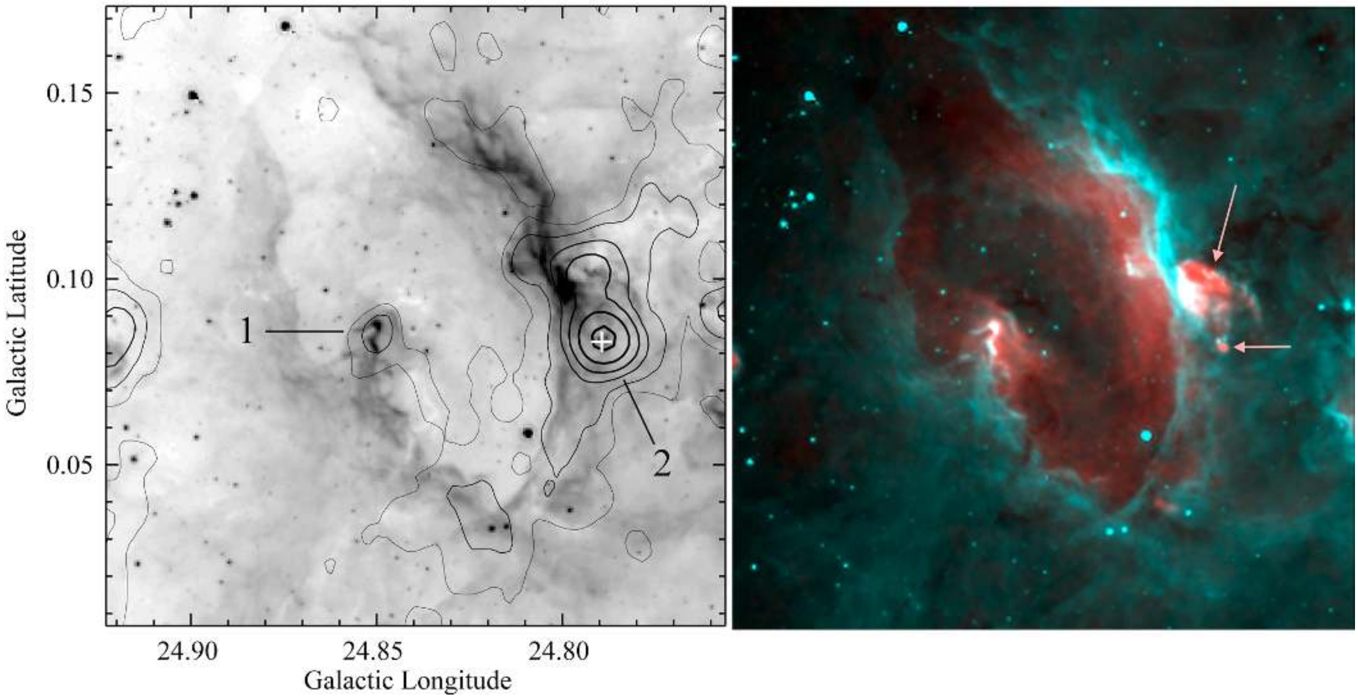

Fig. 17. N36: *left*: contours of the 870 μm emission superimposed on the 8.0 μm image (σ = 0.09 Jy/beam; contour levels 1, 3, 5, 10, 20, 60σ). The white cross shows the position of the methanol maser. *Right*: *Spitzer*-GLIMPSE 8.0 μm emission in turquoise and MAGPIS 20-cm emission in red. The arrows identify the compact and UC H II regions.

6.5.5. N36

This is an open bubble (Fig. 17), of size 15 pc × 7.5 pc for a distance of 6.4 kpc (Table A.2). It is elongated southeast – northwest, and open on the north west side. The 8.0 μm bubble surrounds a diffuse H II region G24.83+00.10 (Kantharia et al. 2007; also called G24.81+0.10 by Lockman 1989). Figure 17 shows faint 870 μm emission in the direction of the PDR, most likely from cold dust in the neutral collected shell. On the east side, a small condensation (#1) lies in the direction of a 8.0 μm bright rim. Examination of emission from MAGPIS indicates that this radio source at G24.849+00.088 likely arises from the dense ionized layer bordering this condensation, and is not a different H II region. A very bright condensation is situated on the opposite side (#2). High resolution radio observations (Kantharia et al. 2007, MAGPIS) show that it contains a compact cometary H II region (G24.796+00.098) and two UC ones in the direction 24.789+00.82; Furuya et al. (2002) discuss the presence of CO outflows and of various maser emission in this direction (among them a 6.7 GHz methanol maser, Sect. 6.6 and Table A.2). All these objects are probably associated as they present similar velocities (Table A.2).

6.5.6. N39

This is a bipolar nebula (Fig. 10 and Sect. 6.1). Several bright 870 μm condensations are observed at its periphery. The compact H II region G25.30−00.14 lies in the direction of one of them (in this direction, $N(\mathrm{H_2})$ = 1.10 × 10^{23} cm^{-2} or A_V ~ 59 mag). The velocity of G25.30−00.14 (98.4 km s^{-1}) differs consideraably from that of the central H II region G25.38−00.18 (57.1 km s^{-1}); thus they are not associated. A 6.7 GHz methanol maser lies at the waist of the bipolar nebula; both objects have similar velocities (see Sect. 6.6 and Table A.2).

6.5.7. N49

This is one of the most well-defined bubbles of the sample (Fig. 18). Its internal diameter is 4.0 pc (for a distance of 5.5 kpc, Table A.2). The central H II region has a radio-continuum flux density of 1.14 Jy at 2.695 GHz (Reich et al. 1984), 1.16 Jy at 4.875 GHz (Wink et al. 1982), and 1.38 Jy at 10.05 GHz (Handa et al. 1987). This radio emission corresponds to an ionizing photon flux of ~3 × 10^{48} s^{-1}. This flux corresponds to a main exciting star of spectral type O7V−O7.5V (Martins et al. 2005). MAGPIS shows that a compact H II region lies in the direction of the PDR. For this region, we measure a radio flux (20-cm) ≤ 0.1 Jy. This flux corresponds to a B0V exciting star, assuming that its radio emission is optically thin at 20-cm. This compact H II region is also surrounded by bright 8.0 μm emission. N49 has been studied in the mid-IR by Watson et al. (2008). Possible exciting stars for the central H II region have been identified; the main one lies in the direction of the radio and 24 μm central hole, and, based on its spectral energy distribution (SED), is either an O5V or O8III star (thus emitting more ionizing photons than necessary to account for the radio flux).

ATLASGAL shows that a shell of collected material surrounds the central H II region. This shell is brighter on its eastern and northern sides, probably because a density gradient was present in the parental cloud. The whole shell, defined by a 870 μm emission brighter than 0.08 Jy/beam (the rms noise in this field), has a total flux of 24.75 Jy, thus a mass of 4200 $M_\odot$ (Appendix B). The shell is fragmented. The most massive fragment has a peak flux of 4.4 Jy/beam (at 18:44:51.05−03:46:02 (J2000); condensation #1 in Fig. 18) corresponding to a column density 1.1 × 10^{23} cm^{-2} (or a visual extinction of 61 mag). Its flux density is 13.70 Jy, which corresponds to a mass of 2300 $M_\odot$. The other neutral condensations, numbered #2, #3, and #4, are less bright. They have peak intensities in the range 0.64−0.75 Jy/beam (and thus column densities in the range

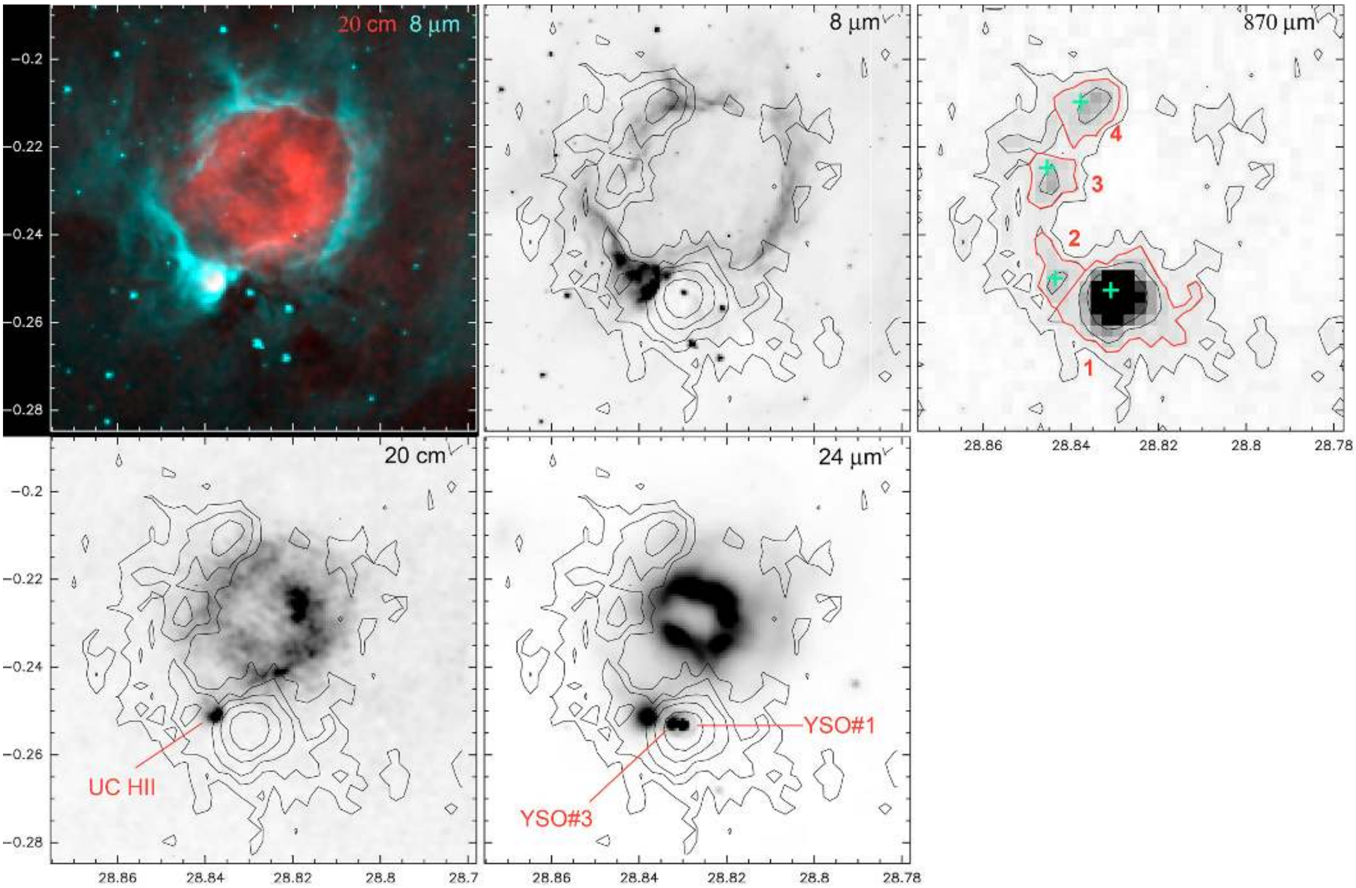

Fig. 18. N49. *Top left*: *Spitzer*-GLIMPSE 8.0 μm emission in turquoise and 24 μm emission in red. *Others*: contours of 870 μm emission superimposed to greyscale images at 8.0 μm, 870 μm, 20-cm, and 24 μm; the 870 μm contour levels are 0.08 Jy/beam (used to define the limits of the collected shell), 0.25, 0.5, 1.0, and 2.0 Jy/beam. The red contours at 0.25 Jy/beam have been used to measure the integrated 870 μm flux of condensations 1 to 4. The green crosses indicate the NH_3 positions measured by Wyrowski & Wienen (in preparation; Table A.2). The massive stage I YSOs found by Watson et al. (2008) are indicated.

1.65−1.9 × 10^{22} cm^{-2}), integrated flux densities of 1.14 Jy, 1.41 Jy, and 2.07 Jy, thus masses of 190 $M_{\odot}$, 240 $M_{\odot}$, and 350 $M_{\odot}$, respectively. The velocity of the four condensations (Table A.2) are similar (in the range 85.89−96.34 km s^{-1}) to the mean velocity of the ionized gas (90.6 km s^{-1}), confirming the association of the entire neutral shell with the H II region.

The compact H II region lies between condensations #1 and #2, adjacent to, but outside the most massive condensation. Two bright YSOs identified by Watson et al. (2008; their Fig. 16) lie in the direction of the center of condensation 1. According to their SEDs, both YSOs are massive (more than 10 $M_{\odot}$ for the central sources), and in an early evolutionary stage (stage I; the luminosity is dominated by the accreting envelope). Furthermore, YSO #3 in Watson et al. is associated with an extended 4.5 μm jet (extended green object or EGO; according to Cyganowski et al. 2008 extended 4.5 μm emission traces shocked molecular gas in protostellar outflows). Two 6.7 GHz methanol masers were detected by Caswell et al. (1995) in this region. The brightest one is observed in the direction of condensation #1, the other, much fainter, in the direction of condensation #3. Their velocities (Table A.2), which are similar to those of the associated condensations, indicate that they are associated with the shell surrounding the N49 H II region. Cyganowski et al. (2009) present high angular resolution methanol maser observations at 6.7 GHz and 44 GHz in the direction of YSO #3 (their Figs. 1 and 5). They show that the 6.7 GHz methanol emission is observed in the direction of the center of the 4.5 μm jet. This emission is linearly distributed along an axis extending over 3000 AU and has a velocity gradient that is indicative of a rotating disk.

6.5.8. N52

This bubble encloses a giant H II region and is part of the W43 complex. The distance of this region is uncertain; Anderson & Bania (2009) place it at the near distance, 5.7 kpc, whereas Pandian et al. (2008) favour the far distance, 9.0 kpc. In the following, we adopt, rather arbitrarily, the near distance. Numerous studies have been performed of the W43 complex. The flux density of the H II region at 5 GHz, 86.5 Jy (Smith et al. 1978) corresponds to a ionizing photons flux ~2.3 × 10^{50} s^{-1}; this points to an exciting cluster containing ~13 O5V stars or ~55 O7V stars (according to the calibration of Martins et al. 2005). The ionized gas was studied by Lester et al. (1985) and Balser et al. (2001, and references therein); the radio continuum map shows several filamentary components or sources; a detailed velocity field contains velocities ranging from 60 km s^{-1} to 110 km s^{-1}. The exciting cluster was analysed by Blum et al. (1999), using deep *JHK* images; this cluster is highly reddened (A_V in the range 0 to 45 mag), and contains at least a WN7 and two early (supergiant) O stars; these stars emit strong winds. The associated molecular material was studied by Motte et al. (2003, and references therein). The molecular cloud has a mass ~10^6 $M_{\odot}$. The cold dust emission (at 350 μm and 1.3-mm) and

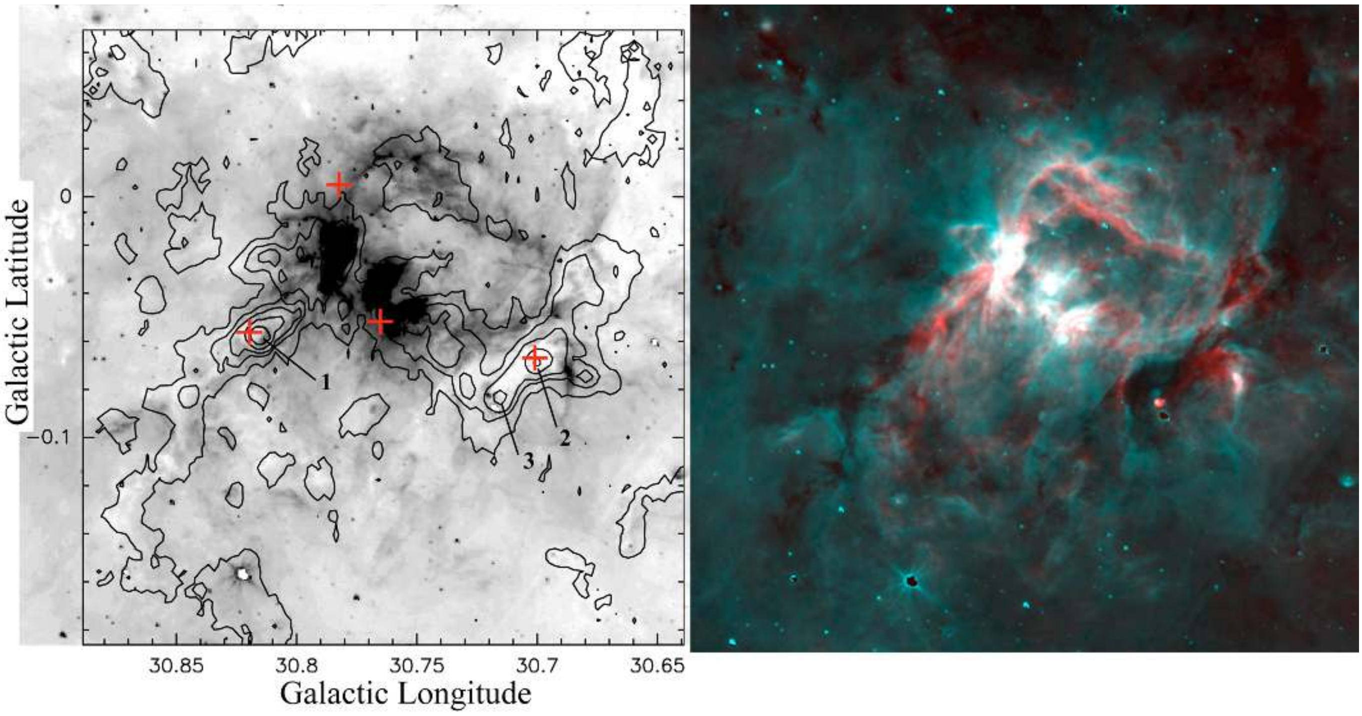

Fig. 19. N52: *left*: contours of the 870 μm emission superimposed on the *Spitzer*-GLIMPSE 8.0 μm image (the contour levels are 0.15 Jy/beam, 1, 2, 5, and 10 Jy/beam). The red crosses show the position of the methanol masers. The condensations #1, #2, #3 contain the cores W43-MM1, -MM2, -MM3 of Motte et al. (2003). *Right*: colour composite image, with the MAGPIS 20-cm emission in red and the 8.0 μm emission in turquoise. Note the bipolar and filamentary structure of this nebula.

the molecular HCO^+ emission have been mapped at high resolutions; they show a filamentary structure, with massive condensations (40−4000 $M_\odot$), large nonthermal velocities (~5 km s^{-1}), and high densities (~10^6 cm^{-3}). Stellar sources with a near-IR excess (Blum et al. 1999) and several maser sources (OH, H_2O, and methanol; see their location in Fig. 1 in Motte et al. 2003) indicate that star formation is still taking place in this complex. Several papers (especially Balser et al. 2001; Motte et al. 2003) suggest that the exciting cluster has a large impact on the surrounding material (both ionized and molecular), blowing it away from the center of the nebula, and compressing it to filaments.

Thus, N52 is not a bubble enclosing a classical, almost spherical H II region. Since the Motte et al. (2003) study, observations have shed new light on this complex. The *Spitzer*-8.0 μm and the MAGPIS-radio observations (the 24 μm emission is saturated over the field), both show, at high resolution and over a wide field, many filamentary structures linked to the complex. Both observations indicate a bipolar morphology (Fig. 19), with the exciting cluster at the center. Furthermore, the ionized gas is distributed in filaments following exactly, on the inside, the 8.0 μm filaments. We propose the following origin and evolution for this complex: i) a massive cluster formed in a massive and rather flat molecular cloud and it ionized an expanding H II region; ii) with time, the massive stars evolved and become Wolf-Rayet and supergiant stars, emitting very strong winds; iii) a very low density, very hot ionized component developed inside the H II region (according to the simulations of Freyer 2003); the expansion accelerated, and the classical H II region was reduced to a thin layer surrounding the central hot ionized gas; iv) presently, the ionized region extends in directions of lower density (perpendicular to the parental cloud), and neutral (collected) material is seen all around. More material is collected at the waist of the bipolar nebula, because this is where the density of the neutral gas is the highest.

This explanation of the bipolar structure agrees with the observed cold dust emission. This emission comes both from material at the waist of the bipolar nebula, and from filamentary structures elongated along the northeast and the southwest PDRs (Fig. 19). The 870 μm emission is very similar to the 350 μm and 1.3-mm emission observed by Motte et al. (2003). For the entire region, we measure a flux density at 870 μm of 408 Jy, indicating a mass of 7.5 × 10^4 $M_\odot$. At least three condensations are very bright and well defined (#1, #2, #3; Fig. 19); they contain the bright cores W43-MM1, -MM2, and -MM3 of Motte et al. (2003). We measure for these condensations 870 μm peak intensities of respectively 21.4 Jy/beam, 11.6 Jy/beam, and 6.3 Jy/beam, corresponding to column densities $N(H_2)$ of 11.4×10^{23} cm^{-2} ($A_V = 295$ mag), 6.2×10^{23} cm^{-2} ($A_V = 160$ mag), and 3.3×10^{23} cm^{-2} ($A_V = 87$ mag). The 870 μm flux densities integrated over regions limited by the 1 Jy/beam contour level (Fig. 19) are, respectively, 76.7 Jy, 59.3 Jy, and 25.3 Jy, for masses of 14 000 $M_\odot$, 4700 $M_\odot$, and 11 000 $M_\odot$ (the W43-MM1, -MM2, -MM3 cores have smaller sizes and masses). Methanol masers at 6.7 GHz are observed in the direction of W43-MM1 and W43-MM2. A third methanol maser is observed in the direction of W43-MM4 (situated at the waist of the bipolar nebula) for which we measured a peak signal of 4.4 Jy/beam ($N(H_2) = 2.3 \times 10^{23}$ cm^{-2}). A fourth maser is given by Xu et al. (2009) toward the PDR, but in a direction of very low 870 μm emission (see Table A.2).

6.5.9. G31.155 and N53

The bubble N53 encloses a relatively small H II region (diameter ~ 4.8 pc for a distance of 11.9 kpc; Table A.2).

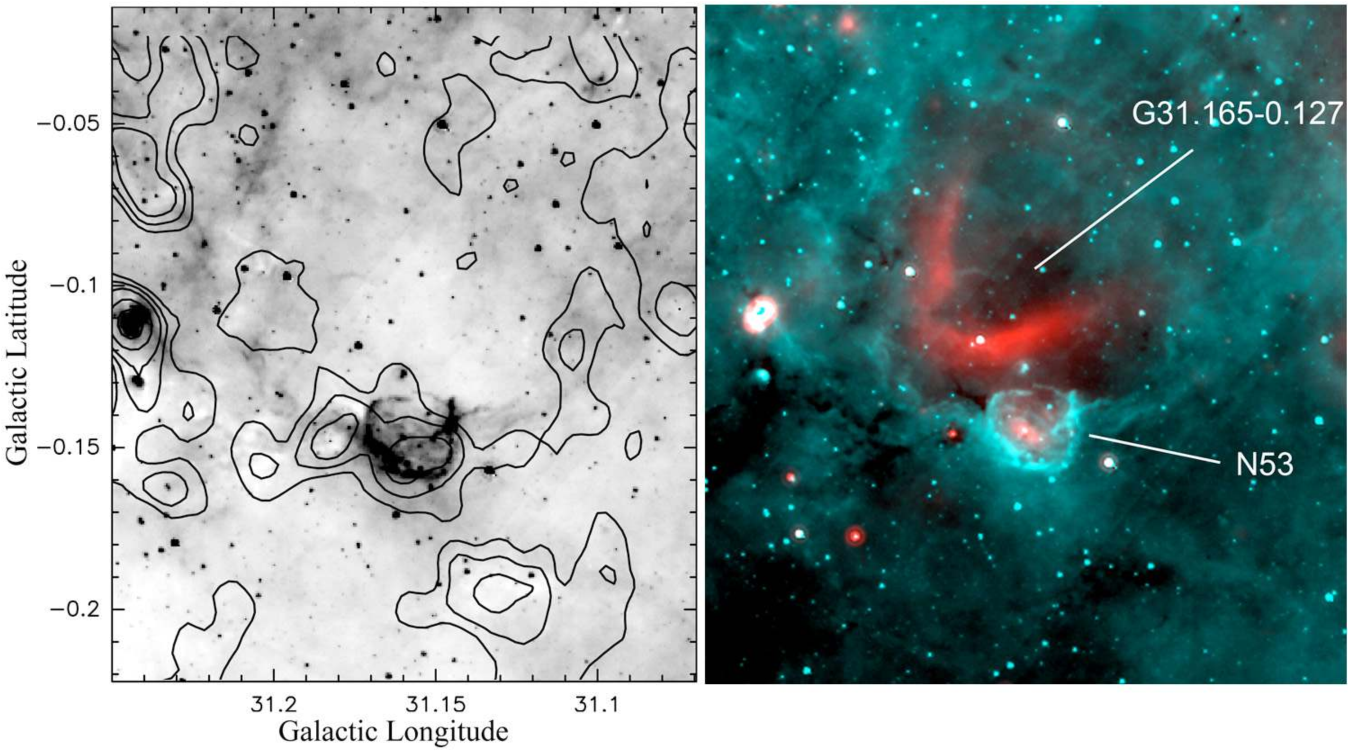

Fig. 20. G31.165-00.127 and N53: *left*: the 870 μm contours levels are superimposed on the 8 μm image; the levels are 0.03, 0.1, 0.2, 0.5 and 1.0 Jy/beam. There is a faint emission structure surrounding the bottom part of G31.165-00.12, with a condensation in the direction of N53. *Right*: composite colour image with the 24 μm emission in red and the 8.0 μm emission in turquoise.

Figure 20 shows that it lies on the border of a larger H II region, G31.165−00.127 (diameter ~ 20 pc for the same distance). The two H II regions are probably linked as they have similar velocities (43.6 and 41.4 km s^{-1}, Table A.2) and N53 is centered on the PDR surrounding G31.165−00.127. In addition N53 lies in the direction of a faint 870 μm emission structure following the PDR of G31.165−00.127. Thus, the exciting star of the H II region at the center of N53 is a good candidate to be a second-generation massive-star, the formation of which has been triggered by the expansion of G31.165−00.127.

6.5.10. N59

This is a rather faint bubble that is not well-defined. It is open to the south. If at 5.6 kpc (Table A.2), its diameter is ~20 pc. A bipolar nebula lies on its northern border, which is possibly associated with N59, but its velocity differs by some 10 km s^{-1} from that of N59. Several cold dust condensations are present adjacent to the PDR. The brightest one contains several radio sources; three of them are in the Becker et al. (1994) catalogue. The radio source at 33.1441−00.0665 (S(5 GHz) = 33.9 mJy, diameter = 4.8″) is most probably extragalactic as it has no 24 μm counterpart. An UC H II region at 33.1330−00.0926 (S(5 GHz) = 385.2 mJy, diameter = 3.″7) has an associated H_2O maser (Kurtz & Hofner 2005), and an associated 6.7 GHz methanol maser (Sect. 6.6 and Table A.2). A compact H II region lies at 33.1420−00.0863 (S(5 GHz) = 26.5 mJy, diameter = 13.″0). A faint UC H II region, which is not catalogued by Becker et al. (1994) lies at 33.111−00.095. The small nearby bubble N58 is possibly associated with N59, as they have very similar velocities (but see the discussion about their distances in Appendix A).

6.5.11. N65

This is a well-defined bubble of medium size (diameter ~ 5 pc for a distance of 3.6 kpc). It is possibly adjacent to another bubble that we have named N65bis. A shell of collected material surrounds N65 (Fig. 21). A bright dust condensation lies between N65 and N65bis. A very bright 24 μm source lies in its center, cospatial with an UC H II region detected via its radio continuum emission. The dust condensation has been observed at 1.2-mm and has a mass of 560 $M_\odot$ (Hill et al. 2005), for a distance of 3.6 kpc (Table A.2). The mass of its molecular counterpart was estimated from ^{13}CO (1−0) observations by Petriella et al. (2010) to be ~2000 $M_\odot$. From the 870 μm emission, we estimate the mass of this condensation to be 1060 $M_\odot$ (see Sect. 6.4 for more details). The UC H II region lies at 35.024+00.350; it has a flux density of 14 mJy at 3.6-cm, and a size (*HPBW*) of ~0.″9 (Kurtz et al. 2005). The OH, H_2O, and 6.7 GHz methanol maser emission are observed in a nearby direction (respectively, Argon et al. 2000; Kurtz & Hofner 2005; Pandian et al. 2007; see also Sect. 6.6).

A small 8.0 μm bubble around an extended 24 μm source is also present in the direction of the collected layer between N65 and N65bis, at 35.044+00.327. No radio emission is detected in its direction; it is possibly a faint compact H II region.

The N65 – N65bis complex may be similar to the Sh 255 – Sh 257 complex where several young massive objects have been found in the compressed zone between the two H II regions (Chavarria et al. 2008, and references therein).

6.5.12. N68

This is a large bubble, elongated northwest to southeast, and possibly open to the southeast. Its size is 34 pc × 17 pc for a distance of 10.6 kpc (Table A.2). It is very similar in appearance to N36. Faint 870 μm emission follows the 8.0 μm PDR,

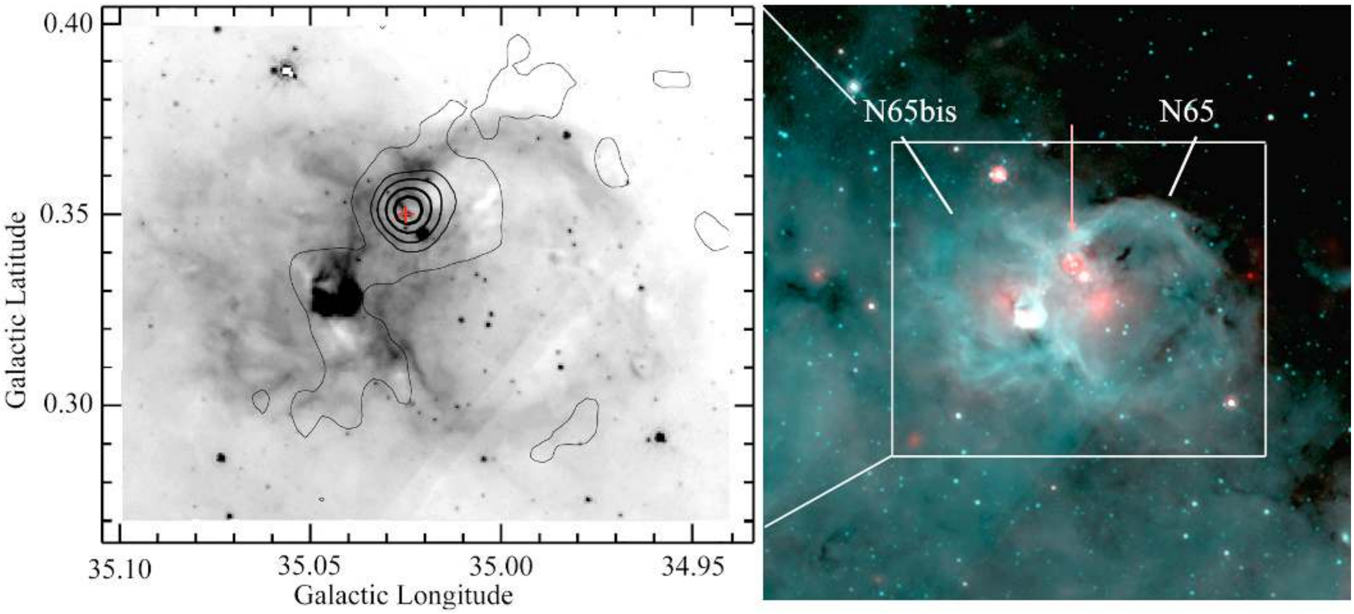

Fig. 21. N65 & N65bis. *Left*: contours of the 870 μm emission superimposed on the 8.0 μm image (σ = 0.04 Jy/beam; contour levels 1, 5, 15, 30, 50σ); *Right*: *Spitzer*-GLIMPSE 8 μm emission in turquoise and -MIPSGAL 24 μm emission in red. We see both the faint emission from the cold dust associated with the collected material surrounding N65, and a bright condensation between the two H II regions, suggesting a zone of compression. The bright condensation contains an UC H II region and a class II methanol maser. The arrow points to a bright 24 μm source which is also a UC H II region. The red cross gives the position of the methanol maser.

probably corresponding to cold dust emission in the collected neutral shell. One dust condensation corresponds to a bright rim observed at 8.0 μm, bordered by bright 20-cm emission. On the other side lies a bright 870 μm condensation. This condensation is associated with the central H II region, as it has a similar velocity ($V_{\rm LSR}$(CS) = 54.1 km s^{-1}, Plume 1992; $V_{\rm LSR}$(H110α) = 51.8 km s^{-1}, Araya et al. 2002). In the direction of this condensation lies a compact H II region, G35.590−00.025, and an UC H II region G35.578−00.031 (Kurtz et al. 1999). OH and H_2O maser emission are observed in the direction of the UC H II region (Forster & Caswell 1999).

6.5.13. N81

This is a very faint, large bubble. For a distance of 8.1 kpc (Table A.2), its size is 45 pc × 32 pc. Two smaller bubbles, N82 and N83 lie on its border. N82 (diameter 7.5 pc) is clearly associated with N81 on morphological basis (Fig. 22). The velocity of N83 differs from that of N82 by more than 10 km s^{-1}; thus, N83 is probably not associated with N81 and N82.

6.5.14. N91

This is a large bubble (28 pc × 14 pc for D = 8.1 kpc; Table A.2), open in the south, with a bright PDR on its east side (Fig. 23). A faint elongated 870 μm structure follows this part of the PDR. Two dust condensations are present in the direction of the PDR, probably slightly in the foreground as a faint absorption is observed at 8 μm in their directions. An UC H II region (which is also a bright 24 μm source) lies near the peak of the brightest condensation. Several other 24 μm sources and a 6.7 GHz methanol maser are also present there. We have no velocity for the UC H II region or for this dust condensation, but the methanol maser has a velocity similar to that of the central H II region, confirming the association (Table A.2).

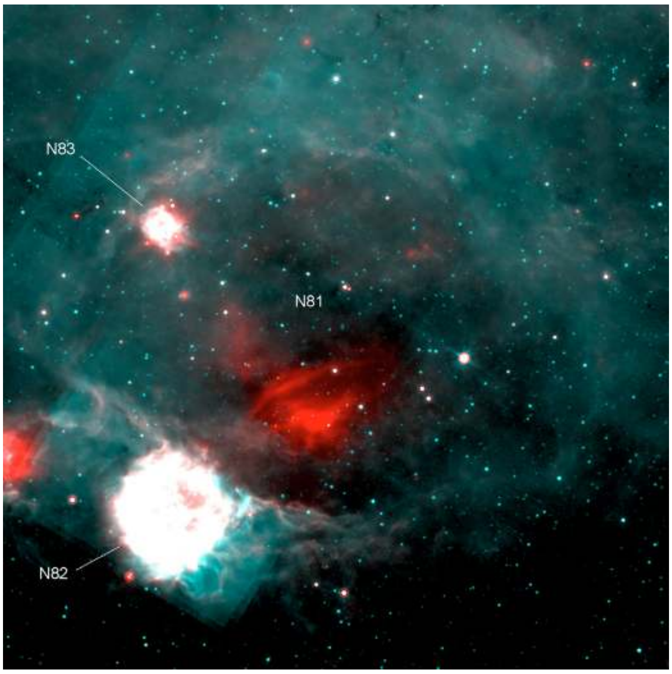

Fig. 22. N81 and the possible second generation H II region N82. Colour composite image: red represents the *Spitzer*-MIPSGAL emission at 24 μm and turquoise represents the *Spitzer*-GLIMPSE emission at 8.0 μm.

6.5.15. N94

This is an open bubble. At a distance of 9.3 kpc (Table A.2), its size is 20 pc × 12 pc. The nearby small bubble N93 (diameter 4.0 pc if at the same distance) lies in the direction of a filament, which is adjacent to N94. This association, however, is uncertain and a measurement of the velocity of N93 is required.

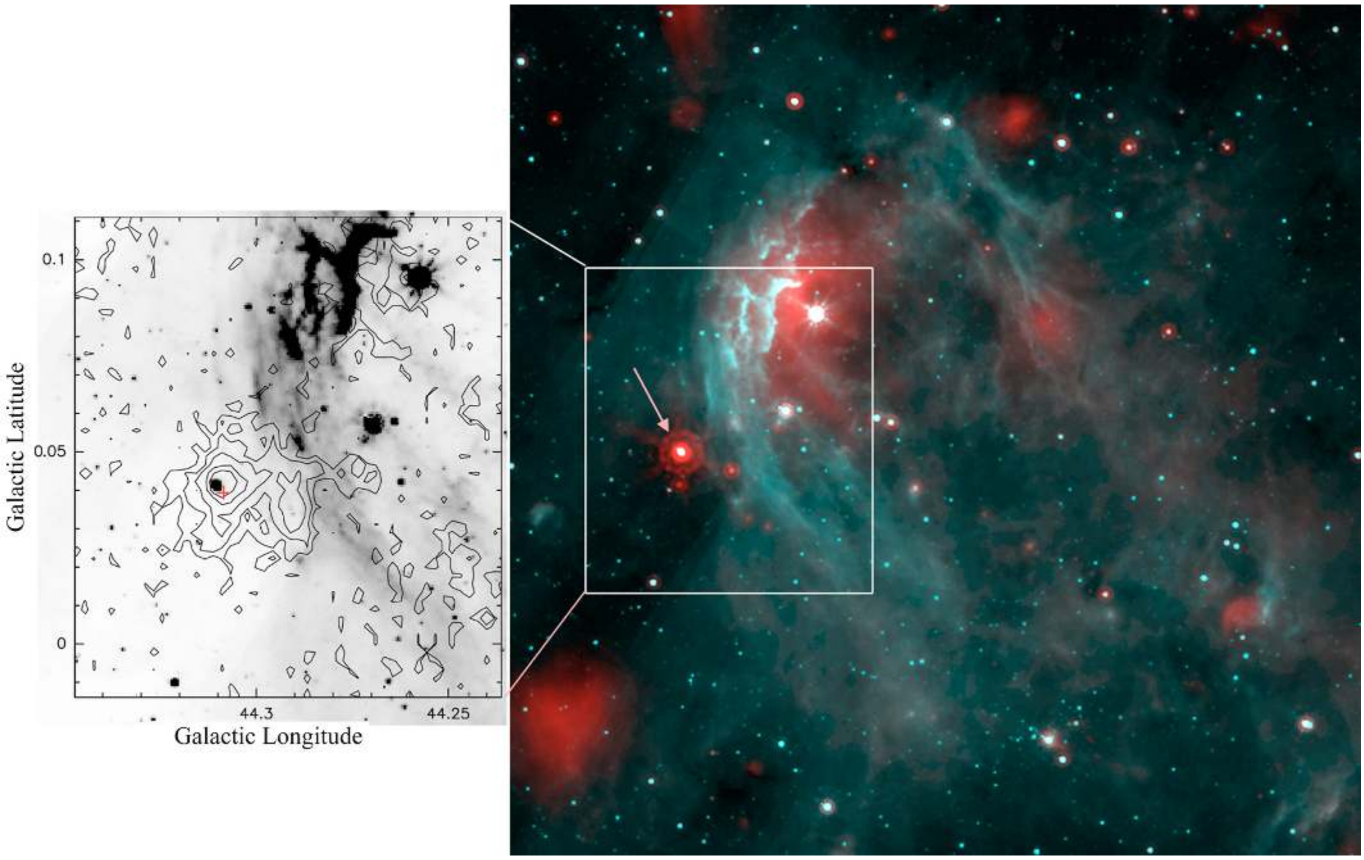

Fig. 23. N91. *Left*: the 870 μm contour levels (0.1, 0.25, 0.5, 1.0, 1.5 Jy/beam) are superimposed on the *Spitzer*-GLIMPSE 8 μm image. The red cross gives the position of the methanol maser. *Right*: colour composite image with the 24 μm emission in red and the 8 μm emission in turquoise. The arrow points to a bright 24 μm source, which is also a UC H II region.

6.5.16. N97

This is an angularly large (diameter ~ 16′) and faint bubble that is not well defined at 8 μm, except along its north border. The small N96 bubble (diameter ~ 1′) lies on this border and is clearly associated with a bright rim bordering a dust condensation. We have no velocities and no distances for these regions.

6.5.17. Conclusions

To conclude, 13 bubbles have associated UC H II regions in the direction of their PDRs and in neutral condensations adjacent to their IFs. These bubbles are N2, N24, N35, N36, N49, N52, G31.16, N59, N65, N68, N81, N91, and N97. These regions are good candidates for triggered massive-star formation. The N94 bubble is another possible candidate for this process, but the association between the large H II region and the UC H II region needs to be confirmed by velocity measurements. The case for N18 is more uncertain as the nearby UC H II regions are not observed in the direction of dust condensations.

Most of these bubble candidates for triggered massive-star formation are large bubbles (size ≥ 15 pc), which could indicate that they represent an evolved population. However, N49 and N65, perhaps our best cases of triggered massive-star formation, are exceptions. Their diameters are in the range 4–5 pc. A possible explanation is that they formed and evolved in a medium of higher density, which has restricted their expansion.

6.6. Other signposts of massive-star formation

The 6.7 GHz methanol masers (class II), discovered by Menten (1991), are associated with massive-star formation. Some are observed in the vicinity of UC H II regions (e.g. the W3(OH) source, Menten et al. 1992). Other methanol masers originate in the direction of (sub)-millimeter condensations containing luminous very red mid- or far-IR sources (*Spitzer*-GLIMPSE sources: Ellingsen 2006; 24 μm sources: Xu et al. 2009; and Minier et al. 2005, and references therein). Breen et al. (2010) present an evolutionary sequence for masers in high-mass star formation regions: 6.7 GHz masers have a lifetime in the range 2.5×10^4 yr to 4.5×10^4 yr; they are coeval with H_2O masers, and appear before the formation of a detectable UC H II region.

We searched for 6.7 GHz methanol masers in the vicinity of the bubbles, using the compilations by Pestalozzi et al. (2005) and Xu et al. (2009). Twenty-nine 6.7 GHz methanol masers have been detected in the vicinity of 23 bubbles. In the following, we comment briefly on the location of these masers with respect to nearby 870 μm condensations, UC H II regions, and mid-IR sources. The positions and velocities of the masers are given in Appendix A, Table A.2. The main difficulty when attempting to associate masers with other signposts of star formation is their positional accuracy, which varies widely from one study to another. The most accurate positions come from interferometric observations.

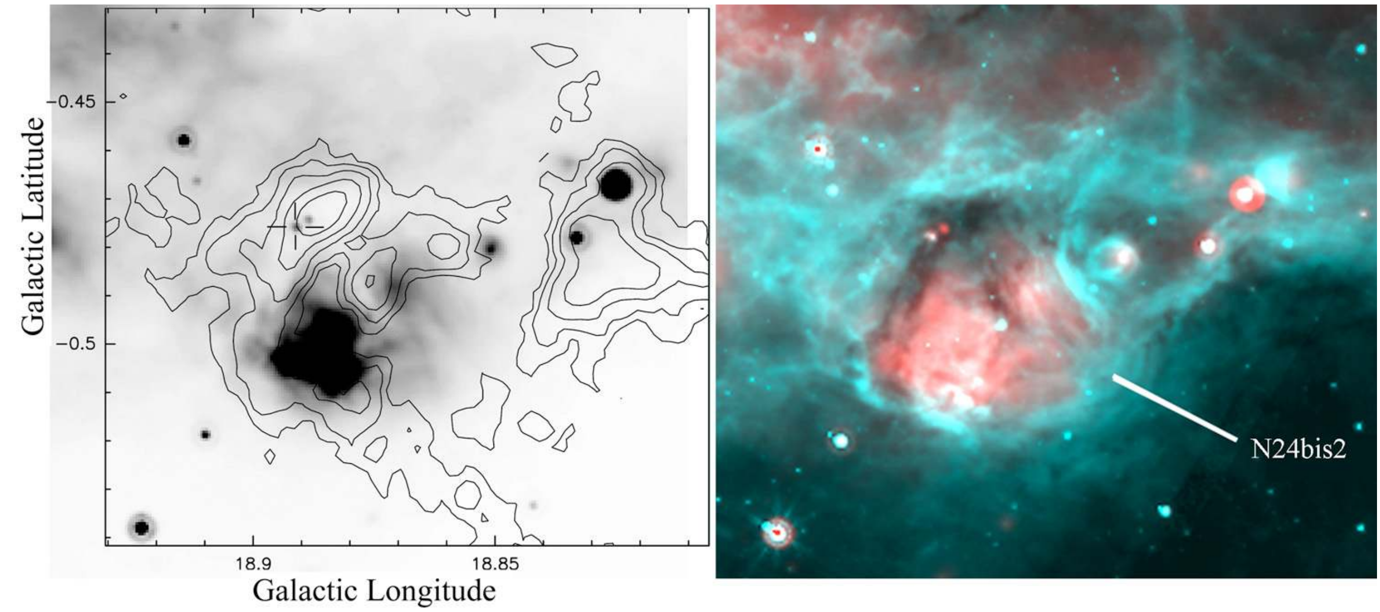

Fig. 24. N24bis2. *Left*: the 870 μm contour levels (0.1, 0.25, 0.5, 1.0, and 2.0 Jy/beam) are superimposed on the 24 μm image. The 6.7 GHz methanol maser, observed in the direction of an EGO, is at the center of the cross. *Right*: composite colour image with the 24 μm emission in red and the 8 μm emission in turquoise.

Walsh et al. (1998) used the Australia Telescope Compact Array (ATCA), which gives absolute positions with an uncertainty ∼1″. These masers lie near:

– N2: two bright 870 μm condensations lie at one extremity of this large open bubble (Fig. 15, Sect. 6.5); both contain a maser. The first maser lies ∼10″ away from the center of condensation #1 (peak emission 25.2 Jy/beam). This condensation contains several UC H II regions, which are also 24 μm sources; the maser lies ∼9″ away from the closest 24 μm source. The second maser lies ∼11″ away from the center of condensation #2 (peak emission 2.4 Jy/beam), and ∼17″ away from the associated UC H II region.

– N36: a maser lies in the direction of the bright adjacent 870 μm condensation (peak emission 15.8 Jy/beam, see Fig. 17), ∼6″ from the sub-mm peak. This is also the direction of a cluster of four YSOs (Furuya et al. 2002). As discussed by these authors, the methanol maser spots correspond to an UC H II region that is also associated with a CO outflow.

– N49: a maser lies in the direction of the bright 870 μm condensation #1 (peak emission 4.4 Jy/beam, Fig. 18 and Sect. 6.5), ∼12″ from its center. This condensation contains two bright mid-IR sources. The maser lies in the direction of one of them, which is also an extended green object (EGO, Cyganowski et al. 2009) with jets. A nearby UC H II region lies outside the condensation, within ∼20″ of the maser's position. A second fainter maser was detected by Caswell et al. (1995; positional accuracy ∼10″), at the border of condensation #3 (peak emission 0.73 Jy/beam); it has no radio or mid-IR counterpart.

– N52 (W43): a maser lies in the direction of the brightest 870 μm condensation (#1, peak emission 23.2 Jy/beam), ∼12″ from its center, and ∼6″ from two faint 24 μm sources. This condensation is adjacent to the bright PDR of W43 (Sect. 6.5 and Fig. 19). A second maser also lies in the direction of the PDR, but at the waist of the bipolar nebula, ∼24″ from a 870 μm condensation (emission peak 4.7 Jy/beam). In this direction, the 24 μm emission is saturated. A third maser lies ∼4″ away from the center of another bright 870 μm condensation (#2, emission peak 12.6 Jy/beam), and in the direction of the PDR of a compact associated H II region; it has no 24 μm counterpart.

Two more regions were observed at high resolution with the VLA by Cyganowsky et al. (2009). They are:

– N24bis2: the maser lies in the direction of a 870 μm condensation, part of the dust shell surrounding the central compact H II region (peak emission 3.7 Jy/beam; Fig. 24). Two mid-IR sources lie nearby. The maser is observed in the direction of one of them, which is also an EGO (Cyganowski et al. 2009). No radio-continuum source is detected nearby.

– N65: the maser is observed in the direction of the center of a 870 μm condensation (emission peak 5.15 Jy/beam) located between the two bubbles N65 and N65bis (Fig. 21 and Sect. 6.5). An UC H II region, which is also a bright 24 μm and 70 μm source, also lies at the center of this condensation. It was found by Kurtz et al. (1994) to be composed of two unresolved (*FWHM* of the beam $\sim 0\farcs9$) radio-continuum sources separated by 2″. The high resolution observations of Cyganowsky et al. (2009) show that the maser is observed in the direction of an EGO with jets, possibly centered on one of the radio sources. As discussed by Cyganowsky et al. (2009), the nature of this radio source is uncertain; it may be a hypercompact H II region or a dust core.

The masers reported by Caswell et al. (1995) were observed with the Parkes 64-m telescope. Their positions have errors of smaller than 10″ in each coordinate. They are:

–N59: a maser lies in the direction of the brightest 870 μm condensation (peak emission 4.0 Jy/beam), ∼17″ away from its center. This condensation contains an UC H II region in its very center, which is also a bright 24 μm source. A second maser is associated with a secondary fainter 870 μm condensation (peak emission 0.50 Jy/beam), which is surrounded by a bright rim at 8.0 μm; the maser lies ∼14″ away from the condensation's center and ∼8″ away from a 24 μm source situated at the tip of the bright rim.

– N61: a very bright 870 μm condensation (peak emission 51.4 Jy/beam) is adjacent to this faint bubble. It contains a group of UC H II regions (G34.3+0.2 A, B, C; Campbell et al. 2004)

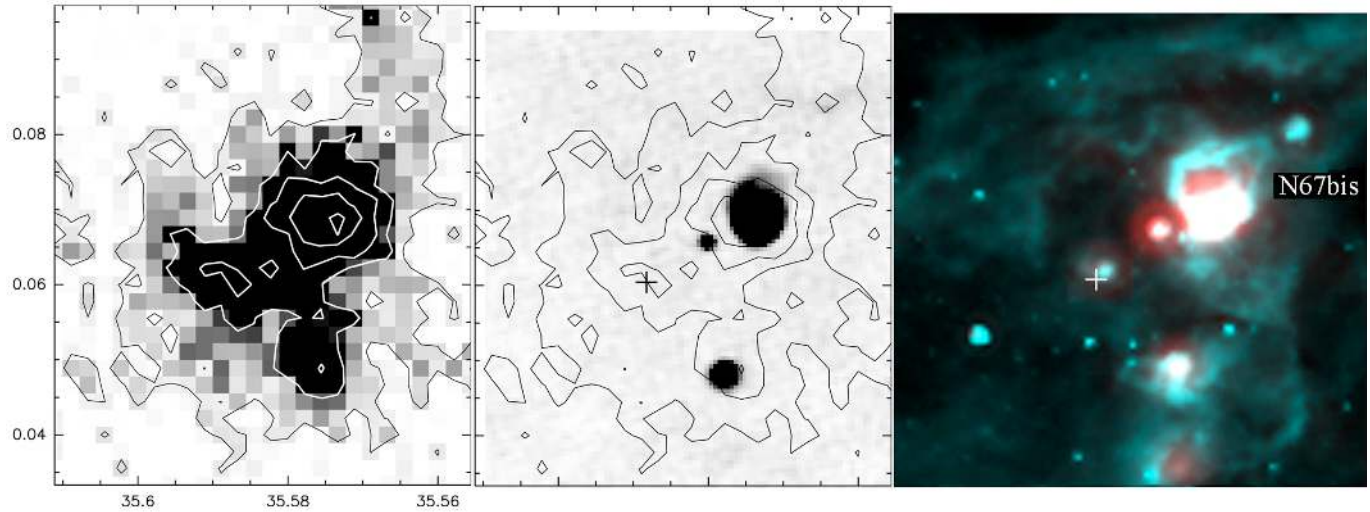

Fig. 25. N67bis, a region of active massive-star formation. *Left*: 870 μm emission; the contour levels are 0.1, 0.5, 1.0, 1.5, and 2.0 Jy/beam. *Middle*: the 870 μm contour levels are superimposed on the MAGPIS 20-cm image. *Right*: colour composite image with the 24 μm emission in red and the 8 μm emission in turquoise. The cross gives the position of the 6.7 GHz methanol maser (Pandian et al. 2007).

and two more classical (extended) H II regions. The maser lies ~9″ from the condensation's peak, on the border of the group of UC H II regions. (The UC H II regions lie near the center of the 870 μm condensation.) The 24 μm emission is saturated. This condensation is a very active massive-star formation region.

Six more masers associated with N67bis, N70, N71, N75, N79, and N91 were detected by Pandian et al. (2007). This unbiased survey, carried out using the Arecibo radio telescope, is complete at the level of 0.27 Jy over the region $l = 35.2°$ to $53.7°$, $|b| \leq 0.41°$. The Arecibo beam was 40″ (*FWHM*) and the pointing accuracy was 7″.

– The bubble N67bis is observed in the direction of a bright 870 μm condensation (peak intensity 2.1 Jy/beam) that is composed of three substructures. The whole condensation contains three radio sources (maximum separation ~80″, ~4 pc for a distance of 10.6 kpc, Table A.2). The methanol maser is observed in the direction of one of the secondary peaks; it is not associated with an UC H II region, but lies ~5″ away from a 24 μm source (Fig. 25). This region is an active massive-star formation, with three UC H II regions and a class II methanol maser inside a massive cloud of about 15 000 $M_\odot$ (the 870 μm emission, integrated over a region enclosed by the 0.1 Jy/beam level, gives a flux density of 23.5 Jy when we assume a distance of 10.6 kpc, Table A.2).

– N70: an 870 μm condensation is adjacent to N70 (emission peak 2.55 Jy/beam). An UC H II region lies at the condensation's center. The maser lies ~17″ from the condensation, in the direction of a faint 24 μm and 70 μm source.

– N71: two methanol masers are detected on the border of the large and faint N71 bubble. They have very different velocities, and thus cannot both be associated with N71. The velocity of the H II region enclosed by N71 is unknown. We suggest that maser #1 is associated with the bubble as it is observed in the direction of a 870 μm condensation possibly linked to structures of the ionization front. The 870 μm peak emission is 1.6 Jy/beam. The condensation does not contain an UC H II region, but only a 24 μm source at the very center of the condensation. The maser lies 17″ away from the center.

– N75 is adjacent to a 870 μm condensation (peak emission 2.8 Jy/beam) that contains a compact H II region and bright 24 μm sources. A methanol maser lies on the border of the condensation, ~26″ away from its center, on the border of the compact H II region. The maser lies ~10″ away from the closest 24 μm source.

– N79: this is a region of very faint 870 μm emission. The methanol maser lies in the direction of the PDR; it is not associated with a 870 μm condensation, or an UC H II region, and lies ~8″ away from a faint 24 μm source.

– N91: a bright 870 μm condensation containing an UC H II region and a methanol maser lies adjacent to the PDR of N91 (maximum emission 2.6 Jy/beam; Fig. 23). The methanol maser lies ~17″ away from the center of the condensation, and ~13″ away from the UC H II region.

Three masers associated with N35, N58, and N69 were observed by Szymczak et al. (2002), using the Torun 32-m telescope. According to the authors, the positional accuracy is better than 30″.

– N35: a maser lies in the direction of a faint filament (870 μm emission 0.24 Jy/beam), adjacent to the PDR. There is no nearby UC H II region or 24 μm source.

– N58: this small bubble lies near the center of a 870 μm condensation (peak emission 2.4 Jy/beam). The maser is on the border of this condensation, ~34″ away from its center, outside the ionized region. No 24 μm source is present nearby.

– N69: the maser lies on the border of an 870 μm condensation (peak emission 1.2 Jy/beam), situated on the open side of N69. The condensation contains no UC H II region, but does have a bright 24 μm source. The maser lies ~30″ away from the center of the condensation; it has no 24 μm counterpart.

Two more masers were detected by Xu et al. (2008) associated with N32 and N39. They have been observed with the Effelsberg 100 m-telescope. According to Xu et al. (2008), the masers' positions may have an error as high as 1′.

– N32: the maser is situated on the border of N32. No 24 μm source is observed nearby. There is an 870 μm condensation (peak emission 1.6 Jy/beam) adjacent to N32, containing an UC H II region. The maser lies ~50″ away from the condensation's peak emission and ~38″ away from the UC H II region's center.

– N39: a maser lies on the border of an 870 μm condensation located at the waist of the bipolar nebula (peak emission 3.0 Jy/beam). The maser lies ~23″ away from the condensation's

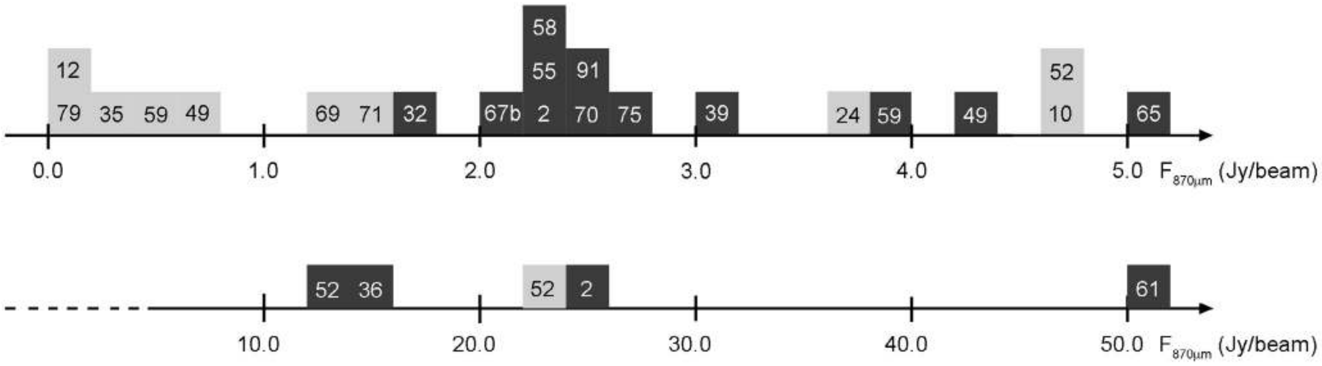

Fig. 26. Methanol masers: 870 μm flux density at the peak of the condensations in the directions of which 6.7 GHz methanol masers are detected. The nearby bubbles are identified by their number (e.g. "12" for N12). The black condensations also contain one or several UC H II regions; no UC H II regions have been detected in the direction of the light grey condensations. Note that the scale along the two axes differ by a factor ten.

peak, in a region of high radio emission and saturated 24 μm emission.

Four more masers were observed in the direction of IRAS sources that heve characteristics similsr to UC H II regions, by Szymczak et al. (2000) and Slysh et al. (1999). Because of the relatively poor positional accuracy of IRAS, the positions of these masers are rather uncertain. They are:

– N10: a maser is observed on the border of one of the two bright 870 μm condensations adjacent to the bubble. It lies ~31″ away from the peak emission (signal 4.7 Jy/beam). No UC H II region and no 24 μm sources are observed nearby (the nearest 24 μm source lies ~18″ away from the maser).

– N12: a maser lies not far from the PDR, but inside the bubble, in a region where no 870 μm emission is detected, and far from any 24 μm source.

– N22: the maser is not linked to the bubble, as it has a very different velocity (see Table A.2).

– N55: a maser lies inside the adjacent 870 μm condensation (peak emission 2.3 Jy/beam), ~9″ from the condensation's center. This condensation is an active massive-star formation region as it contains two UC H II regions and several bright 24 μm sources. The maser lies between the two UC H II regions, within 10″ of the closest one.

These class II methanol masers are most often observed in the direction of 870 μm condensations. Figure 26 gives the 870 μm flux density at the peak of these condensations. The condensations in the directions of UC H II regions (detected by MAGPIS) appear in black. Condensations without any UC radio sources appear in light grey. Figure 26 shows that most of the condensations containing UC H II regions and class II methanol masers have high column densities, in the range 5×10^{22} to 1.3×10^{24} cm^{-2}. These column densities are higher by a factor ~10 than the column densities estimated in the direction of the shells of collected material. (The 870 μm flux densities in the collected shells, outside the condensations, are in the range 0.1–0.5 Jy/beam indicating column densities in the range 2.6×10^{21}–1.3×10^{22} cm^{-2}.)

Many of the bright 870 μm condensations containing a class II methanol maser are very active massive-star forming regions. They often contain several young massive objects in different evolutionary stages: various masers, and UC and compact H II regions. The condensation associated with N67bis is a good illustration of such a region (Fig. 25). Similar condensations are found near N2, N36, N55, N59, and N61.

A few class II methanol masers are found in quite different regions, associated with a bright rim (N59, N71), in a region of high compression between two bubbles (N65). Some are even seen in directions of dim 870 μm emission such as those associated with N12, N35, and N79 (their positions, however, are possibly not very accurate).

The presence of 6.7 GHz methanol masers in dust condensations adjacent to the bubbles is a strong indicator of massive-star formation presently at work. As discussed by Breen et al. (2010), 6.7 GHz methanol masers appear before the formation of a detectable UC H II region, and are still present at the beginning of their evolution; their lifetime is short, $\leq 5 \times 10^4$ yr. Thus, they are much younger than the classical H II regions enclosed by the bubbles (with ages of a few Myr).

At least 12 bubbles show class II methanol masers in the direction of condensations interacting with the enclosed H II regions. They are good candidates for triggered massive-star formation. They are N2, N10, N24bis2, N36, N39, N49, N52, N59, N65, N69, N71, and N91.

6.7. Infrared dark clouds (IRDCs)

IRDCs were discovered by the ISO and MSX surveys as structures seen in absorption against the bright Galactic mid-IR background (Perault et al. 1996; Carey et al. 1998). IRDCs may contain dense, cold, and massive cores which are often presented as the locations where clusters and high-mass stars form (Chambers et al. 2009, and references therein; Peretto & Fuller 2009).

Several of the possible second-generation UC H II regions described above are seen in the direction of bright molecular condensations, with high column densities at the peak. This is the case for the UC H II region G24.789+00.082 on the border of N36. The column density in this direction is $N(\mathrm{H_2}) = 4.13 \times 10^{23}$ cm^{-2} (corresponding to a visual extinction $A_V \sim 221$ mag). However, as shown in Fig. 27, this condensation does not appear to be an IRDC at 8.0 μm (or 24 μm) because it lies in the direction of the bright PDR of N36, and slightly at the back of the H II region. The foreground PDR emission hides any absorption. An IRDC is observed nearby (also detected in emission at 870 μm) that corresponds to the outer part of the condensation, far from the PDR. The same situation is observed for the condensation on the opposite side of N36.

The situation is the same for the bright condensations at the border of N2 ($N(\mathrm{H_2}) = 6.51 \times 10^{23}$ cm^{-2}), at the border of N59

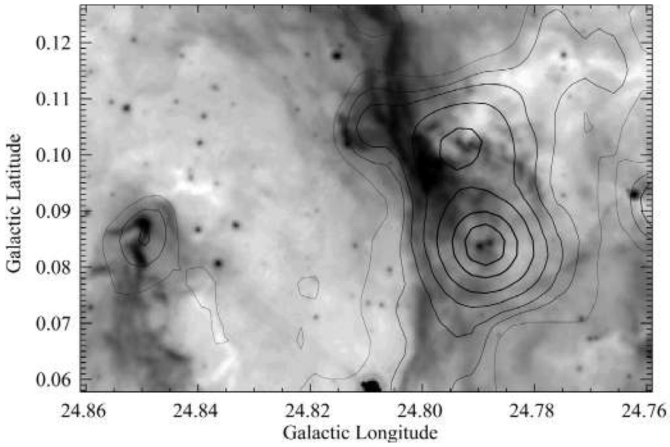

Fig. 27. Dense condensations and IRDCs at the border of N36. The 870 μm contour levels are superimposed on the 8 μm image (σ = 0.09 Jy/beam; contour levels are 1, 3, 5, 10, 20, 40, and 60σ). The dense condensation in the direction of the possible second-generation UC H II region G24.789+00.082 does not appear as an IRDC. It lies in the direction of the bright PDR surrounding N36, and probably slightly behind it. The foreground bright 8.0 μm emission of the PDR hides the background absorption caused by the condensation.

($N(H_2) = 1.02 \times 10^{23}$ cm^{-2}), at the border of N65 ($N(H_2)$ = 1.33×10^{23} cm^{-2}), or at the border of N68 ($N(H_2) = 1.07 \times 10^{23}$ cm^{-2}). All these bright dust condensations do not appear as IRDCs.

This situation was already observed in the RCW 120 bubble (Deharveng et al. 2009; their Fig. 3) where the brightest condensation adjacent to the ionization front (condensation 1, with a peak column density of 4.2×10^{23} cm^{-2}) is not observed as an IRDC, whereas the outskirts of this condensation, far from the IF, are observed in absorption at 8.0 μm.

To conclude, not all massive condensations (where high-mass star formation may occur) appear as IRDCs. Many massive condensations, adjacent to H II regions, and slightly behind the ionized gas are not seen in absorption at 8.0 μm or 24 μm; this absorption is hidden by the emission of the PDR at these wavelengths.

7. Conclusions

We have studied 102 regions identified as "bubbles" on the *Spitzer*-GLIMPSE images at 8.0 μm. Most of these regions were catalogued by Churchwell et al. (2006). This large sample allows us to draw the following statistical conclusions:

- At least 86% of the bubbles enclose H II regions, detected in the MAGPIS and VGPS surveys at 20-cm as radio-continuum sources. Therefore, bubbles are clearly associated with H II regions and their massive OB2 exciting stars.
- Ninety-eight percent of the bubbles enclose hot dust radiating at 24 μm. This emission is more centrally peaked than the radio-continuum emission of the ionized gas. Therefore, dust grains are present inside the ionized region, where they are heated by the absorption of Lyman continuum photons emitted by the central exciting stars. However, this study alone cannot say wether this hot dust emission comes from big grains in thermal equilibrium or from very small grains out of equilibrium.
- The cold dust emission at 870 μm, as traced by ATLASGAL, allows us to detect the dense (and often massive) condensations that are potential sites of star formation. In 65 regions, we have high enough angular resolution to study the distribution of neutral material and dust in the vicinity of the bubbles. Forty percent of these 65 regions are surrounded by collected material forming a (partial) shell or a "necklace" of condensations around the ionized gas. Another 28% show interacting condensations, bordered by bright rims. These are possibly pre-existing condensations that are being compressed by the adjacent expanding H II regions. The association is uncertain for 24% of the bubbles as we lack velocity information, and 8% of the bubbles present no detectable cold dust emission.
- At least 13 bubbles (possibly 14) have been found to contain an UC H II region (or several of them) in the direction of their PDRs. These additional H II regions are located in dense condensations adjacent to the IFs. At least 12 bubbles show class II methanol masers in dense adjacent condensations (7 bubbles with associated UC H II regions and methanol masers, plus 5 more bubbles with only methanol masers). These regions are good candidates for triggered massive-star formation. Thus, among the 65 H II regions enclosed by bubbles, and for which the angular resolution of ATLASGAL is high enough to study the distribution of cold dust, more than a quarter may have triggered the formation of massive-stars. This indicates that massive-star formation triggered by H II regions may be a rather efficient process to form massive stars (either via collect and collapse or by radiative compression of pre-existing clumps). A detailed study of several of these regions will be given in a forthcoming paper.

The very simple morphology of these regions also allows us to draw some morphological conclusions:

- We confirm that PAHs are destroyed in the ionized gas. PAHs are strong emitters at 8.0 μm in the PDRs surrounding the H II regions for two reasons: i) they are excited by the far UV radiation leaking from the ionized regions; ii) there is a strong overdensity of neutral material just beyond the IF (by a factor 10 to 100, Hosokawa & Inutsuka 2005, 2006a).
- Hot dust is present inside the ionized zones. In many bubbles, more than half of the 24 μm continuum emission comes from dust inside the H II region. Models of H II regions must take into account the absorption of Lyman continuum photons there.

Acknowledgements. We thank D. Russeil for useful discussions about distance determinations, C. Beaumont and J. Williams for allowing us to use their CO observations, and J. Arthur for providing beautiful images of simulated H II regions. We thank Paola Caselli, our referee, for suggesting a number of clarifications. We thank the APEX staff for their help during the observations with APEX-LABOCA. This research has made use of the SIMBAD data base, operated at CDS, Strasbourg, France, and of the interactive sky atlas Aladin (Bonnarel et al. 2000). This work is based in part on observations made with the *Spitzer Space Telescope*, which is operated by the Jet Propulsion Laboratory, California Institute of Technology, under contract with NASA. We have made use of the NASA/IPAC Infrared Science Archive to obtain data products from the 2MASS, *Spitzer*-GLIMPSE, and *Spitzer*-MIPSGAL surveys. We have used images extracted from the MAGPIS survey. These images were generated with data from telescopes of the National Radio Astronomy Observatory, a National Science Foundation Facility, managed by Associated Universities Inc. The research presented in this paper has also used data from the Canadian Galactic Plane Survey, a Canadian project with international partners supported by the Natural Sciences and Engineering Research Council. L.A. acknowledges support by the ANR Agence Nationale pour la recherche project "PROBeS", number ANR-08-BLAN-0241. L.B. acknowledge support from the Center of Excellence in Astrophysics and Associated Technologies (PFB06) and by FONDAP Center for Astrophysics 15010003.

References

Allain, T., Leach, S., & Sedlmayr, E. 1996a, A&A, 305, 602
Allain, T., Leach, S., & Sedlmayr, E. 1996b, A&A, 305, 616
Anderson, L. D., & Bania, T. M. 2009, ApJ, 690, 706
Araya, E., Hofner, P., Churchwell, E., & Kurtz. S. 2002, ApJS, 138, 63
Argon, A. L., Reid, M. J., & Menten, K. M. 2000, ApJS, 129, 159
Arthur, S. J. 2009, The Local Bubble and Beyond, AIP Conf. Proc., 1156, 285
Arthur, S. J. 2010, Computational Star Formation, IAU Symp., 270, submitted
Bacmann, A., Lefloch, B., Cessarelli, C., et al. 2002, A&A, 389, L6
Balser, D. S., Goss, W. M., & De Pree, C. G. 2001, AJ, 121, 371

Barlow, M. J., & Silk, J. 1977, ApJ, 215, 800
Beaumont, C. N., & Williams, J. P. 2010, ApJ, 709, 791
Beck, S. C., Kelly, D. M., & Lacy, J. H. 1998, AJ, 115, 2504
Becker, R. H., White, R. L., Helfand, D. J., & Zoonematkermani, S. 1994, ApJS, 91, 347
Benjamin, R. A., Churchwell, E., Babler, B. L., et al. 2003, PASP, 115, 953
Blum, R. D., Damineli, A., & Conti, P. S. 1999, AJ, 117, 1392
Blum, R. D., Damineli, A., & Conti, P. S. 2001, AJ, 121, 3149
Bohlin, R. C., Savage, B. D., & Drake, J. F. 1978, ApJ, 224, 132
Bodenheimer, P., Tenorio-Tagle, G., & Yorke, H. W. 1979, ApJ, 233, 85
Bisbas, T. G., Wünsch, R., Whitworth, A. P., & Hubber, D. A. 2009, A&A, 497, 649
Bonnarel, F., Fernique, P., Bienayme, O., et al. 2000, A&ASS, 143, 33
Brand, J., & Blitz, L. 1993, A&A, 275, 67
Breen, S. L., Ellingsen, S. P., Caswell, J. L., & Lewis, B. E. 2010, MNRAS, 401, 2219
Campbell, M. F., Harvey, P. M., Lester, D. F., & Clark, D. M. 2004, ApJ, 600, 254
Capriotti, E., & Kozminski, J. F. 2001, PASP, 113, 677
Carey, S. J., Clark, F. O., Egan, M. P., et al. 1998, ApJ, 508, 721
Carey, S. J., Noriega-Crespo, A., Mizuno, D. R., et al. 2009, PASP, 121, 76
Caselli, P., Walmsley, C. M., Tafalla, M., Dore, L., & Myers, P. C. 1999, ApJ, 523, L165
Caswell, J. L., Vaile, R. A., Ellingsen, S. P., Whiteoak, J. B., & Norris, R. P. 1995, MNRAS, 272, 96
Césarsky, D., Lequeux, J., Abergel, A., et al. 1996, A&A, 315, L309
Césarsky, D., Jones, A. P., Lequeux, J., & Verstraete, L. 2000, A&A, 358, 708
Chambers, E. T., Jackson, J. M., Rathborne, J. M., & Simon, R. 2009, ApJS, 181, 360
Chavarria, L. A., Allen, L. E., Hora, J. L., Brunt, C. M., & Fazio, G. G. 2008, ApJ, 682, 445
Churchwell, E., Povich, M. S., Allen, D., et al. 2006, ApJ, 649, 759 (CH06)
Churchwell, E., Watson, D. F., Povich, M. G., et al. 2007, ApJ, 670, 428 (CH07)
Compiègne, M., Abergel, A., Verstraete, L., & Habart, E. 2008, A&A, 491, 797
Corbel, S., & Eikenberry, S. S. 2004, A&A, 419, 191
Cyganowski, C. J., Whitney, B. A., Holden, E., et al. 2008, AJ, 136, 2391
Cyganowski, C. J., Brogan, C. L., Hunter, T. R., & Churchwell, E. 2009, ApJ, 702, 1615
Deharveng, L., Zavagno, A., Schuller, F., et al. 2009, A&A, 496, 117
Desert, F.-X., Boulanger, F., & Puget, J. L. 1990, A&A, 237, 215
Downes, D., Wilson, T. L., Bieging, J., & Wink, J. 1980, A&ASS, 40, 379
Draine, B. T., & Li, A. 2007, ApJ, 657, 810
Dyson, J. E., & Williams, D. A. 1997, The physics of the interstellar medium, 2nd edn., ed. R. J. Tayler, & M. Elvis (Bristol and Philadelphia: Institute of Physics Publishing)
Ellingsen, S. P. 2006, ApJ, 638, 241
Elmegreen, B. G., & Lada, C. J. 1977, ApJ, 214, 725
Elmegreen, B. G., Kimura, T., & Tosa, M. 1995, ApJ, 451, 675
Falgarone, E., & Phillips, T. G. 1996, ApJ, 472, 191
Fazio, G. G., Hora, J. L., Allen, L. E., et al. 2004, ApJS, 154, 10
Forster, J. R., & Caswell, J. L. 1999, A&ASS, 137, 43
Franco, J., Tenorio-Tagle, G., & Bodenheimer, P. 1990, ApJ, 349, 126
Freyer, T., Hensler, G., & Yorke, H. W. 2003, ApJ, 594, 888
Freyer, T., Hensler, G., & Yorke, H. W. 2006, ApJ, 638, 262
Furuya, R. S., Cesaroni, R., Codella, C., et al. 2002, A&A, 390, L1
Fukuda, N., & Hanawa, T. 2000, ApJ, 533, 911
Giard, M., Bernard, J. P., Lacombe, F., Normand, P., & Rouan, D. 1994, A&A, 291, 239
Gritschneder, M., Naab, T., Walch, S., Burkert, A., & Heitsch, F. 2009, ApJ, 694, L26
Güdel, M., Brigg, K. R., Montmerle, T., et al. 2008, Science, 319, 309
Handa, T., Yoshiaki, S., Naomasa, N., Hisashi, H., & Makoto, I. 1987, PASJ, 39, 709
Helfand, D. J., Becker, R. H., White, R. L., Fallon, A., & Tuttle, S. 2006, AJ, 131, 2525
Henney, W. J., Arthur, S. J., Mellema, G., & Vazquez-Semadeni, E. 2010, in preparation
Hildebrand, R. H. 1983 Q.Jl. R. astr. Soc., 24, 267
Hill, T., Burton, M. G., Minier, V., et al. 2005, MNRAS, 363, 405
Hosokawa, T., & Inutsuka, S. 2005, ApJ, 623, 917
Hosokawa, T., & Inutsuka, S. 2006a, ApJ, 646, 240
Hosokawa, T., & Inutsuka, S. 2006b, ApJ, 648, L131
Icke, V. 1979, ApJ, 234, 615
Jackson, J. M., Rathborne, J. M., Shah, R. Y., et al. 2006, ApJS, 163, 145
Kantharia, N. G., Goss, W. M., Roshi, D. A., Mohan, N. R., & Viallefond, F. 2007, J. Astrophys. Astr., 28, 41
Kassim, N. E., Weiler, K. W., Erickson, W. C., & Wilson, T. L. 1989, ApJ, 338, 152
Keto, E., & Wood, K. 2006, ApJ, 637, 850
Kolpak, M. A., Jackson, J. M., Bania, T. M., Clemens, D. P., & Dickey, J. M. 2003, ApJ, 582, 756
Krumholz, M. R., & Matzner, C. D. 2009, ApJ, 703, 1352
Krumholz, M. R., Stone, J. M., & Gardiner, T. A. 2007, ApJ, 671, 518
Kuchar, T. A., & Bania, T. M. 1994, ApJ, 436, 117
Kurtz, S., & Hofner, P. 2005, AJ, 130, 711
Kurtz, S., Churchwell, E., & Wood, D. O. S. 1994, ApJS, 91, 659
Kurtz, S., Watson, A. M., Hofner, P., & Otte, B. 1999, ApJ, 514, 232
Leach, S. 1989, IAUS, 135, 155
Lebouteiller, V., Brandl, B., Bernard-Salas, J., Devost, D., & Houck, J. R. 2007, ApJ, 665, 390
Leger, A., & Puget, J. L. 1984, A&A, 137, 5
Lester, D. F., Dinerstein, H. L., Werner, M. W., et al. 1985, ApJ, 296, 565
Lockman, F. J. 1989, ApJS, 71, 469
Martins, F., Schaerer, D., & Hillier, D. J. 2005, A&A, 436, 1049
Martins, F., Pomarès, M., Deharveng, L., Zavagno, A., & Bouret, J.-C. 2009, A&A, accepted
Mellema, G., Arthur, S. J., Henney, W. J., Iliev, I. T., & Shapiro, P. R. 2006, ApJ, 647, 397
Menten, K. M. 1991, ApJ, 380, L75
Menten, K. M., Reid, M. J., Pratap, P., Moran, J. M., & Wilson, T. L. 1992, ApJ, 401
Micelotta, E. R., Jones, A. P., & Tielens, A. G. G. M. 2010, A&A, 510, 37
Minier, V., Burton, M. G., Hill, T., et al. 2005, A&A, 429, 945
Motte, F., Schilke, P., & Lis, D. C. 2003, ApJ, 582, 277
Normand, P., Rouan, D., Lacombe, F., & Tiphène, D. 1995, A&A, 297, 311
Omont, A. 1986, A&A, 164, 159
Paladini, R., Burigana, C., Davies, R. D., et al. 2003, A&A, 397, 213
Pandian, J. D., Goldsmith, P. F., & Deshpande, A. A. 2007, ApJ, 656, 255
Pandian, J. D., Momjian, E., & Goldsmith, P. F. 2008, A&A, 486, 191
Peeters, E., Martin-Hernandez, N. L., Damour, F., et al. 2002, A&A, 381, 571
Pérault, M., Omont, A., Simon, G., et al. 1996, A&A, 315, L165
Peretto, N., & Fuller, G. A. 2009, A&A, 505, 405
Pestalozzi, M. R., Minier, V., & Booth, R. S. 2005, A&A, 432, 737
Petriella, A., Paron, S., & Giacani, E. 2010, A&A, 513, A44
Plume, R., Jaffe, D. T., & Evans II, N. J. 1992, ApJS, 78, 505
Povich, M. S., Stone, J. M., Churchwell, E., et al. 2007, ApJ, 660, 346
Rathborne, J. M., Jackson, J. M., Chambers, E. T., et al. 2005, ApJ, 630, L181
Reich, W., Furst, E., Steffen, P., Reif, K., & Haslam, C. G. T. 1984, A&ASS, 58, 197
Rieke, G. H., Young, E. T., Engelbracht, C. W., et al. 2004, ApJS, 154, 25
Robitaille, T. P., Meade, M. R., Babler, B. L., et al. 2008, AJ, 136, 2413
Roelfsema, P. R., Cox, P., Kessler, M. F., & Baluteau, J.-P. 1998, ASP Conf. Ser., 132, 76
Schaller, G., Schaerer, D., Meynet, G., & Maeder, A. 1992, A&AS, 96, 269
Schuller, F., Menten, K. M., Contreras, Y., et al. 2009, A&A, 504, 415
Sellgren, K. 1984, ApJ, 277, 623
Sewilo, M., Watson, C., Araya, E., et al. 2004, ApJS, 154, 553
Sharpless, S. 1959, ApJS, 4, 257
Siringo, G., Kreysa, E., Kovács, A., et al. 2009, A&A, 497, 945
Slysh, V. I., Val'tts, I. E., Kalenskii, S. V., et al. 1999, A&ASS, 134, 115
Smith, L. F., Biermann, P., & Mezger, P. G. 1978, A&A, 66, 65
Stil, J. M., Taylor, A. R., Dickey, J. M., et al. 2006, AJ, 132, 1158
Szymczak, M., Hrynek, G., & Kus, A. J. 2000, A&ASS, 143, 269
Szymczak, M., Kus, A. J., Hrynek, G., Kepa, A., & Pazderski, E. 2002, A&A, 392, 277
Tenorio-Tagle, G. 1979, A&A, 71, 59
Tielens, A. G. G. M. 2008, Annu. Rev. Astro. Astrophys., 46, 289
Townsley, L. K., Feigelson, E. D., Montmerle, T., et al. 2003, ApJ, 593, 874
Walsh, A. J., Burton, M. G., Hyland, A. R., & Robinson, G. 1998, MNRAS, 301, 640
Watson, C., Povich, M. S., Churchwell, E. B., et al. 2008, ApJ, 681, 1341
Watson, C., Corn, T., Churchwell, E. B., et al. 2009, ApJ, 694, 546
Wink, J. E., Altenhoff, W. J., & Mezger, P. G. 1982, A&A, 108, 227
Whitworth, A. P., Bhattal, A. S., Chapman, S. J., Disney, M. J., & Turner, J. A. 1994, MNRAS, 268, 291
Xu, Y., Li, J. J., Hachisuka, K., et al. 2008, A&A, 485, 729
Xu, Y., Voronkov, M. A., Pandian, J. D., et al. 2009, A&A, 507, 1117
Zavagno, A., Deharveng, L., Comerón, F., et al. 2006, A&A, 446, 171

Pages 30 to 35 are available in the electronic edition of the journal at http://www.aanda.org

Appendix A: The distance to the bubbles

The distances to the H II regions in the center of the bubbles (or associated with them, see the footnotes) are given in Table A.2. These distances are kinematic distances (based on the velocity of the ionized gas measured mostly using radio recombination lines, and assuming circular rotation around the Galactic center). All the regions belong to the first quadrant. Therefore, each positive velocity has two possible distance solutions. This is known as the kinematic distance ambiguity (KDA).

Seventy-four H II regions have a measured velocity and fifty-seven of them have the KDA resolved. Most of the distances given in Table A.2 are from Anderson & Bania (2009), who resolved the KDA using two methods, one comparing the velocity of the ionized gas with the maximum velocity of H I absorption (H I emission/absorption), and one looking for H I absorption at the velocity of molecular emission (H I self-absorption). We also used distances from Sewilo et al. (2004), who resolved the distance ambiguity by comparing the velocity of the ionized gas with that of the H_2CO absorbing material along the same line of sight. Additional velocity measurements are from the Green Bank Telescope H II Region Discovery Survey (Anderson et al. 2010a, in prep.). For these new measurements, the distance was derived using the H I emission/absorption method (Anderson et al. 2010b, in prep). When the KDA was not resolved, we indicate in Table A.2 the two possible kinematic distances obtained using the Galactic rotation curve of Brand & Blitz (1993). In a few cases, two velocity components have been measured; they are both given in Table A.2.

Class II methanol masers (emitters at 6.7 GHz) are considered as signposts of recent massive-star formation. Twenty-nine methanol masers have been detected in the vicinity of the bubbles studied in this paper. Their coordinates and velocities are also given in Table A.2. We also report in this table the distances estimated by Pandian et al. (2008) for these masers. The KDA is resolved by comparing the maser velocity with the maximum velocity of the H I absorption in the same direction.

The velocities of several bright 870 μm condensations have been measured by F. Wyrowsky and M. Wienen, using the NH_3 (1, 1) inversion line (Wienen et al., in preparation). This information allows to confirm the association of the dust condensations with the nearby bubbles and H II regions. These velocities are also given in Table A.2.

The distances to two bubbles are especially problematic. The bipolar bubble N52 (W43) has a recombination line velocity of 91.6 km s^{-1} (Lockman 1989), which is near the tangent point velocity in this direction (105 km s^{-1} according to Brand & Blitz 1993). Differentiating between the near and the far kinematic distances using H I absorption, as A&B have done, relies on the detection of H I absorption between the recombination line velocity and the tangent point velocity. If these two velocities cannot be clearly separated, this method gives less reliable results than when they can. A&B also used the H I self-absorption method, this analysis favoring the near distance for N52, in agreement with Downes et al. (1980) and Kuchar & Bania (1994).

The H II region enclosed by N59 has a recombination line velocity of 87.4 km s^{-1} (Araya et al. 2002), which is near the tangent point velocity of 97.9 km s^{-1} according to the Brand & Blitz (1993) rotation curve. There is, however, H I absorption from the H II region's continuum beyond the tangent point velocity, which favors the far distance. A&B assigned the near distance based on H I self-absorption alone since the H I absorption method is less reliable for sources with velocities near the tangent point velocity than distinct from it. Pandian et al. (2008) favor the far distance based on H I absorption analysis. It seems likely, given the strong absorption at more than 10 km s^{-1} from the recombination line velocity, that N59 is at the far distance.

Appendix B: Column density and mass estimated from the 870 μm dust emission

In the following, we assume that the 870 μm emission arises from thermal dust grains. According to Hildebrand (1983), the total (gas+dust) mass of a condensation is related to its flux density S_ν by

$$M_{\rm (gas+dust)} = 100\,\frac{S_{870\,\mu\rm m}\;D^2}{\kappa_{870\,\mu\rm m}\;B_{870\,\mu\rm m}(T_{\rm dust})},$$

where D is the distance of the source, $\kappa_{870\,\mu\rm m}$ is the dust opacity per unit mass at 870 μm, and $B_{870\,\mu\rm m}(T_{\rm dust})$ is the Planck function for a temperature $T_{\rm dust}$. For all the estimates in this paper, we assumed a gas-to-dust ratio of 100, a dust temperature of 20 K, and an opacity $\kappa_{870\,\mu\rm m} = 1.8$ cm^2 g^{-1}. All these values are uncertain and the subject of discussion.

With the same assumptions, we can estimate the H_2 column density, $N(H_2)$, from the surface brightness $F_{870\,\mu\rm m}$, using the formula

$$N({\rm H_2}) = \frac{100\;F_{870\,\mu\rm m}}{\kappa_{870\,\mu\rm m}\;B_{870\,\mu\rm m}(T_{\rm dust})\;2.8\,m_{\rm H}\;\Omega_{\rm beam}},$$

where $F_{870\,\mu\rm m}$ is expressed in Jy beam^{-1}, $B_{870\,\mu\rm m}$ in Jy, $N(H_2)$ is per square centimetre, the hydrogen atom mass m_H is in grams, and the beam solid angle $\Omega_{\rm beam}$ is in steradians.

Adopting $\Omega_{\rm beam} = 9.817 \times 10^{-9}$ sr corresponding to a beam of 19.″2 (*FWHM*), and assuming $T_{\rm dust} = 20$ K, this gives

$$N({\rm H_2}) = 2.581 \times 10^{22}\;F_{870\,\mu\rm m}.$$

From the classical relations, $N({\rm H}+{\rm H_2})/E(B-V) = 5.8 \times 10^{21}$ particles cm^{-2} mag^{-1} (Bohlin et al. 1978) and $A_{\rm V} = 3.1\;E(B-V)$, we obtain $A_{\rm V} = 5.34 \times 10^{-22}\;N({\rm H_2}) = 13.78\;F_{870\,\mu\rm m}$.

Table A.1. Nature of the bubbles.

Name	l (°)	b (°)	Size (′)	Radio emission	24 μm emission	Nature
N1[2]	10.231	−0.305	10	Yes	Yes	H II region
N2	10.747	−0.468	30	Yes	Yes	H II region, open bubble
N3	11.570	+0.395	10	No	Yes	?
N4	11.892	+0.748	10	Yes	Yes	H II region
N6[3]	12.512	−0.609	25	?	Yes (faint)	?, two sources?
N7	12.787	−0.167	5	No	No	?
N8	12.805	−0.312	5	Yes	Yes	H II region
N8bis	12.795	−0.326	idem	No	Yes	?
N9	12.890	−0.046	5	No	Yes	?
N10[1]	13.188	+0.039	15	Yes	Yes (saturated)	H II region
N11	13.218	+0.082	idem	Yes	Yes	H II region
N12	13.727	−0.015	20	Yes	Yes	H II region
N13	13.900	−0.014	5	Yes	Yes	H II region
N14[1]	14.002	−0.135	10	Yes	Yes (saturated)	H II region = Sh 44
N15[1]	15.010	−0.611	10	No	? (faint)	?
N16[1]	15.017	+0.056	10	Yes	Yes	H II region, open bubble
G15.68	15.680	−0.280	30	Yes	Yes	H II region
N18	16.679	−0.366	20	Yes	Yes	H II region
N20[1]	17.917	−0.687	10	Yes	Yes	H II region
N21[1,4]	18.190	−0.396	10	Yes	Yes	H II region
N22[1]	18.254	−0.305	10	Yes	Yes (saturated)	H II region
N23	18.679	−0.237	5	Yes	Yes	H II region
N24[5]	19.000	−0.326	30	Yes	Yes	H II region, open bubble
N24bis1	19.066	−0.278	idem	Yes	Yes (saturated)	UC H II region
N24bis2	18.885	−0.492	idem	Yes	Yes	H II region
N25	19.507	−0.191	5	Yes	Yes	H II region
N25bis	19.494	−0.206	idem	Yes	Yes	UC H II region
N26	19.587	−0.051	5	Yes	Yes	H II region
G19.82	19.821	−0.322	5	?	Yes	?
N27[1]	19.814	+0.017	10	Yes	Yes	H II region
N28	21.351	−0.137	10	Yes	Yes	H II region
N29[1]	23.055	+0.559	25	Yes	Yes	H II region
N31	23.843	+0.097	10	Yes	Yes	H II region
N32	23.905	+0.070	5	Yes	Yes	H II region
N33	24.215	−0.044	5	Yes	Yes	H II region
N34[1]	24.295	−0.170	10	Yes	Yes	H II region, two sources?
N35[1]	24.513	+0.241	15	Yes	Yes	H II region
N36[1]	24.837	+0.090	10	Yes	Yes (saturated)	H II region, open bubble
N37[1]	25.292	+0.293	10	Yes	Yes	H II region, open bubble
N39[1]	25.364	−0.160	10	Yes	Yes (saturated)	bipolar H II region
N40[1,6]	25.369	−0.365	10	Yes	Yes	H II region, two sources?
N41	26.266	+0.282	5	Yes	Yes	H II region
N42	26.329	−0.071	5	Yes	Yes	H II region
N43	26.597	+0.098	5	Yes	Yes	H II region
N44[1]	26.821	+0.382	10	Yes (faint)	Yes	H II region
N45[1]	26.991	−0.053	10	Yes	Yes	H II region
N46[1]	27.310	−0.110	10	Yes	Yes	H II region, open bubble
N47[1]	28.025	−0.031	20	Yes	Yes	H II region
N48	28.332	+0.154	10	?	Yes	?
N49[1]	28.827	−0.229	10	Yes	Yes	H II region
N50[1]	29.001	+0.097	10	Yes	Yes	H II region, open bubble
N51[1]	29.158	−0.262	10	No	Yes	?
G30.250	30.250	+0.240	5	Yes	Yes	H II region
N52[1,7]	30.749	−0.019	20	Yes	Yes (saturated)	H II region
N53[1]	31.157	−0.145	5	Yes	Yes	H II region
G31.16	31.165	−0.127	15	Yes	Yes	H II region
N54[1]	31.164	+0.292	10	Yes	Yes	H II region
N55	32.098	+0.091	5	Yes	Yes	H II region

Table A.1. continued.

Name	*l* (°)	*b* (°)	Size (′)	Radio emission	24 μm emission	Nature
N56[1]	32.583	+0.002	10	Yes	Yes	H II region
N57	32.763	−0.150	5	Yes	Yes	H II region
N58	32.990	+0.040	5	Yes	Yes	H II region
N59	33.071	−0.075	20	Yes	Yes	H II region
N60	33.814	−0.150	5	Yes	Yes	H II region
N61[1]	34.157	+0.140	20	Yes	Yes	H II region
N62[1]	34.334	+0.216	10	Yes	Yes	H II region
N64	34.760	−0.669	20	Yes	Yes	H II region
N64bis	34.695	−0.653	idem	?	Yes	?
N65[1]	35.000	+0.332	15	Yes	Yes	H II region
N65bis	35.062	+0.336	idem	Yes	Yes	H II region
N66	35.259	+0.119	5	Yes	Yes	H II region
N67	35.543	+0.011	10	Yes	Yes	H II region
N67bis	35.573	+0.068	idem	Yes	Yes	H II region
N68	35.654	−0.062	15	Yes	Yes	H II region
N69	36.187	+0.648	30	Yes	Yes	H II region, open bubble
N70	37.751	−0.112	5	Yes	Yes	H II region
N71	38.290	+0.007	20	?	Yes (faint)	?
N72	38.352	−0.133	5	Yes	Yes	H II region
N73	38.739	−0.137	10	Yes	Yes	H II region
N74[1]	38.909	−0.437	20	Yes	Yes	H II region
N75	38.928	−0.387		Yes	Yes	H II region
N76	38.955	−0.731	20	Yes	Yes	H II region
N77[1]	40.421	−0.056	10	Yes	Yes	H II region
N78	41.229	+0.170	5	Yes	Yes	H II region
N79[1]	41.514	+0.030	10	Yes	Yes	H II region
N80[1]	41.930	+0.031	10	Yes	Yes	H II region
N81	42.003	−0.512	25	Yes	Yes (faint)	H II region
N82[1]	42.102	−0.623	idem	Yes	Yes	H II region
N83	42.113	−0.442	idem	Yes	Yes	H II region
N84[1]	42.831	−0.161	10	?	Yes	?
N85	43.074	−0.017	10	?	Yes	?
N86	43.097	−0.040	idem	Yes	Yes	H II region
N87	43.218	+0.107	5	?	Yes	?
N89	43.739	+0.114	25	Yes	Yes	H II region
N90[1]	43.774	+0.059	idem	Yes	Yes	H II region
N91	44.211	+0.050	20	Yes	Yes	H II region, open bubble
N92[1]	44.333	−0.839	10	Yes	Yes	H II region, open bubble
N93	44.777	−0.550	10	Yes	Yes	H II region
N94[1]	44.818	−0.500	15	Yes	Yes	H II region, open bubble
N95	45.393	−0.717	10	Yes	Yes	H II region
N96	46.947	+0.368	5	Yes	Yes	H II region
N97	46.951	+0.312	20	Yes	Yes	H II region, open bubble
N98	47.027	+0.219	10	Yes	Yes	H II region

Notes. (1) The CO environment of these bubbles was studied by Beaumont & Williams (2010).
(2) N1 belongs to the W31 complex, which contains the nearby bright H II region G10.16−0.35.
(3) N6 possibly consists of two different structures, an open bubble in the north and a filament in the south; the radio emission seems to be associated with the filament.
(4) N21 & N22 belong to a large group of H II regions, among them SH2-53 (Sharpless 1959).
(5) N24 is in the test field of the general paper describing the ATLASGAL survey (Schuller et al. 2009).
(6) N40 probably encloses two distinct H II regions (centered at 25.384−0.328 and 25.377−0.357), as two regions of extended 24 μm emission are observed in its direction.
(7) N52 is part of the W43 complex.

Table A.2. Velocities and distances.

Name	CH06 coordinates	Coordinates (2000)	Refs.[1]	Velocity ($\mathrm{km\,s^{-1}}$)	Distance kpc)	Comments
N1[2]	10.231−0.305	10.232−0.301	A+	11.7	2.0/14.8	H II region
		10.16−0.35	S+	12.5	14.6	nearby H II region
		18:09:20.63–20:15:04.5	WW	12.01		dust condensation
		18:09:24.52–20:15:41.5	WW	11.23		dust condensation
N2	10.737−0.468	10.664−0.467	L89	−2.4		H II region
		18:10:25.71–19:56:04.5	WW	−3.21		dust condensation #1
		18:10:35.00–19:55:51.6	WW	−2.91		dust condensation #1
		18:10:29.24–19:55:41.3	W98	2.2–5.9		methanol maser
		18:10:18.58–19:54:24.6	WW	−4.19		dust condensation #2
		18:10:15.63–19:54:46.7	WW	−4.62		dust condensation #2
		18:10:17.99–19:54:04.2	W98	−6.2, −8.0		methanol maser
		18:10:29.80–19:49:03.6	WW	−1.49		dust condensation #3
		18:10:18.60–19:50:16.1	WW	−1.53		dust shell
		18:10:36.53–19:57:05.9	WW	−1.60		dust shell
		18:10:55.17–19:58:35.1	WW	−2.89		dust shell
		18:10:56.40–19:59:19.3	WW	−2.82		dust shell
		18:10:58.19–19:58:58.3	WW	−3.76		dust shell
N4[3]	11.892 +0.748	11.898 +0.747	L89	25.1	3.15/13.48	H II region
		18:08:55.05–18:14:32.6	WW	24.84		dust condensation
N6	12.512−0.609	12.446−0.619	L89	40.0	4.12/12.49	H II region
		18:14:24.04–18:24:43.9	WW	45.99		dust condensation
N8	12.805−0.312	18:14:40.10–17:59:17.7	WW	13.81		dust condensation
N10	13.188+0.039	13.186+0.045	L89	54.1		H II region
		18:14:00.92–17:28:41.3	WW	49.16		dust condensation #1
			P08+	48–49	4.6	methanol maser
		18:14:00.8–17:28:05	SZY00	48.5		methanol maser
		18:14:10.16–17:27:20.6	WW	51.84		dust condensation #2
N11	13.218+0.082	13.231+0.082	A+	54.0	4.7/11.8	H II region
N12	13.727−0.015	18:15:30.2–17:03:58	SZY00	51.9	4.4/11.9	methanol maser
		18:15:37.63–17:04:24.7	WW	47.13		dust condensation
N13	13.900−0.014	13.886−0.017	L89	32.6	3.43/13.07	H II region
N14[4]	14.002−0.135	13.998−0.128	L89	36.0	3.65/12.85	H II region
		18:16:22.91–16:51:56.4	WW	39.97		dust condensation
		18:16:24.23–16:49:49.1	WW	41.06		dust condensation
		18:16:32.89–16:51:22.1	WW	41.32		dust concensation
N16	15.017+0.056	15.00+0.05	A&B	26.5	13.7	H II region
		18:17:50.52–15:53:33.0	WW	24.58		dust condensation
G15.68	15.680−0.28	15.64−0.24	A&B	61.8	11.5	H II region
N18[5]	16.679−0.366	16.61−0.32	A&B	44.9	12.4	H II region
N20	17.917−0.687	17.928−0.677	A+	39.1	12.8	H II region
N21	18.190−0.396	18.19−0.40	A&B	43.2	3.6	H II region
		18:25:19.37–13:12:46.9	WW	49.1		dust condensation
		18:25:21.56–13:13:39.6	WW	46.95		dust condensation
N22	18.254−0.305	18.26−0.30	A&B	50.9	4.0	H II region
		18:25:01.48–13:09:06.4	WW	66.7		dust condensation
		18:25:05.54–13:08:19.8	WW	68.31		dust condensation
		18:25:06.45–13:08:51.3	WW	67.75		dust condensation
		18:25:11.25–13:08:04.4	WW	68.55		dust condensation
		18:25:13.3–13:09:16	SZY00	75.2		methanol maser
Sh2-53		18.143−0.289	K	53.9	4.3	H II region near N21, N22
N23	18.679−0.237	18.677−0.236	A+	42.6, 61.9		H II region
N24[6]	19.000−0.326	19.044−0.431	L89	65.8		large H II region
		19.12−0.34	S+	63.5	4.6	large H II region
		18:26:15.14–12:41:36.4	WW	65.49		dust condensation
		18:26:23.47–12:39:42.2	WW	63.45		dust condensations
N24bis1	19.070−0.279	19.07−0.27	A&B	64.2	4.6	UC H II region
		19.07−0.28	S+	64.2	4.7	UC H II region
		18:26:46.31–12:26:27.3	WW	66.0		dust condensation
N24bis2	19.070−0.279	18.881−0.493	L89	65.5		compact H II region
		18:26:58.87–12:44:49.3	WW	63.27		dust condensation
		18:27:02.74–12:45:12.2	WW	65.2		dust condensation
		18:27:05.69–12:43:10.8	WW	65.43		dust condensation
		18:27:07.49–12:41:41.7	WW	66.08		dust condensation
		18:27:07.83–12:41:35.9	CY	56.46		methanol maser
		18:27:09.27–12:42:36.6	WW	65.5		dust condensation
		18:27:14.60–12:43:10.8	WW	66.21		dust condensation
N25	19.507−0.191	19.504−0.193	A+	37.8	12.8	H II region

Table A.2. continued.

Name	CH06 coordinates	Coordinates (2000)	Refs.[1]	Velocity (km s^{-1})	Distance (kpc)	Comments
G19.82	19.821−0.322	18:28:23.79–11:47:36.1	WW	44.75		dust condensation
N27	19.814+0.017	19.813 +0.010	A+	60.4, 118.0		H II region
N29	23.055+0.559	23.12 +0.56	A&B	29.5	2.2	H II region
N31	23.843+0.097	23.836 +0.104	A+	41.9, 114.3		H II region
N32	23.905+0.070	23.91 +0.07	A&B	32.8	13.1	H II region
		23.91 +0.07	A&B	103.4	9.4	H II region
		18:34:36.18–08:01:02.4	WW	41.03		dust condensation
		18:34:37.06–08:00:21.4	WW	39.25		dust condensation
		18:34:38.2–07:59:35	X+	35.7		methanol maser
N33	24.215−0.044	24.22−0.05	A&B	82.0	10.4	H II region
N34	24.295−0.170	24.30−0.15	A&B	55.5	11.7	H II region
		18:36:07.97–07:45:01.6	WW	53.64		dust condensation
N35	24.513+0.241	24.48+0.21	A&B	115.7	8.6	H II region
		18:35:11.28–07:26:41.1	WW	119.08		dust condensation
		18:34:53.0–07:19:11	SZY02	106.2		methanol maser
N36	24.837+0.090	24.81+0.10	A&B	108.6	6.4	H II region
		24.78 +0.08	P08+	106–115	6.1	methanol maser
		18:36:12.57–07:12:11.5	W98	106.7–114.6		methanol maser
N37	25.292+0.293	25.29+0.31	A&B	39.6	12.6	H II region
N39[7]	25.364−0.160	25.38−0.18	A&B	57.1	3.8	large H II region
		25.30−0.14	A&B	98.4	5.9	compact H II region
		18:38:14.3–06:47:47	X+	58.2		methanol maser
N40	25.369−0.365	25.39−0.35	A&B	62.1	11.3	H II region
N41	26.266+0.282	26.261+0.280	A+	88.6, 117.0		H II region
N42	26.329−0.071	26.330−0.071	A+	100.9	5.9/9.3	H II region
N43	26.597+0.098	26.60+0.09	A&B	102.5	9.0	H II region
N44	26.821+0.382	26.824+0.380	A+	82.0	5.0/10.1	H II region
N45	26.991−0.053	26.98−0.07	A&B	79.9	10.2	H II region
		18:40:46.55–05:21:05.4	WW	81.85		dust condensation
N46	27.310−0.110	27.31−0.14	A&B	92.3	5.6	H II region
		18:41:51.15–05:01:42.5	WW	91.21		dust condensation
N47	28.025−0.031	28.00−0.03	A&B	99.9	8.9	H II region
N49	28.827−0.229	28.82−0.23	A&B	90.6	5.5	H II region
		18:44:51.0–03:45:53.5	WW	86.71		dust condensation #1
		18:44:51.08–03:45:48.5	CY	83.48		methanol maser
		18:44:51.8–03:45:10	WW	87.99		dust condensation #2
		18:44:46.6–03:44:20	WW	96.34		dust condensation #3
		18:44:47.6–03:44:49	C+	100		methanol maser
		18:44:42.5–03:44:21	WW	85.89		dust condensation #4
N50	29.001+0.097	29.007+0.076	A+	67.7	10.6	H II region
G30.250	30.250+0.240	30.249+0.243	A+	8.9, (90.8)	14.0	H II region
N52 [8]	30.749−0.019	30.78−0.03	A&B	91.6	5.7	large H II region
		18:47:28.42–02:01:00	WW	89.48		dust condensation
		18:47:36.15–02:00:58	WW	91.27		dust condensation
		18:47:38.93–01:58:32	WW	94.53		dust condensation
		18:47:39.73–01:57:21.9	W98	91.8		methanol maser
		18:47:41.42–02:00:42	WW	93.89		dust condensation
		18:47:36.80–02:00:49.0	W98	88.0		methanol maser
		18:47:46.98–01:54:19.6	W98	101.2		metanol maser
		30.82−0.05	P08+	105.7	9.0	methanol maser
		18:47:29.9–01:54:39	X+	95.1		methanol maser
N53 [9]	31.157−0.145	31.157−0.148	A+	43.6, (101.6)	11.6	H II region
G31.16	31.165−0.127	31.17−0.13	A&B	41.4	11.9	H II region
N54	31.164+0.292	31.13+0.28	A&B	104.7	7.3	H II region
N55 [10]	32.098+0.091	32.11+0.09	A&B	93.0	8.4	nearby UC H II region
		18:49:36.7–00:41:05	SLY99	93.2		methanol maser
N56	32.583+0.002	32.587+0.006	A+	78.1	9.4	H II region
N57	32.763−0.150	32.761−0.151	A+	30.1	2.1/12.2	H II region
N58	32.990+0.040	32.99+0.04	A&B	89.0	8.6	H II region
		18:51:23 +00:03:46	SZY02	92.0		methanol maser
			P08+	89–93	8.7	methanol maser
N59 [11]	33.071−0.075	33.13−0.09	A&B	87.4	5.6	H II region + UC H II
		33.129−0.094	L89	93.8		H II region + UC H II
		18:52:07.3 +00:08:05	C+	73		methanol maser
			P08+	71–81	8.7	methanol maser
		33.20−0.01	A&B	105.8	7.1	nearby compact H II region
		18:51:58.8 +00:06:31	C+	96		methanol maser

Table A.2. continued.

Name	CH06 coordinates	Coordinates (2000)	Refs.[1]	Velocity (km s^{-1})	Distance (kpc)	Comments
N60	33.814−0.150	33.810−0.154	A+	50.0	10.8	H II region
N61 [12]	34.157+0.140	34.26+0.15	A&B	54.0	3.4	nearby UC H II region
		18:53:19.0 +01:14:52	C+	58		methanol maser
N62 [13]	34.334+0.216	34.325+0.211	A+	62.9	4.1/10.0	H II region
		34.40+0.23	A&B	60.1	10.3	nearby UC H II region
		34.4+0.2	R+		3.7	nearby IRDC
N64	34.760−0.669	34.76−0.68	A&B	52.1	3.2	H II region
N65	35.000+0.332	35.02+0.35	A&B	57.2	3.6	H II region + UC H II
		18:54:00.66 +02:01:19.3	CY	44.36		methanol maser
		18:54:01.3 +02:01:28	P+	44.4		methanol maser
N66	35.259+0.119	35.260+0.122	A+	36.2	11.4	H II region
N67	35.543+0.011	35.541+0.005	A+	57.6	10.1	H II region
N67bis	35.573+0.068	35.57+0.07	A&B	51.8	10.6	H II region
		18:56:04.3 +02:23:28	P+	45.9		methanol maser
N68	35.654−0.062	35.67−0.04	A&B	51.9	10.6	H II region
N69	36.187+0.648	36.29+0.73	A&B	76.5	4.9	H II region
		18:55:15.6 +03:04:42	SZY02	73.0		methanol maser
N70	37.751−0.112	37.75−0.10	A&B	49.7	10.4	H II region
		19:00:38.0 +04:13:18	P+	50.3		methanol maser
N71	38.290+0.007	19:01:20.1 +04:39:37	P+	79.6		methanol maser 1
		19:01:27.2 +04:42:09	P+	15.4		methanol maser 2
N73	38.739−0.137	38.738−0.140	A+	60.9	9.2	H II region
N74	38.909−0.437	19:03:39.7 +05:09:36	P+	31.9		methanol maser
N75	38.928−0.387	38.930−0.386	A+	42.1	2.8/10.4	H II region
N78	41.229+0.170	41.229+0.170	A+	22.9	1.5/11.2	H II region
N79	41.514+0.030	41.52+0.03	A&B	17.7	12.1	H II region
		19:07:09.4 +07:42:19	P+	11.9		methanol maser
N80	41.930+0.031	41.928+0.029	A+	20.7	11.2	H II region
N81 [14]	42.003−0.512				8.1	
N82	42.102−0.623	42.1−-0.62	A&B	66.0	8.1	H II region
N83	42.113−0.442	42.11−0.44	A&B	53.4	9.2	H II region
N90	43.774+0.059	43.770+0.070	A+	70.5	6.1	H II region
N91	44.211+0.050	44.26+0.10	A&B	59.6	8.1	H II region
		19:12:16.4 +10:07:44	P+	55.7		methanol maser
N92	44.333−0.839	44.339−0.827	A+	62.5	6.1	H II region
N94	44.818−0.500	44.79−0.49	A&B	44.8	9.3	H II region
N95	45.393−0.717	45.386−0.726	A+	52.5	8.0	H II region
N96	46.947+0.368	46.948+0.374	A+	−45.2	16.2	H II region
N98	47.027+0.219	47.028+0.232	A+	56.9	5.8	H II region

Notes. (1) References: A&B: Anderson & Bania (2009); C+: Caswell et al. (1995); CY: Cyganowsky et al. (2009); K: Kolpak et al. (2003; A+: Anderson et al. (in preparation); L89: Lockman (1989); P+: Pandian et al. (2007); P08+: Pandian et al. (2008); R+: Rathborne et al. (2005); S+: Sewilo et al. (2004); SLY: Slysh et al. (1999); SZY00: Szymczak et al. (2000); SZY02: Szymczak et al. (2002); WW: Wienen & Wyrowski, in preparation; W98: Walsh et al. (1998); X+: Xu et al. (2008).

(2) N1: the first velocity measurement concerns the nearby H II region G10.16−0.35, and not directly N1. The distance of 3.4 kpc is that of the exciting cluster of G10.16−0.35 (Blum et al. 2001).

(3) N4: we favor the near distance as Hα emission is observed.

(4) N14: we favor the near distance as Hα emission is observed.

(5) N18: the distance is uncertain as the confidence parameters given by A&B are not good.

(6) N24 is a large open bubble. The velocity has been measured in several directions at its border. Two of these are the directions of the UC H II regions (N24bis1 and N24bis2). These UC H II regions are most probably physically associated with N24, as they present very similar velocities.

(7) N39 is a large bipolar nebula, on the border of which lies an UC H II region at 25.397−0.140. This H II region is probably not associated with N39, as it presents a different velocity.

(8) N52: the detailed velocity field of the ionized gas is given by Balser et al. (2001), and the velocity field of the molecular material by Motte et al. (2003).

(9) N53 lies on the border of the large G31.165−0.127 H II region; they are probably linked as they present similar velocities.

(10) N55 lies adjacent to a dense core containing several UC H II regions. The measured velocity is that of one of these UC H II region.

(11) N59 is a large bubble. The second observed direction is that of a compact H II region, on the border of the large bubble. They are possibly associated.

(12) N61 is a large and faint bubble. The measured velocity is that of a nearby UC H II region. They are most probably associated as they lie on each side of an interacting filament.

(13) The distance of N62 is uncertain. Rathborne et al. (2005) assumed that the nearby IRDC, adjacent to N62 and containing the G34.4+0.2 UC H II region, is at the near kinematical distance; A&B put the UC H II region at the far distance, but their confidence parameter is not good.

(14) N81 is a large and faint bubble. N82 and N83 are observed respectively on the border and inside the bubble. N82 is clearly linked to N81, on morphological basis. The association is doubtful for N83. We adopt for N81 the distance of N82.